OXYGEN TRANSFER IN A MODEL HYDROCARBON BIOPROCESS IN A BUBBLE COLUMN REACTOR

by

Jannean Christelle Cloete

Thesis presented in partial fulfillment
of the requirements for the Degree

of

MASTER OF ENGINEERING
(CHEMICAL ENGINEERING)

in the Faculty of Engineering
at Stellenbosch University

Supervisor
Prof K.G. Clarke

March 2015

Declaration

By submitting this thesis electronically, I declare that the entirety of the work contained therein is my own, original work, that I am the sole author thereof (save to the extent explicitly otherwise stated), that reproduction and publication thereof by Stellenbosch University will not infringe any third party rights and that I have not previously in its entirety or in part submitted it for obtaining any qualification.

Date: 20 February 2015

Abstract

The expansion of the global fuels industry has caused an increase in the quantity of hydrocarbons produced as a by-product of refinery gas-to-liquid processes. Conversion of hydrocarbons to higher value products is possible using bioprocesses, which are sustainable and environmentally benign. Due to the deficiency of oxygen in the alkane molecule, the supply of sufficient oxygen through aeration is a major obstacle for the optimization of hydrocarbon bioprocesses. While the oxygen solubility is increased in the presence of hydrocarbons, under certain process conditions, the enhanced solubility is outweighed by an increase in viscosity, causing a depression in overall volumetric oxygen transfer coefficient (K_La).

The rate at which oxygen is transferred is defined in terms of a concentration driving force (oxygen solubility) and the overall volumetric oxygen transfer coefficient (K_La). The K_La term comprises an oxygen transfer coefficient (K_L) and the gas-liquid interfacial area (a), which are dependent on the fluid properties and system hydrodynamics. This behaviour is not well understood for hydrocarbon bioprocesses and in a bubble column reactor (BCR). To provide an understanding of oxygen transfer behaviour, a model hydrocarbon bioprocess was developed using a BCR with a porous sparger.

To evaluate the interfacial area, the Sauter mean bubble diameter (D_{32}) was measured using an image analysis algorithm and gas holdup (ϵ_G) was measured by the change in liquid height in the column. Together the D_{32} and ϵ_G were used in the calculation of interfacial area in the column.

The K_La was evaluated with incorporation of the probe response lag, allowing more accurate representation of the K_La behaviour. The probe response lag was measured at all experimental conditions to ensure accuracy and reliability of data.

The model hydrocarbon bioprocess employed C_{14-20} alkane-aqueous dispersions (2.5 - 20 vol% hydrocarbon) with suspended solids (0.5 - 6 g/l) at discrete superficial gas velocity (u_G) (1 - 3 cm/s). For systems with inert solids (corn flour, $d_p = 13.36\ \mu m$), the interfacial area and K_La were measured and the behaviour of K_La was described by separation of the influences of interfacial area and oxygen transfer coefficient (K_L). To further the understanding of oxygen transfer behaviour, non-viable yeast cells ($d_p = 5.059\ \mu$m) were used as the dispersed solid phase and interfacial area behaviour was determined. This interfacial area behaviour was compared with the behaviour of systems with inert solids to understand the differences with change in solids type.

In systems using inert solids, a linear relationship was found between ϵ_G and u_G. An empirical correlation fo rthe prediction of this behaviour showed an accuracy of 83.34% across the experimental range. The interfacial area showed a similar

relationship with u_G and the empirical correlation provided an accuracy of 78.8% for prediction across the experimental range.

In inert solids dispersions, the K_La increased with u_G as the result of an increase in interfacial area as well as increases in K_L. An increase in solids loading indicated an initial increase in K_La, due to the influence of liquid-film penetration on K_L, followed by a decrease in K_L at solids loading greater than 2.5 g/l, due to diffusion blocking effects.

In systems with yeast dispersions, the presence of surfactant molecules in the media inhibited coalescence up to a yeast loading of about 3.5 g/l, and resulted in a decrease in D_{32}. Above this yeast loading, the fine yeast particles increased the apparent viscosity of the dispersion sufficiently to overcome the influence of surfactant and increase the D_{32}.

The behaviour of ϵ_G in yeast dispersions was similar to that found with inert solids and demonstrated a linear increase with u_G. However, in yeast dispersions, the interaction between alkane concentration and yeast loading caused a slight increase in dispersion viscosity and therefore ϵ_G. An empirical correlation to predict ϵ_G behaviour with increased u_G was developed with an accuracy of 72.55% for the experimental range considered. Comparison of yeast and inert solids dispersions indicated a 37.5% lower ϵ_G in yeast dispersions compared to inert solids as a result of the apparent viscosity introduced by finer solid particles. This ϵ_G and D_{32} data resulted in a linear increase in interfacial area with u_G with no significant influence of alkane concentration and yeast loading. This interfacial area was on average 6.7% lower than interfacial area found in inert solid dispersions as a likely consequence of the apparent viscosity with finer particles.

This study provides a fundamental understanding of the parameters which underpin oxygen transfer in a model hydrocarbon bioprocess BCR under discrete hydrodynamic conditions. This fundamental understanding provides a basis for further investigation of hydrocarbon bioprocesses and the prediction of K_La behaviour in these systems.

Opsomming

Die uitbreiding van die internasionale brandstofbedryf het 'n toename veroorsaak in die hoeveelheid koolwaterstowwe geproduseer as 'n deur-produk van raffinadery gas-tot-vloeistof prosesse. Omskakeling van koolwaterstowwe na hoër waarde produkte is moontlik met behulp van bioprosesse, wat volhoubaar en omgewingsvriendelik is. As gevolg van die tekort aan suurstof in die alkaan molekule, is die verskaffing van voldoende suurstof deur deurlugting 'n groot uitdaging vir die optimalisering van koolwaterstof bioprosesse. Terwyl die suurstof oplosbaarheid verhoog in die teenwoordigheid van koolwaterstowwe, onder sekere proses voorwaardes is die verhoogde oplosbaarheid oortref deur 'n toename in viskositeit, wat 'n depressive veroorsaak in die algehele volumetriese suurstofoordragkoëffisiënt (K_La).

Die suurstof oordrag tempo word gedefinieer in terme van 'n konsentrasie dryfkrag (suurstof oplosbaarheid) en K_La. Die K_La term behels 'n suurstofoordragkoëffisiënt (K_L) en die gas-vloeistof oppervlakarea (a), wat afhanklik is van die vloeistof eienskappe en stelsel hidrodinamika. Hierdie gedrag is nie goed verstaan vir koolwaterstof bioprosesse nie, asook in kolom reaktors (BCR). Om 'n begrip van suurstof oordrag gedrag te voorsien, is 'n model koolwaterstof bioproses ontwikkel met 'n BCR met 'n poreuse besproeier.

Om die oppervlakarea te evalueer, is die gemiddelde Sauter deursnit (D_{32}) gemeet deur 'n foto-analise algoritme en gas vasvanging (ϵ_G) is gemeet deur die verandering in vloeibare hoogte in die kolom. Saam is die D_{32} en ϵ_G gebruik in die berekening van die oppervlakarea in die kolom.

Die K_La is geëvalueer met insluiting van die meter se reaksie sloering, om n meer akkurate voorstelling van die K_La gedrag te bereken. Die meter reaksie sloering was gemeet op alle eksperimentele toestande om die akkuraatheid en betroubaarheid van data te verseker.

Die model koolwaterstof bioproses gebruik n-C_{14-20} alkaan-water dispersies (2.5 - 20 vol% koolwaterstof) solide partikels (0.5 - 6 g/l) op diskrete oppervlakkige gas snelhede (1 - 3 cm/s). Vir stelsels met inerte solides (koring meel, $d_p = 13.36\mu m$), is die oppervlakarea en K_La gemeet en die gedrag van K_La beskryf deur skeiding van die invloede van oppervlakarea en K_L. Om die begrip van suurstof oordrag se gedrag te bevorder, is nie-lewensvatbare gisselle ($d_p = 5.059\mu m$) gebruik as die verspreide solide fase en oppervlakarea is bepaal. Hierdie oppervlakarea gedrag is vergelyk met die van stelsels met inerte solides om die verskille met verandering in solide tipes te verstaan.

In stelsels met inerte solides, is 'n lineêre verwantskap gevind tussen ϵ_G en u_G. 'n Empiriese korrelasie vir die voorspelling van hierdie gedrag is opgestel met 'n akkuraatheid van 83.34% in die eksperimentele reeks. Die oppervlakarea het

'n soortgelyke verhouding met u_G en die empiriese korrelasie verskaf 'n akkuraatheid van 78,8% vir die voorspelling van oppervlakarea oor die eksperimentele reeks.

In inerte solide dispersies, het die K_La toegeneem met u_G as die gevolg van 'n toename in grens oppervlak asook stygings in K_L. 'n Toename in solides belading het n aanvanklike styging in K_La aangedui, as gevolg van die invloed van die vloeistof-film penetrasie op K_L, gevolg deur 'n afname in K_L op vastestowwe ladings groter as 2.5 g/l, te danke aan diffusie blokkeer effekte.

In stelsels met gis dispersies, het die teenwoordigheid van benattings molekules in die media samesmelting geïnhibeer tot 'n gis lading van ongeveer 3.5 g/l, en het gelei tot 'n afname in D_{32}. Bo hierdie gis lading, het die fyn gis partikels die skynbare viskositeit van die verspreiding verhoog genoegsaam om die invloed van benattings molekules te oorkom en die D_{32} te verhoog.

Die gedrag van ϵ_G in gis dispersies was soortgelyk aan die van inerte solides en dui op 'n lineêre toename met u_G. Maar in gis dispersies, het die interaksie tussen alkaan konsentrasie en gis lading 'n effense toename veroorsaak in die verstrooiing viskositeit en dus in ϵ_G. 'n Empiriese korrelasie is ontwikkel om ϵ_G gedrag te voorspel en het 'n akkuraatheid van 72,55% vir die eksperimentele verskeidenheid beskou. Vergelyking van gis en inerte patrikel dispersies wys 'n 37.5% laer ϵ_G in gis dispersies in vergelyking met inerte vaste stowwe as 'n gevolg van die skynbare viskositeit bekendgestel deur fyner vastestowwe partikels. Hierdie ϵ_G en D_{32} data het gelei tot 'n linere toename in grens oppervlak met u_G met geen beduidende invloed van alkaan konsentrasie en gis lading nie. Die oppervlakarea was gemiddeld 6.7% laer as oppervlakarea gevind in inerte partikel dispersies as 'n waarskynlike gevolg van die skynbare viskositeit met fyner partikels.

Hierdie studie bied 'n fundamentele begrip van die veranderlikes wat die suurstof oordrag definieer in 'n model koolwaterstof bioproses BCR onder diskrete hidrodinamiese voorwaardes. Hierdie fundamentele begrip bied n basis vir verdere ondersoek van koolwaterstof bioprosesse en en die voorspelling van K_La gedrag in hierdie stelsels.

Acknowledgements

I would not have been able to complete this thesis without the invaluable support and assistance of many people over the past two years:

- Sven Pfützenreuter, for his help and endless support through countless late nights. For being a constant sounding board for my ideas and thoughts.
- My family, Marius, Elize and Francois Cloete, for their love and support throughout
- Peter Hollis, for sharing his valuable experience in the field with me
- My supervisor, Prof K.G. Clarke for guidance and attention to detail throughout the project
- My fellow students, Thapelo Mokomele and Angelo Ridout for making life in the department more enjoyable
- Fenna Bester, for being a good friend through undergrad and long after. Your support and friendship means the world to me
- My close friends, my support structure, I could not have done this without you
- The workshop, Oom Anton and Oom Jos, for their help building the column casing and setting up the lighting
- Mrs H. Botha, for the particle size analysis
- Wilhelm Burger, for the design of the column
- Francis Layman and Juliana Steyl for their assistance with all orders and financial matters
- Lynette Bresler for always being willing to help with any administrative issues no matter how small
- Alvin Petersen, for technical assistance in the department
- DST-NRF Centre of Excellence (c*change) for funding, in the form of a bursary and project funding

Contents

List of Figures

List of Tables

Nomenclature

A single bubble area.

A_p equivalent surface area.

C measured oxygen concentration.

C^* oxygen concentration under saturated conditions.

C_p dissolved oxygen concentration as given by the probe.

D diameter.

D_F Feret diameter.

D_{32} Sauter mean bubble diameter.

H liquid height.

H_0 liquid height before aeration.

K_La overall volumetric oxygen transfer coefficient.

K_L oxygen transfer coefficient.

K_P probe response lag.

L length.

P perimeter.

ϵ_G gas holdup.

τ_P probe response lag time.

a gas-liquid interfacial area.

d_p particle diameter.

t time [s].

u_G superficial gas velocity.

BCR bubble column reactor.

CCD central composite design.

DO dissolved oxygen.

GOP gassing out procedure.

OTR oxygen transfer rate.

PSP pressure step procedure.

STR stirred tank reactor.

Chapter 1

Introduction

The expansion of the global fuels industry has resulted in an increase in the production of hydrocarbon by-products which are sold as fuels. Conversion of these hydrocarbons to higher value products is especially important in South Africa, where the operation of high capacity refineries, such as SASOL, are essential to the functioning of the economy.

The hydrocarbon structure is saturated and can be either linear (n-alkanes), branched (iso-alkanes) or cyclic (cyclo-alkanes). The conversion of hydrocarbons to high value products depends largely on the addition of a functional group to the hydrocarbon molecule, which is met with difficulties due to the inert nature of hydrocarbons. The difficulties associated with the addition of functional groups to the saturated hydrocarbon molecules can be overcome through the use of micro-organisms, which can utilize hydrocarbons as a feedstock to produce several high value products (Wentzel *et al.*, 2007).

The products which can be produced from hydrocarbon molecules include proteins, carbohydrates and organic acids, among others. One of the most promising of these products is citric acid, which can be directly derived from the hydrocarbon molecular structure (Fukui and Tanaka, 1980). Several compounds which can be produced through the oxidation of hydrocarbon molecules are important in the manufacture of detergents, surfactants and lubricants, as well as in the medical, cosmetic and food industries (Fickers *et al.*, 2005; Wentzel *et al.*, 2007).

One of the challenges in these hydrocarbon bioprocesses is that the oxygen demand must be met solely through aeration since the hydrocarbon molecule is deficient of oxygen (Clarke and Correia, 2008). Conventional techniques to enhance oxygen transfer, such as increasing agitation or aeration rates or increasing partial pressure of the sparge gas result in an increase in shear forces, which can rupture sensitive cells (Sánchez Pérez *et al.*, 2006). Chemical methods, such as the addition of hydrogen peroxide, can also be used to increase oxygen supply. However, this method is limited to systems using organisms with high catalase activity which can remove the toxic hydrogen peroxide and is therefore not widely applicable (Jianlong, 2000).

The addition of small concentrations of hydrocarbons to carbohydrate bioprocesses has shown usefulness as an oxygen vector (Quijano *et al.*, 2010a; Jianlong, 2000; Rols *et al.*, 1990). This is as a result of the increased solubility of oxygen in hydrocarbons. The solubility of oxygen in water is only 8 to 10mg/l (at atmospheric pressure between 15 and 30°C (Jianlong, 2000)), whereas the solubility

of oxygen in hydrocarbons is an order of magnitude greater (Clarke and Correia, 2008).

However, at higher alkane concentration, such as in a hydrocarbon bioprocess, the increase in viscosity with addition of alkane causes a resistance to oxygen transfer and depression of the overall volumetric oxygen transfer coefficient (K_La) (Cascaval *et al.*, 2006; Clarke and Correia, 2008). The K_La depression creates difficulty for oxygen transfer in hydrocarbon bioprocesses which must be further investigated.

A change in reactor configuration may also be used to increase the oxygen transfer in hydrocarbon based bioprocesses. Bubble column reactors (BCRs) afford increased oxygen transfer rates without the high shear caused by impellers in stirred tank reactors (STRs). Bouaifi *et al.* (2001) showed that for an aqueous system, the interfacial area in BCRs is approximately 30% higher than in STRs when compared at the same power consumption levels. Bouaifi *et al.* (2001) also found that the K_La values were higher in BCRs than in STRs, due to the higher interfacial area.

K_La is an important, and easily measured, parameter in defining the rate of oxygen transfer. The K_La term comprises the oxygen transfer coefficient (K_L) and the gas-liquid interfacial area (a), which are both dependent on the system hydrodynamics and fluid properties. While K_L is difficult to measure, the interfacial area can be measured as a function of Sauter mean bubble diameter (D_{32}) and gas holdup (ϵ_G).

In a model hydrocarbon bioprocess, the interfacial area was investigated in a system comprising C_{14-20} alkane-aqueous dispersions (2.5 - 20 vol% alkane) with inert solids (0.5 - 6 g/l) in a BCR. The interfacial area results were then used to provide a more comprehensive understanding of the factors underpinning K_La behaviour in the model hydrocarbon bioprocess with inert solids. Following this, the interfacial area behaviour was measured in a system with non-viable yeast, to provide further understanding of the influence of solid properties on interfacial area behaviour.

Chapter 2

Literature Review

2.1 Mechanism of Oxygen Transfer

To properly describe oxygen transfer behaviour, it is important to understand the underlying mechanisms which govern the transfer of oxygen from the bubble to the oxygen reaction site within a cell. To provide insight into these mechanisms, the main pathway for oxygen transfer will be described firstly for an aqueous system, followed by a discussion of the pathways for oxygen transfer in systems containing an immiscible alkane phase.

2.1.1 Pathways for Oxygen Transfer from Bubble to Cell in Aqueous Systems

Doran (1995) describes eight steps which are required to transfer oxygen in aqueous media to the active sites within a cell. These steps are represented below in Figure 2.1.

Each of the eight steps represented in Figure 2.1 are dependent on the properties of the system. In most aqueous systems, comprising sparingly soluble oxygen, the following steps are required and their relative rates can be described to determine the rate of oxygen transfer and, in turn, which transfer step is rate-limiting.

(a) Oxygen transfer from the bubble center to the gas-liquid interface

(b) Transfer across the gas-liquid interface

(c) Diffusion through the stationary liquid film around the gas bubble

(d) Transfer through bulk liquid

(e) Diffusion through stationary film around the cell or cell clump

(f) Transfer through solid-liquid interface of the cell

(g) Diffusion to individual cell in a floc or cell clump

(h) Intracellular transfer across cytoplasm to the active site for oxygen transfer

Many of these transfer steps are fast, but the main oxygen transfer limitation, and therefore the rate-limiting step in aerobic processes, is transfer through the liquid film around the bubbles (Figure 2.1 (c)). Generally, the other steps offer negligible resistance relative to (c), but in viscous media, transfer through the

bulk liquid, Figure 2.1 (d) can contribute significantly to the oxygen transfer rate (OTR) (Doran, 1995).

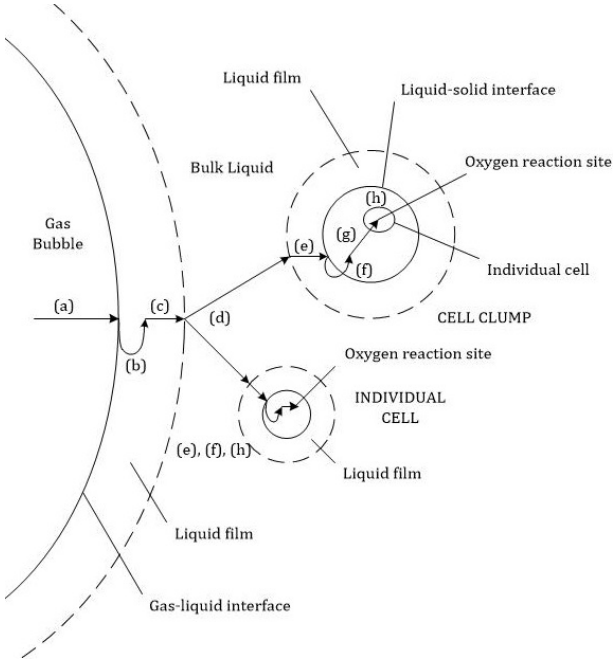

Figure 2.1: Oxygen transfer steps from gas bubble to cell through aqueous media, redrawn from Doran (1995)

2.1.2 Pathways for Oxygen Transfer from Bubble to Cell in Alkane-Aqueous Dispersions

When an immiscible alkane phase is introduced into the system, the behaviour of the alkane phase in the system will determine the pathways for oxygen transfer. In alkane-aqueous dispersions additional diffusion pathways to cells, via the immiscible alkane phase, can occur. These potential pathways are shown in Figure 2.2. This figure illustrates the pathways that oxygen transfer can take in a four-phase system (cells, water, an immiscible liquid (alkane) and air) (Rols and Goma, 1989; Rols *et al.*, 1990).

1. Bubble-water-cell transfer.
   This pathway is common to all aqueous systems, whether or not they contain an alkane phase. For this pathway, the oxygen molecules must first transfer into the bulk liquid before being taken up by the cells and is the mechanism described in Figure 2.1 for carbohydrate bioprocesses.

2. Bubble-cell transfer.
   Cells which adhere to the bubble surface are able to utilize oxygen directly from the bubble. It is common for microbial cells to adhere to the bubble surface due to surface adsorption tendencies (Rols *et al.*, 1990).

3. Bubble-alkane-water-cell transfer.
   In this pathway, the oxygen is dissolved in the alkane phase before diffusion to the bulk liquid takes place and the cells utilize the oxygen from the aqueous phase. For systems where the alkane spreads over the bubble surface, the oxygen transfer is facilitated via this pathway (Rols and Goma, 1989). Although this is also possible where the alkane forms beads around the bubble, it is not probable and generally assumed negligible (Dumont and Delmas, 2003).

4. Bubble-alkane-cell transfer.
   In this mechanism, cells adhere to the alkane droplet, where the alkane is in contact with the bubble surface. The adsorption of the cells onto the alkane would depend strongly on the hydrophobicity of the cells. This is most likely to occur when the alkane spreads over the bubble surface, but can also occur when alkane forms droplets on the bubble surface.

5. Bubble-water-alkane-water-cell transfer.
   In this mechanism, the bubble, alkane and cell are separate from one another and oxygen is transported through the liquid bulk to the alkane, from the alkane to the liquid bulk and then to the cell. This pathway is more probable in systems where the alkane forms droplets in the bulk liquid (Dumont and Delmas, 2003).

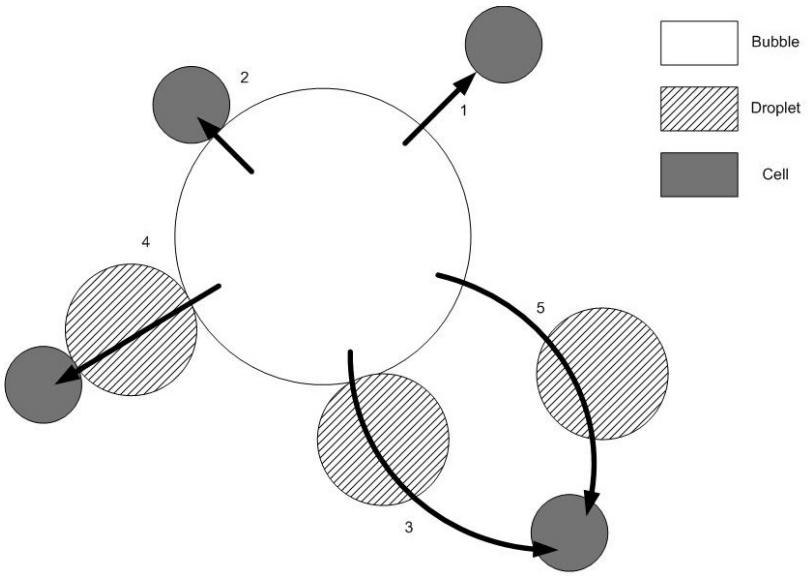

Figure 2.2: Pathways for oxygen transfer in alkane-aqueous dispersions, redrawn from Rols *et al.* (1990)

The existence of a sixth pathway for oxygen transfer, illustrated below in Figure 2.3, where transfer of oxygen is from bubble-water-alkane-cell, has not been discussed in literature. In this mechanism, the cells adhere to an alkane droplet, but the alkane does not adhere to the bubble. This would be more likely in

systems where the alkane forms beads in the bulk liquid. The validation of this pathway could provide additional information regarding mechanisms for oxygen transfer in alkane-aqueous systems, but this is outside the scope of the current project.

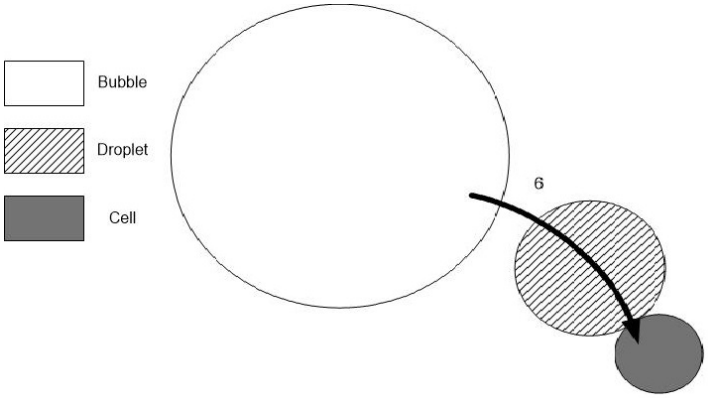

Figure 2.3: Proposed sixth pathway for oxygen transfer to cells in alkane-aqueous systems

2.2 Measurement of K_La

To properly understand the oxygen transfer behaviour, an accurate method must be selected to measure K_La behaviour. Several methods are available for K_La measurement. These include the sulphite oxidation method, the oxygen balance method, gassing out procedure (GOP) and the pressure step procedure (PSP).

The sulphite oxidation method uses the oxidation of sulphite to sulphate to determine the rate of oxygen transfer and gives a direct indication of the oxygen transfer rate (Cooper *et al.*, 1944). However, the use of catalysts in the system may alter the ionic properties and pH of the media, affecting the rate of sulphite oxidation (Linek and Vacek, 1981; Imai *et al.*, 987). The oxygen balance method uses the concentrations of oxygen at all gas streams to establish a mass balance for the determination of dissolved oxygen. The oxygen balance procedure, however, is only applicable to active fermentative systems at steady state and requires gas analyses to determine the oxygen mass balance (Yoshida *et al.*, 1970). The PSP and GOP will be further discussed as well as the GOP method for K_La determination which corrects for the inaccuracies introduced by the probe response lag time (τ_P).

2.2.1 Gassing Out Procedure

The GOP is the most commonly used procedure for the determination of K_La (Doran, 1995). This method involves the measurement of the dissolved oxygen

(DO) response to a step change in the sparge gas composition (Correia and Clarke, 2009) and the subsequent calculation of K_La.

During the GOP, the DO concentration is initially decreased to zero by sparging the reactor with nitrogen. At this point, a step change in the composition of the sparge gas is introduced, by switching between air and nitrogen aeration without interruption of the aeration rate. The rate of the response of DO ($\frac{dC}{dt}$) is measured with an oxygen probe and recorded until oxygen saturation is achieved in the system (Correia and Clarke, 2009; Doran, 1995; Garcia-Ochoa and Gomez, 2009). The K_La can then be solved by linearisation of the first order model given in Equation 2.1, which provides a straight line with gradient equivalent to $-K_La$ (Doran, 1995).

$$\frac{dC}{dt} = K_La(C^* - C) \tag{2.1}$$

Although this method is suitable for many applications and is widely accepted, recent studies have shown significant underestimation of the K_La (up to 49%) in alkane-aqueous dispersions compared to results obtained using PSP (Correia and Clarke, 2009). Clarke and Manyuchi (2012) showed that this inaccuracy arises due to the probe response lag which is not accounted for in the GOP.

2.2.2 Pressure Step Procedure

The PSP was originally developed in aqueous systems (Linek *et al.*, 1989, 1993) and has subsequently shown sufficient accuracy in alkane-aqueous dispersions. This method takes into account the oxygen probe response lag, making it more accurate than GOP, described in Section 2.2.1.

The determination of K_La using PSP involves measurement of the response of DO concentration to a step change in the pressure, rather than the composition, of the sparge gas. Before initiation of PSP, steady state oxygen concentration is obtained in the reactor using low pressure air. Once steady-state has been established, a step change in air pressure is introduced by switching the sparge gas to a higher pressure, to establish a new steady state. A series of dimensionless DO profiles are constructed using theoretical K_La values. The DO profiles are adjusted using a step input response function to incorporate the influence of probe response lag. Thereafter, the transient probe properties are convoluted with the DO profiles for each estimated K_La value to obtain weighted moving averages. Numerical solutions are then applied to solve the equations and compare them to the experimental DO profile. The DO profile which corresponds to the experimental data will yield the actual system K_La.

As is evident from the above procedure, the PSP is both experimentally and mathematically more complex than the GOP. However, the GOP has shown

significant underestimation of the K_La, specifically at high agitation rates (Correia and Clarke, 2009). This error in the determination of K_La, coupled with the complexities associated with the PSP, have prompted the development of a methodology to include the probe response lag in the GOP, further discussed in Section 2.2.3.

2.2.3 Gassing Out Procedure with Probe Response Lag

Benedek and Heideger (1970) and Aiba and Huang (1969) showed that oxygen transfer from the liquid to the DO probe cathode, through the probe membrane, is a oxygen transfer process which results in a τ_P. τ_P is reported to be a function of the membrane type, membrane thickness, membrane age, electrolyte usage, electrochemical half reactions which occur at the anode and cathode, and the properties of the liquid phase (Aiba and Huang, 1969; Benedek and Heideger, 1970; Fuchs *et al.*, 1971). While it is commonly assumed that τ_P is constant at all experimental conditions, the liquid properties will change with system parameters, which will result in a change in the τ_P.

τ_P is measured by transferring the oxygen probe from 0% DO to an oxygen saturated system. This can be accomplished using a sulphide (Na_2SO_3) saturated solution (Benedek and Heideger, 1970; Clarke and Manyuchi, 2012; Nakanoh and Yoshida, 1980) or a nitrogen sparged vessel to achieve a 0% DO environment. The probe response lag (K_P), the inverse of τ_P, is reported to follow a first order response model, given by Equation 2.2.

$$\frac{dC_p}{dt} = K_p(C - C_p) \tag{2.2}$$

where $\frac{dC_p}{dt}$ is the concentration gradient as given by the response; K_p is the probe oxygen transfer coefficient (s^{-1}); C is the DO concentration given by the response ($mol.m^{-3}$) and C_p is the DO concentration due to probe lag time ($mol.m^{-3}$).

τ_P is defined as the time taken for the response to reach 63.2% of the saturation value (Van't Riet, 1979; Merchuk and Gluz, 1999; Tribe *et al.*, 1995). The τ_P, and therefore K_P, can be determined by interpolation between readings to find the time taken to reach 63.2% of the saturation DO.

Combination of the first order model for oxygen transfer (Equation 2.1), where $C = C_P$, with the first order model defining the probe response (Equation 2.2) provides the second order model for the calculation of K_La, given by Equation 2.3. The analytical derivation of this model is provided in Appendix A.1 and is based on the assumption that the membrane is tightly attached to the cathode surface and that the cathode surface is free of contaminants (Aiba and

Huang, 1969). The model can also be derived using Laplacian methodology, but only the analytical method is provided in Appendix A.1.

$$\frac{C_p}{C_p^*} = 1 - \frac{1}{K_p - K_L a}.(K_p e^{-K_L a.t} - K_L a e^{-K_p t}) \tag{2.3}$$

This second order model describes the system response to a step change in aeration with the inclusion of the probe response lag. This methodology can be used to reliably determine the $K_L a$ in alkane-aqueous dispersions without the need for the complex calculations and mathematical modelling of the PSP. The second order model has been shown to yield an accuracy of results which is comparable to those obtained using PSP (Clarke and Manyuchi, 2012).

$K_L a$ can then be calculated by iterative solution of the experimental and calculated $\frac{C_p}{C_p^*}$ data (Clarke and Manyuchi, 2012). The methodology for the measurement of this data is further detailed in Section 3.4.

2.3 Comparison of Reactor Configurations for Oxygen Transfer

Various reactor configurations are available for use in hydrocarbon bioprocesses, including STRs, air-lift columns and BCRs. The following section will discuss these configurations, with a focus on the use of BCRs for hydrocarbon bioprocesses, which will be used in this study.

2.3.1 Stirred Tank Reactors

Typical STRs, used for bioprocesses, consist of a baffled tank, with two identical, six-bladed Rushton turbine impellers for agitation. These reactors commonly make use of ring type spargers, located directly beneath the impeller structure, for aeration.

Many studies, such as those reviewed in Clarke and Correia (2008), have been conducted with a view to enhance the oxygen transfer in hydrocarbon systems. An important finding of these studies is the importance of turbulence on the overall OTR. In STRs, turbulence has a significant influence on bubble coalescence and break up and therefore on the enhancement of interfacial area. Often, this increase in turbulence is introduced through an increase in the agitation speed, thereby increasing the energy input to the system (Clarke and Correia, 2008).

This increase in power supplied to STRs may not be feasible in industrial scale bioreactors. The cost to operate and maintain such a reactor, with a high power

consumption and moving parts, may not be economically viable. A solution to this problem is required, either through the enhancement of the oxygen transfer without an increase in power input, or the optimization of an alternative reactor configuration, which does not require high agitation to achieve sufficient OTR.

2.3.2 Air-lift Column Reactors

Air-lift column reactors offer several advantages for use in bioprocesses. The flow patterns in these reactors are determined by the configuration of the reactor, which consists of two channels in a closed loop, one for the up-flow of the gas-liquid dispersion and the other for liquid down-flow. The reactor channels can be configured in a number of ways, each offering their own advantages for different processes (Merchuk and Gluz, 1999).

The dissipation of energy in air-lift column reactors is more evenly spread throughout the reactor, whereas the energy supplied for the movement of fluids in STRs or BCRs is more localized to the stirrer or sparger regions. One major disadvantage of air-lift columns is the requirement for a specific liquid height in the column, to allow the flow of liquid through both reactor channels. On the contrary, air-lift columns have been demonstrated to show advantages for cell growth operations and they offer high oxygen transfer rates (Merchuk and Gluz, 1999). Since they offer several advantages for bioprocesses, including a higher degree of mixing, without high shear stresses, it may be beneficial to consider air-lift reactors for use in future studies.

2.3.3 Bubble Column Reactors

BCRs have been shown to offer several advantages over conventional STRs. BCRs have simple construction, with only a sparger at their base (Merchuk and Gluz, 1999), and no moving parts, decreasing their maintenance and operating costs (Maceiras *et al.*, 2010; Prakash *et al.*, 2001; Kohler, 1986). This has made BCRs an attractive reactor configuration for bioprocessing operations. In addition, BCRs provide a higher gas dispersion efficiency than STRs (Vlaev and Fialova, 2003) as well as improved reactor performance and capacity (Kohler, 1986). Bouaifi *et al.* (2001) showed improved K_La in BCRs compared to STRs resulting from a greater interfacial area.

Much research has been conducted in BCRs to quantify the oxygen transfer and flow regimes for optimization of BCR systems. The majority of this research has been focused on aqueous systems, with limited research conducted in the presence of alkanes. However, the important properties identified in aqueous systems will most likely also be significant in hydrocarbon processes. The important design parameters for optimization of BCRs are the sparger design, column

geometry and operating conditions, as well as the properties of the gas-liquid dispersion (Maceiras *et al.*, 2010).

The mode of operation of the BCR is also of importance to the design. BCRs can be operated as continuous or batch systems (Pino *et al.* 1992, as reviewed by Kantarci *et al.* 2005). During continuous operation, the air and liquid are fed concurrently at the base of the column. During operation, the superficial gas velocity (u_G) is maintained an order of magnitude greater than the liquid flow rate, to ensure sufficient contact and mixing in the column (Kantarci *et al.*, 2005). During batch operation, the liquid suspension is inoculated at the start of the process and air is bubbled through the reactor as a continuous phase. Since BCRs have no mechanical agitation in the form of impellers, the bubbling of air must provide sufficient mixing and turbulence. The design of the column and operating conditions will be further discussed in Section 2.3.3.1 and 2.3.3.2.

2.3.3.1 Geometry and Sparger Design

The geometry of a BCR is important for optimal oxygen transfer. In this section, the aspect ratio, diameter and sparger design of the column will be discussed, as well as their influence on oxygen transfer.

The aspect ratio, or height to diameter ratio, is an important parameter for the design of BCRs. Industrial-scale BCRs typically operate with an aspect ratio of 5, and columns used for bioprocess applications have aspect ratios varying between 2 and 5. The large diameters of industrial columns are desirable as they offer large gas throughputs and taller columns offer greater contact time for oxygen transfer, allowing for higher conversion of reactants. The disadvantage of large columns are difficulties with ease of operation, such as sterilisation and cleaning. For research purposes, small columns, with diameters less than 15cm, introduce significant wall effects and may cause conditions to differ significantly from those found in large columns (Kantarci *et al.*, 2005). The difference in conditions, caused by wall effects, may be so severe that the results obtained are no longer relevant to actual operations.

The BCR used in this study has a diameter of 15cm and will be operated with a liquid height of 60cm. The operation will therefore be conducted using an aspect ratio of 4, which is in accordance with the typical geometry of BCRs used in bioprocess applications. Furthermore, the diameter of the column is sufficient to eliminate wall effects. Future research may vary the liquid height to investigate the influence of different aspect ratios on oxygen transfer characteristics, however, this study will focus on a single aspect ratio.

The choice of sparger also has a significant influence on the operation of the column. Various sparger types are available to facilitate gas distribution through BCRs. These include perforated plates, membranes and fine porous spargers. To

produce a uniform bubble size distribution across the entire cross section, perforated plate spargers require operation above a certain u_G. Membrane spargers generate a significant pressure drop when compared to other sparger types, but are able to maintain the homogeneous flow regime at greater u_G. Porous spargers offer a larger gas-liquid interfacial area for oxygen transfer, as they can produce a greater number of bubbles with a smaller average bubble size (Mouza *et al.*, 2005). Since the porous sparger is expected to offer improved oxygen transfer and greater interfacial area, due to smaller bubbles, the column used in this study is equipped with a porous sparger for gas distribution.

2.3.3.2 Flow Regimes

The dispersion of air through the BCR is an important parameter and has a significant influence on the behaviour of the bubble bed and consequently on oxygen transfer. There are two main flow regimes encountered in BCRs, namely, the homogeneous flow regime and the heterogeneous flow regime (Camarasa *et al.*, 1999), as well as a third regime, known as the slug-flow regime. These regimes are all depicted in Figure 2.4. While these regimes may be influenced by rheological changes with alkane addition, these were not measured. However, these influences were taken into account in the evaluation of the results.

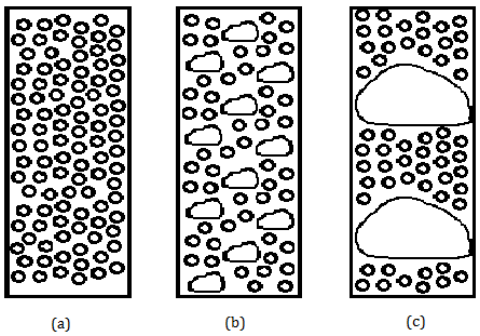

Figure 2.4: Bubble column flow regimes (a) homogeneous (or bubbly flow) regime, (b) heterogeneous (or churn-turbulent) regime and (c) slug-flow regime, redrawn from Camarasa *et al.* (1999); Kantarci *et al.* (2005)

The homogeneous (or bubbly) flow regime, Figure 2.4 (a), is found at low u_G, usually below 5cm/s during batch operation (Kantarci *et al.*, 2005). This regime is characterized by a narrow bubble size distribution with small bubble size and negligible bubble interaction, due to the gentle mixing found at low u_G. In the homogeneous regime, the bubble size formed at the sparger defines the bubble size in the system and these bubbles are evenly distributed across the cross section of the column (Kantarci *et al.*, 2005; Camarasa *et al.*, 1999). Maceiras *et al.* (2010) investigated the influence of height above the sparger in a BCR operating in the homogeneous regime on the bubble size distribution. It was

found that the bubble size distribution varied significantly at the start of the operation, but equilibrium was reached and bubble size no longer varied with height above the sparger. The same bubble behaviour was expected for the current configuration and the height selected for image analysis did not influence the D_{32} results.

As u_G is increased, liquid recirculation patterns are observed. This leads to a change in the turbulence of the system and an increase in bubble interaction, leading to the formation of both large and small bubbles. This change in flow patterns is known as the transition regime and at high u_G shifts operation to the heterogeneous (or churn-turbulent) flow regime (Camarasa *et al.*, 1999).

In the heterogeneous (or churn-turbulent) regime, Figure 2.4 (b), bubble interaction becomes even more prevalent. Bubble collision causes coalescence and the formation of larger bubbles with greater rise velocities are observed. At the same time, the increased turbulence in the system results in a greater tendency for rupture of bubble film and therefore the formation of smaller bubbles through breakup. Because of this complex bubble interaction behaviour, a bimodal bubble size distribution is observed and the bubble size becomes significantly different from that observed near the sparger. The heterogeneous regime also has a noticeable radial gas hold-up profile and the interfacial area must be calculated and modelled using a bimodal bubble size distribution, with separate correlations for large bubbles and small bubbles (Camarasa *et al.*, 1999).

A third flow regime, Figure 2.4 (c), called the slug flow regime, has been encountered in laboratory size BCRs, where wall effects are significant. This flow regime is only reported to occur in small columns, with diameters less than 15cm, and at high u_G. This is an unsteady flow regime, characterized by the formation of bubble slugs, or separated flow, which are caused by the stabilization of large bubbles against the column walls (Hyndman *et al.*, 1997). This regime is not expected to occur in the current study as the column diameter is sufficient to eliminate the influence of wall effects on the bubble flow patterns.

The transition of regimes in aqueous systems have been characterized according to the u_G and column diameter. The regime map, for aqueous systems, has been redrawn in Figure 2.5, to allow for quick reference to predict regime behaviour during operation of the BCR (Deckwer and Louisi, 1980). The red line indicated on this map represents the diameter of the column used in this study and shows that for aqueous systems the column is not expected to operate in the heterogeneous regime. Since BCR flow regime maps have not been characterized for alkane-aqueous dispersions, the intercepts on this curve are not necessarily applicable, and it is important to also consider other methods to determine the operating regime. Despite the data available for aqueous systems, the interpretation of statistical data to evaluate which bubble size distributions are subjective and therefore a more systematic approach should be followed to determine the

regime of operation.

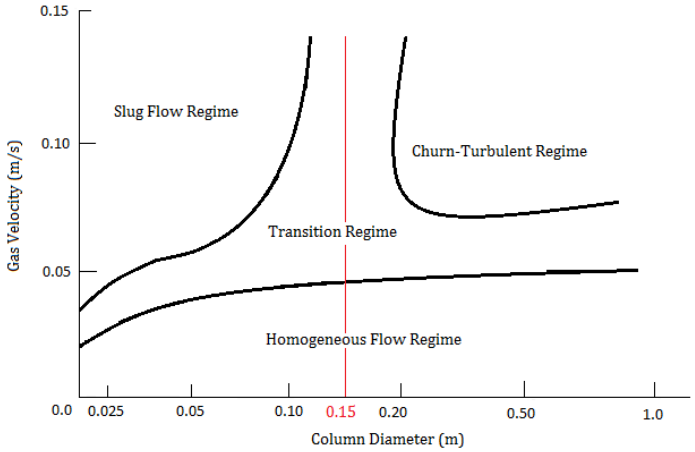

Figure 2.5: Flow regime map for bubble columns using aqueous media, redrawn from Kantarci *et al.* (2005); Deckwer and Louisi (1980)

One such regime classification system is that described by Ruzicka and Zahradnik (2001). This characterization is conducted on the basis of different behaviour of the plot of ϵ_G against u_G in the different operating regimes. The homogeneous regime demonstrates a slightly convex curve, where gas hold up increases progressively with increase in u_G. The heterogeneous regime however, follows a concave trend as u_G increases. These two curves are separated from each other by the transition regime, which shows an inflection at the end of the homogeneous regime, and passes through a local maxima before decreasing back to the beginning of the pure heterogeneous flow regime (Ruzicka and Zahradnik, 2001). This classification of regimes has been supported by Maceiras *et al.* (2010) where sufficient distinction of flow regimes was achieved for diethanolamine (DEA)-aqueous dispersions in a BCR.

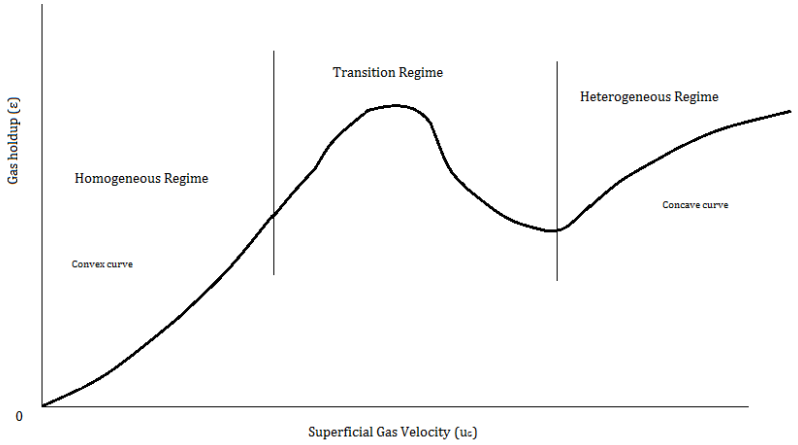

Figure 2.6: Generalised flow regime map, redrawn from Ruzicka and Zahradnik (2001)

2.4 Factors Influencing Oxygen Transfer

An analysis of the literature indicated several important parameters which influence the K_La and the interfacial area. The relevant factors and ranges for evaluation are discussed here with reference to the current study.

2.4.1 Superficial Gas Velocity

The influence of aeration rate on the oxygen transfer in alkane-aqueous dispersions is an important consideration, especially in BCRs. Since BCRs do not make use of mechanical agitation, the aeration rate is the principal factor influencing the mixing in the column.

It is well known that an increase in the aeration rate can be used to increase the turbulence in the system, and therefore the K_La. This trend in K_La has been confirmed by the work of Vandu *et al.* (2004) where it was shown that the K_La in a slurry BCR was enhanced by an increase in aeration rate. In systems containing solid particles, this enhancement has been attributed to an increase in the penetration of the liquid-side diffusion film with increasing u_G (Nguyen-tien *et al.*, 1985), leading to an increase in K_L. Maceiras *et al.* (2010) found an increase in interfacial area as u_G was increased in a BCR with amine. This increase was a result of increasing ϵ_G in the homogeneous flow regime and decreasing bubble size due to increase in bubble breakup behaviour.

The influence of aeration on oxygen transfer in alkane-aqueous dispersions has been well documented for STRs and the trend of this data can be seen in Figure 2.7 (Clarke *et al.*, 2006) at a constant agitation speed of 1000 rpm. From the trend shown in this graph, it is clear that the K_La value increased as the rate of aeration was increased from 0.5 vvm to 1.5 vvm.

It is therefore expected that the K_La in this study will follow a similar trend and with an increase in aeration rate. Since the operation of a BCR does not include mechanical agitation, the low aeration rates used in STRs will not achieve satisfactory mixing in the BCR. Therefore, higher aeration rates, or u_G, are required in the BCR. However, to remain in the homogeneous regime, where bubble distributions are more well defined than in the transition regime, the u_G will be maintained at velocities less than 4 cm/s (The change in regimes can be seen in Figure 2.5, where the red line is indicative of the column used in this study).

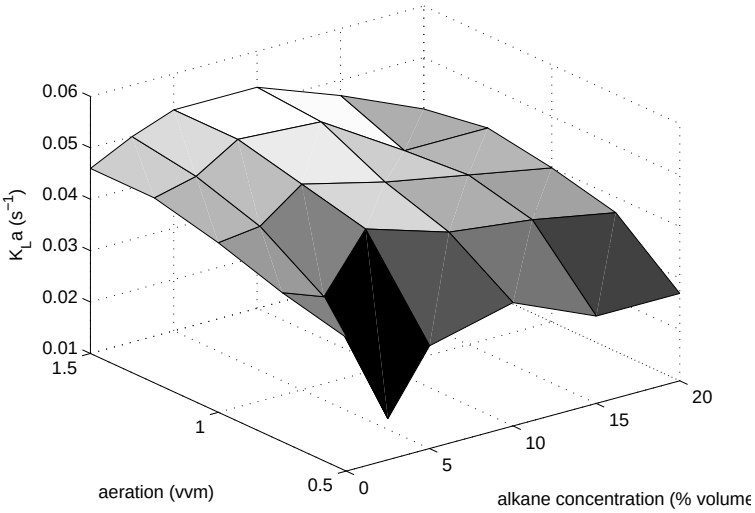

Figure 2.7: Influence of aeration and alkane concentration on K_La in a stirred-tank reactor at agitation of 1000 rpm, data from Clarke *et al.* (2006)

2.4.2 Alkane Concentration

Alkane-aqueous dispersions have been investigated in STR environments with respect to the influence of aeration, alkane concentration and agitation rates on oxygen transfer. Correia *et al.* (2010) showed, using n-C_{10-13} alkane cut in a STR, an initial enhancement of K_La with increasing alkane concentration, followed by a decrease.

The interfacial area available for oxygen transfer is reported to increase with an increase in alkane concentration (Rols *et al.*, 1990). This is suggested to result from the decreased surface tension brought about by the addition of alkanes, which limit the coalescence behaviour in the dispersion (Akita and Yoshida, 1974; Schafer *et al.*, 2002). However, above a certain alkane concentration, the influence of increased viscosity apparently outweighed the positive influence of the reduced surface tension and coalescence became prevalent in the system, resulting in larger bubbles and a decrease in the interfacial area (Schafer *et al.*, 2002; Galindo *et al.*, 2000).

Studies using n-dodecane and n-perflourocarbon as oxygen vectors to increase K_La confirm this enhancement of K_La throughout the range investigated, 0 - 4 vol% (Jia *et al.*, 1997). A similar trend is expected in the BCR, where K_La and interfacial area will experience an initial increase, followed by a decrease when viscosity effects result in the formation of larger bubbles. To confirm this, the alkane range investigated must extend through the supposed maximum point, and will therefore be varied between 2.5 and 20 vol%.

2.4.3 Solids Loading

In a bioprocess, cells are present and behave as solid particles. Therefore, in the characterisation of a model bioprocess, it is important to consider the influence of solids on the oxygen transfer.

To develop a model hydrocarbon bioprocess, a solids loading similar to that found in a hydrocarbon bioprocess must be used. Crolla and Kennedy (2001) investigated a bioprocess with n-paraffin as substrate in a STR and found that the optimal inoculation concentration of yeast was 5 g/l.

An evaluation of literature (Table 2.1) showed that most studies do not use solids loadings representative of a bioprocess. Evaluation of the data in Table 2.1, only Prakash *et al.* (2001) and Oguz *et al.* (1987) used solids loadings in an appropriate range. However, these studies do not contain an immiscible liquid phase and Oguz *et al.* (1987) used metal oxides, which do not provide a representative density for bioprocesses.

Several systems shown in Table 2.1 included an immiscible liquid phase. However, the solids loadings employed in Inga and Morsi (1999); Behkish *et al.* (2002) and Öztürk and Schumpe (1987) are far greater than those found in hydrocarbon bioprocesses and do not provide enough detail at the relevant solids loadings to understand the oxygen transfer behaviour at solids loadings relevant to a hydrocarbon bioprocess.

Table 2.1: Properties of inert solids used in mass transfer studies

Solids Loading (g/l)	**Reactor Type**	**Solids Type**	**Particle Size (μm)**	**Density (kg/m^3)**	**Immiscible Liquid Phase**	**Reference**
0 - 23	Stirred Tank	non-pyrophoric Raney nickel	10 - 15	6500	n/a	Dietrich *et al.* (1992)
0 - 23	Stirred Tank	pyrophoric Raney nickel	10 - 15	6500	n/a	Dietrich *et al.* (1992)
0 - 50	Bubble Column	Nylon	800	1190	n/a	Jamialahmadi and Muller-Steinhagen (1991)
0 - 100	Bubble Column	Styrocel (polystyrene)	1300	1360	n/a	Jamialahmadi and Muller-Steinhagen (1991)
0 - 102	Bubble Column	calcium alginate	1200 - 2100	1023	n/a	Mena (2005)
0 - 134	Airlift Column	biofilm-coated particles	470 - 1950	1319	n/a	Nicolella *et al.* (1998)
0 - 245	Stirred Tank	glassy alumina-silica fly ash (fillite)	30-180	700	n/a	Bartos and Satterfield (1986)
0 - 307	Airlift Column	calcium alginate	2131	1023	n/a	Freitas and Teixeira (2001)
0 - 350	Stirred Tank	polypropylene	30 - 180	1000	n/a	Bartos and Satterfield (1986)

0 - 400	Stirred Tank	polypropylene	53 - 250	not given	n/a	Joosten *et al.* (1977)
0 - 500	Bubble Column	Iron oxides	1,5 - 40	not given	hexane	Inga and Morsi (1999)
0 - 864	Bubble Column	Iron oxides	1,5-40	4000	hexane	Behkish *et al.* (2002)
0 - 900	Bubble Column	Glass beads	11,4	2500	hexane	Behkish *et al.* (2002)
0,5 - 1,2	Stirred Tank	ZnO	1	4720	n/a	Oguz *et al.* (1987)
1 - 1,8	Stirred Tank	TiO2	0,5	3610	n/a	Oguz *et al.* (1987)
1 - 4	Bubble Column	Glass beads	11	not given	n/a	Prakash *et al.* (2001)
1 - 4,5	Stirred Tank	Fe2O3	0,5	4380	n/a	Oguz *et al.* (1987)
1,5 - 33	Stirred Tank	activated carbon	26,96	1640	n-butanol	Ozkan *et al.* (2000)
2 - 50	Bubble Column	Calcium hydroxide	7	not given	n/a	Sada and Kumazawa (1985)
2 - 127	Bubble Column	kieselguhr	6,6	2360	n/a	Schumpe and Deckwer (1987)
3 - 55	Stirred Tank	CaCO3	9,39	2750	n-butanol	Ozkan *et al.* (2000)

3 - 63	Bubble Column	aluminium oxide	8,1	3180	n/a	Schumpe and Deckwer (1987)
4 - 77	Stirred Tank	TiO2	0,54	3830	n-butanol	Ozkan *et al.* (2000)
4 - 84	Stirred Tank	BaSO4	2,47	4220	n-butanol	Ozkan *et al.* (2000)
5 - 104	Stirred Tank	Fe2O3	6,19	5210	n-butanol	Ozkan *et al.* (2000)
5 - 150	Bubble Column	Activated carbon	5,4	1800	n/a	Schumpe and Deckwer (1987)
9 - 184	Bubble Column	activated carbon	4 - 6	1800	n/a	Quicker *et al.* (1984)
10 - 50	Bubble Column	ZnO	2,3	not given	n/a	Zahradnik and Drápal (1992)
10 - 100	Bubble Column	aluminium oxide	6 - 10	3180	n/a	Quicker *et al.* (1984)
10 - 200	Bubble Column	Ca(OH)2	7	240	n/a	Sada *et al.* (1986)
10 - 300	Bubble Column	kieselguhr	4 - 6	2360	n/a	Quicker *et al.* (1984)
48 - 357	Bubble Column	polyethylene	10,5	965	ligoin & tetralin	Öztürk and Schumpe (1987)

49 - 143	Bubble Column	polystyrene	2000	1050	n/a	Tang and Fan (1990)
54 - 156	Bubble Column	nylon	2500	1150	n/a	Tang and Fan (1990)
55 - 160	Bubble Column	acrylic	1500	1180	n/a	Tang and Fan (1990)
61 - 177	Bubble Column	acetate	1000	1300	n/a	Tang and Fan (1990)
167	Stirred Tank	styrene-butadiene copolymer	3570	940	n/a	Littlejohns and Daugulis (2007)
167	Stirred Tank	nylon 6,6	2590	1140	n/a	Littlejohns and Daugulis (2007)
167	Stirred Tank	silicone rubber	2500	1150	n/a	Littlejohns and Daugulis (2007)

Several studies have been conducted to investigate oxygen transfer with non-viable microbial cells, shown in Table 2.2. However, these systems cannot be used to predict oxygen transfer behaviour in hydrocarbon bioprocesses as they do not contain representative hydrocarbon concentrations. In studies where hydrocarbons have been used (Cascaval *et al.*, 2006; Galaction *et al.*, 2005), the hydrocarbon phase was included as an oxygen vector. These concentrations do not offer sufficient information regarding the behaviour of solid particles in systems with similar dispersion properties to those found in hydrocarbon bioprocesses.

Prakash *et al.* (2001) investigated the influence of non-viable yeast cells (0.1 - 0.4 wt%) on ϵ_G in an alkane-aqueous dispersion BCR. However, substantial foaming was observed which may suggest that microbial cells remained active following deactivation. This excessive foaming could however, also be the result of high u_G, causing entrapment of solid particles in the foam layer, rather than in the dispersion. Khare and Joshi (1990) investigated the influence of fine alumina particles on ϵ_G and found an initial increase, followed by a decrease in ϵ_G as solids loading was increased above 0.7 wt%.

Joosten *et al.* (1977) investigated the influence of solids on K_La in a STR and found an initial increase, followed by a sharp decrease with increasing solids loading (polypropylene and glass beads). The decrease in K_La at higher solids loading was attributed to a decrease in the interfacial area, although this was not measured. The behaviour of fine particles in a fluidized bed reactor was investigated by Khare and Joshi (1990) who found that the addition of solids with a smaller d_p resulted in an increase in the ϵ_G. This increase was a likely consequence of the increase in viscosity introduced by the presence of fine solid particles. (0-1 vol%) alumina.

Table 2.2: Oxygen transfer studies using microbial cells

Reference	**Reactor Type**	**Immiscible liquid phase**	**Microorganism**	**Deactivation method**
Amaral *et al.* (2008)	Stirred tank	perfluoro-decalin	*Y. lipolytica*	30% ethanol
Cascaval *et al.* (2006)	Stirred tank	n-dodecane	*P. shermanii*	0.2% pyrogallic acid & 0.4% KOH
Cascaval *et al.* (2006)	Stirred tank	n-dodecane	*S. cerevisiae*	0.2% pyrogallic acid & 0.4% KOH
Galaction *et al.* (2004)	Stirred tank	none	*P. chrysogenum*	0.2% pyrogallic acid & 0.4% KOH
Galaction *et al.* (2004)	Stirred tank	none	*P. shermanii*	0.2% pyrogallic acid & 0.4% KOH
Galaction *et al.* (2004)	Stirred tank	none	*S. cerevisiae*	0.2% pyrogallic acid & 0.4% KOH
Galaction *et al.* (2005)	Stirred tank	n-dodecane	*S. cerevisiae*	0.2% pyrogallic acid & 0.4% KOH
Ju and Sundararajan (1994)	magnetic stirrer	none	*S. cerevisiae*	active, non-respiring cells

2.5 Hypotheses

Since the oxygen transfer behaviour in a model hydrocarbon bioprocess BCR is not well understood, such a system was investigated. The main objective was to determine the influence of u_G, alkane concentration and solids loading on interfacial area and to use this behaviour to understand the K_La. Additionally, the influence of solids type on the interfacial area behaviour was determined to provide a basis for understanding oxygen transfer in a hydrocarbon bioprocesss BCR.

1. **An increase in u_G would cause an increase in interfacial area and an increase in K_La**
   Enhancement of interfacial area was observed with amine-aqueous systems in a BCR due to an increase in ϵ_G in the homogeneous flow regime and decrease in D_{32}.
   An increase in u_G also resulted in an increase in K_La for slurry BCRs from an increase in both interfacial area and K_L behaviour.

2. **An increase in alkane concentration would indicate a maximum value for interfacial area and K_La**
   An initial increase in interfacial area was observed for BCRs with an immiscible liquid phase due to the competing influences of surface tension and viscosity.
   K_La showed similar behaviour in a STR, resulting from the interfacial area behaviour and the influence of fluid properties on K_L.

3. **An increase in solids loading would cause an initial increase in interfacial area and K_La, followed by a decrease**
   At low solids loading, an increase has shown an increase in ϵ_G. Further increase in solids loading has demonstrated a sharp decrease in ϵ_G.
   K_La showed similar behaviour with increased solids loading, where the decrease at higher solids loading was attributed to a possible decrease in the interfacial area.

4. **The interfacial area will be higher for systems with finer particles**
   The use of finer particles in an aqueous dispersion BCR has shown an increase in ϵ_G and therefore interfacial area as a likely result of the increase in dispersion viscosity introduced by fine particles.

Chapter 3

Materials and Methodology

3.1 Materials

The study was conducted in a model hydrocarbon bioprocess. Solid particles were suspended in an alkane-aqueous dispersion in a BCR. The alkane composition is provided in Section 3.1.1. Section 3.1.2 provides information related to the solids, such as the protocol followed for the measurement of particle sizes and the methodology for the preparation of non-viable microbes.

3.1.1 Hydrocarbons

For all experiments a straight chain hydrocarbon cut, n-C_{13-21}, was used. The composition of this hydrocarbon cut was determined using gas chromatographic analysis and the composition is shown below in Table 3.1. The hydrocarbon was composed, per volume, of 0.81% n-C_{13}, 28.06% n-C_{14}, 26.62% n-C_{15}, 22.67% n-C_{16}, 15.51% n-C_{17}, 5.37% n-C_{18}, 0.82% n-C_{19}, 0.10% n-C_{20} and 0.03% n-C_{21}.

Table 3.1: Composition of n-C_{13-21} alkane

Chain length	Composition (vol%)
n-C_{13}	0.81
n-C_{14}	28.06
n-C_{15}	26.62
n-C_{16}	22.67
n-C_{17}	15.51
n-C_{18}	5.37
n-C_{19}	0.82
n-C_{20}	0.10
n-C_{21}	0.03
Impurities	6.00

3.1.2 Solid Particles

The solids used in this study included both an inert solid and a non-viable microbe. The inert solid selected was corn flour ($d_p = 13.36\ \mu m$), and *Saccharomyces cerevisiae* was selected as the non-viable microbe ($d_p = 5.059\ \mu m$). To provide a system which was both representative of a bioprocess, as well as providing information regarding the influence of different solids loadings, a range from 0.5 to 6 g/l was selected, as discussed in Section 2.4.3.

3.1.2.1 Measurement of Particle Size

To facilitate discussion of the influence of particle size on the oxygen transfer in a BCR, the average particle size must be known. The particle size was determined by Static Laser Light Scattering, using a Saturn DigiSizer 5200 (Micromeritics Instrument Corporation).

To measure the particle size, this procedure used a laser and a charge-coupled device containing over one million detector elements. The detectors measured the intensity of light scattered by the particles at different angles. The scattering of this light is dependent on the particle shape, size, refractive index and the wave length of the incident light. Using the Mie theory, the particle size distribution was determined from the angle distribution of the scattered light intensity, as collected by the charge-coupled device detectors. The particle sizes, and standard deviation of measurements, are reported in Table 3.2 (H. Botha, personal communication).

Table 3.2: Properties of inert solids

Inert Solid	Particle Size (μm)		
	Mean	Median	Mode
Corn flour	13.36 ± 0.052	14.04 ± 0.030	15.05 ± 0.00
Non-viable microbes	5.059 ± 0.114	5.087 ± 0.037	5.341 ± 0.00

3.1.2.2 Method for Preparation of Non-viable Microbes

The *S. cerevisiae* cells were deactivated prior to use in the system. The deactivation was carried out according to a procedure developed by P. Hollis (personal communication. 2013), as described below.

Dried yeast pellets were transferred into a centrifuge tube containing 200 ml of physiological saline solution (0.85% NaCl (w/v)). The amount of yeast used was dependent on the required concentration for the experiment (Section 3.5)The

mixture was vortexed to ensure a homogeneous dispersion of cells before placing the dispersion in a water bath at 75°C. After 20 minutes, the yeast suspension was transferred to an ice bath where it was rapidly cooled.

To evaluate the effectiveness of the deactivation technique, both methylene blue staining and streak plate techniques were used. Methylene blue staining has shown consistent results and is effective in cultures of *S. cerevisiae* (Trevors *et al.*, 1983). Since the cell walls of *S. cerevisiae* are negatively charged (Vu *et al.*, 2011), they do not allow the anionic methylene blue solution to penetrate the cell wall. In contrast, the inactive cells do not have a surface charge and these cells are readily dyed by the solution. In this study, methylene blue solution with a concentration of 0.002% (w/v) was found to be sufficient for staining inactive cells.

Following this staining technique, the percentage viability of cells in the culture was determined by a cell count in a Boeco haemocytometer, using a Zeiss Axiostar Plus microscope at 400x magnification. To ensure a sufficient number of cells, counting was conducted in five chambers of the haemocytometer. The percentage viability of cells was determined for five independent samples to confirm the effectiveness of the deactivation technique. The percentage viability of cells was calculated using Equation 3.1. The average viability of cells following deactivation was less than 1%.

$$\%\ viability\ of\ cells = \frac{total\ viable\ cells}{total\ cells} \times 100 \tag{3.1}$$

In addition to the methylene blue staining test, the viability of cells was also shown using streak plate techniques. A sample from the yeast suspension was streaked onto a 39 g/l potato dextrose agar plate, and incubated at 30°C for 72 hours to confirm that no growth occurred in the non-viable yeast sample. An image of the agar plates, showing the sample prior to deactivation on the left and after deactivation on the right, is given below in Figure 3.1.

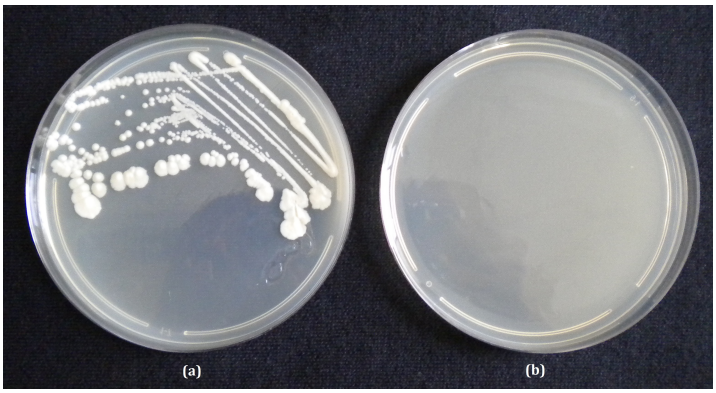

Figure 3.1: Streak plates indicating the growth of *S. cerevisiae* after 72 hours incubation at 30°C (a) before deactivation and (b) after deactivation

3.2 Experimental System

A schematic of the experimental setup is illustrated in Figure 3.2 and a photograph of the BCR is provided in Figure 3.3. The glass BCR (6), as designed by W. Burger (2012), used in this study was cylindrical with an inside diameter of 15 cm. The column was operated at a liquid height of 60 cm, providing an aspect ratio (L/D) of 4. The column was aerated (stream a) through a flat surface porous sparger (7). The column was equipped with an outlet below the sparger for easy drainage of liquid media (stream b).

The assembled column was placed in a rectangular perspex box (4) which acted as a flat plane for image acquisition to remove the optical distortion against the cylindrical surface of the BCR (Camarasa *et al.*, 1999; Wilkinson *et al.*, 1993; Galindo *et al.*, 2005). The perspex box was positioned with close proximity to the column surface. The side panels of the perspex box were constructed of white perspex to provide maximum reflection of light to the column contents. This additional reflection of light and close proximity to the column edge ensured sufficient contrast in the acquired images. In addition, the perspex box was also used to maintain the temperature in the system by acting as a buffer between the column and the surrounding environment.

To prevent the release of alkane to the laboratory environment, and to ensure a constant composition throughout experimentation, a condenser (8) was placed on the off-gas vent. The condenser was operated with a flow of cold water (stream c) to condense residual alkanes in the vapour exiting the column (stream d).

During operation, compressed air feed through the sparger was controlled using a needle valve (stream a). The flow rate of air was maintained constant using a Cole Parmer high flow 150 mm rotameter (3), calibrated as described in Appendix A.2, and the u_G was determined using this calibration curve.

The DO in the system was measured using a Mettler-Toledo InPro 6800 polarographic oxygen sensor (DO probe, inserted through a port in the reactor lid. The DO probe (5) was connected to a Mettler-Toledo M300 analytical transmitter and was used to measure K_La and K_P. Image acquisition was conducted using a high speed camera (Matrix Vision mvBlueFOX 124G) (2) connected to a computer (1) for image storage.

To provide sufficient contrast in the images, a light source is required (Taboada *et al.*, 2003; Mouza *et al.*, 2005). This was achieved using a panel of white LED strip lights (9) mounted on an aluminium sheet. Although previous studies have made use of a light diffuser, it was found experimentally that the presence of solids in the investigated system provided sufficient diffusion of light across the imaging area. The full stepwise experimental procedure can be found in Appendix A.3.

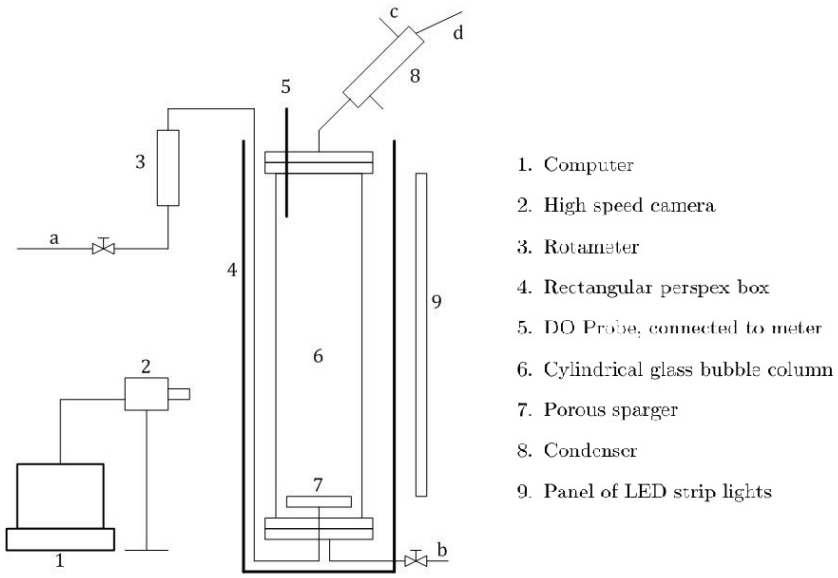

Figure 3.2: Bubble column setup used in experiments

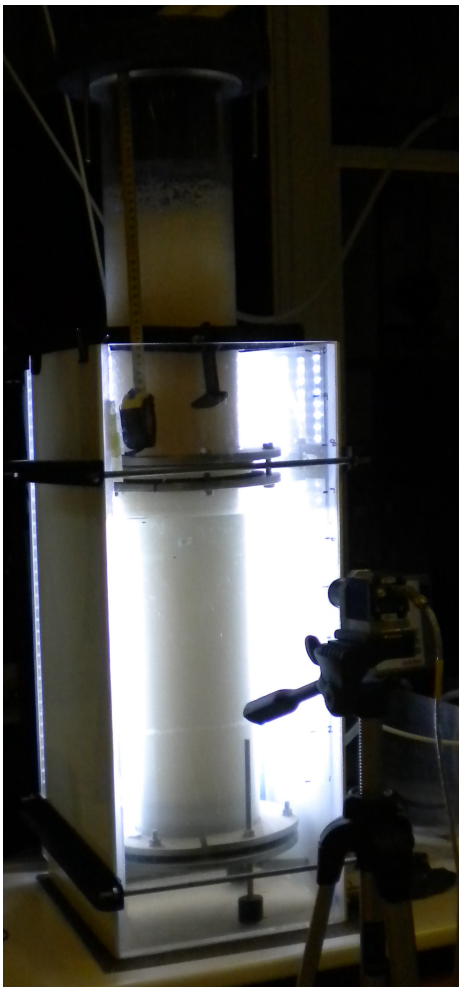

Figure 3.3: Bubble column equipment during operation

3.3 Measurement of Interfacial Area

The interfacial area was measured to provide an understanding of the behaviour underpinning K_La and is a function of D_{32} and ϵ_G. This section provides details pertaining to the image acquisition and processing, as well as the calculation of interfacial area. D_{32} was determined through image analysis techniques and ϵ_G was determined by measuring the liquid height in the BCR. The D_{32} and ϵ_G were then used to calculate the interfacial area in the column.

3.3.1 Image Acquisition

A high speed camera (Matrix Vision mvBlueFOX 124G) was used to acquire images for analysis of bubble size. The large resolution of the sensor, relative to others in the range, on this compact industrial camera is 1.9 million pixels (or 1.9 mega pixels), and allowed the acquisition of detailed images. These images were directly stored on a computer with resolution of 1600 x 1200.

To obtain consistent images, the camera was positioned on a stable tripod 20cm from the column at a constant height of 30cm above the sparger. Images were captured through a window to ensure that each experiment was focused on the same section of the column. The ASTM E1951 standard ruler method (ASTM International, 2007) was used to calibrate the image sizes to obtain a conversion between pixels and metric length. This was done using a line of 10mm length, included in each captured image.

A representative sample was ensured in all experiments. Evaluation of literature showed a wide range in the number of bubbles used for image analysis data, with sample size ranging from 30 to 10 000 bubbles (Table 3.3). Although Colella *et al.* (1999) used a sample size of 500 bubbles (Table 3.3), it was shown that a sample of 100 - 200 bubbles provided sufficient information to draw statistically significant conclusions, while 500 bubbles offered enough information for the study of coalescence and bubble breakup. In the data shown in Table 3.3, only Taboada *et al.* (2006) made use of a solid phase (fungal culture) and found that a sample size of 300 bubbles provided sufficient reproducibility. Junker (2006) reviewed image analysis procedures and found that for BCR studies a sample size between 300 and 1000 bubbles offered reproducible data. Based on this evaluation, a sample size of at least 300 bubbles was used to offer a representative sample with sufficient repeatability in the model hydrocarbon bioprocess BCR.

Table 3.3: Number of bubbles required to obtain a representative sample for bubble size studies

Number of bubbles	**Reactor type**	**Liquid media**	**Immiscible phase**	**Solid phase**	**Reference**
30	Bubble Column	DEA solutions	none	none	Maceiras *et al.* (2010)
150 - 200	Stirred Tank	Water	none	none	Bouaifi *et al.* (2001)
150 - 200	Bubble Column	Water	none	none	Bouaifi *et al.* (2001)
300	Stirred Tank	Fermentation Broth	castor oil	fungal culture	Taboada *et al.* (2006)
300	Stirred Tank	Water	none	none	Vega-Alvarado and Cordova (2004)
300 - 3000	Airlift Column	Water	none	none	Kiambi and Duquenne (2001)
400	Stirred Tank	Mineral salt media	silicone oil	none	Quijano *et al.* (2010b)
500	Stirred Tank	Water	castor oil	none	Galindo *et al.* (2000)
500	Bubble Column	Water	none	none	Colella *et al.* (1999)
500	Stirred Tank	Water	none	none	Barigou and Greaves (1992)
600	Stirred Tank	Water	alkane	none	Correia *et al.* (2010)
4000 - 70 000	Stirred Tank	Water & n-butanol	none	none	Laakkonen *et al.* (2005)
10000	Bubble Column	Water	none	none	Bailey *et al.* (2005)

3.3.2 Image Processing

Processing of the images acquired as described in Section 3.3.1 was conducted using software developed in MATLAB® by Correia (2007) and later modified by Hollis (2013), Burger (2012) and Yzelle (2012), and made use of the functions available in the Image Analysis Toolpack provided with MATLAB® software.The source code for this software is given in Appendix A.5. The software makes use of image segmentation to detect an object. Image morphology and edge detection principles were used to detect bubbles in the dispersion. The image processing steps are described in this section.

3.3.2.1 Image Pre-Processing and Contrast Enhancement

Prior to image processing, the acquired bitmap image was read into the program as an input using the '`imread`' function. If required, the '`imcrop`' function can be enabled to crop the image and retain only the area with bubbles for analysis, but this was not used in the current algorithm. Figure 3.4 shows an acquired image, prior to contrast enhancement and analysis.

Figure 3.4: Image prior to contrast enhancement and median filtering. Image at 7.88 vol% alkane, 5 g/l corn flour and 2 cm/s superficial gas velocity

Several methods exist for the enhancement of images for edge detection. The methods employed in this software were sharpening, median filtering and contrast adjustment. Image sharpening resulted in more defined, crisp edges by increasing the brightness of bright pixels and the darkness of the darker pixels. To sharpen the image, the '`imfilter`' function was applied. This function was used to filter multidimensional images, by computation of an output array using

a double-precision floating point (Correia, 2007). The value for image sharpening was adjusted between 0 and 1, with a default value of 0.5.

Median filtering was applied using the 'medfilt2' function, which performed two-dimensional median filtering, using the nearest neighbours to adjust each pixel, based on their median value. The use of a median value, rather than a mean, to determine the pixel value in the new image allowed for the removal of outlier pixels, without reducing the sharpness of the image (Correia, 2007).

The contrast of the image was enhanced using the 'imadjust' function. This function mapped the values in the original image to new values according to the user defined low and high limits. These high and low values were adjusted for each experimental set between 0 and 255. Figure 3.5 shows the result of Figure 3.4 after pre-processing and contrast enhancement operations were applied.

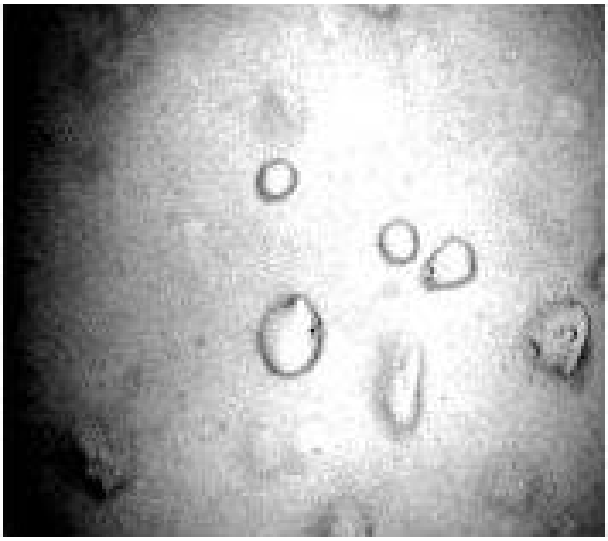

Figure 3.5: Image after contrast enhancement and median filtering. Image at 7.88 vol% alkane, 5 g/l corn flour and 2 cm/s superficial gas velocity

3.3.2.2 Edge Detection and Image Analysis

Following the enhancement of the images, the image segmentation was initiated. For image segmentation, the following steps were required before D_{32} data were extracted.

Edge detection was conducted using the 'edge' function. This function used the Sobel method for edge detection. This algorithm calculated the derivative of the intensity in the image and defined the object edges as the point at which a maximum gradient of the intensity was found (The Mathworks Inc, 2014a)

To obtain an effective delineation of the bubble edges, Correia (2007) found that morphology techniques were required. These techniques were applied to the image shown in Figure 3.5 after inversion. Following the inversion of the

enhanced image, the morphology techniques were applied. These morphology techniques involved dilation and erosion of the image to add or remove pixels at the boundary of the identified objects. The '`strel`' function was used to create a structural element for the application of the '`imdilate`' function to dilate the image, to create more defined and more complete object boundaries. The dilation distance was set at a default value of 3, but could be adjusted by the user to any positive integer. An inverted, dilated image is shown below in Figure 3.6.

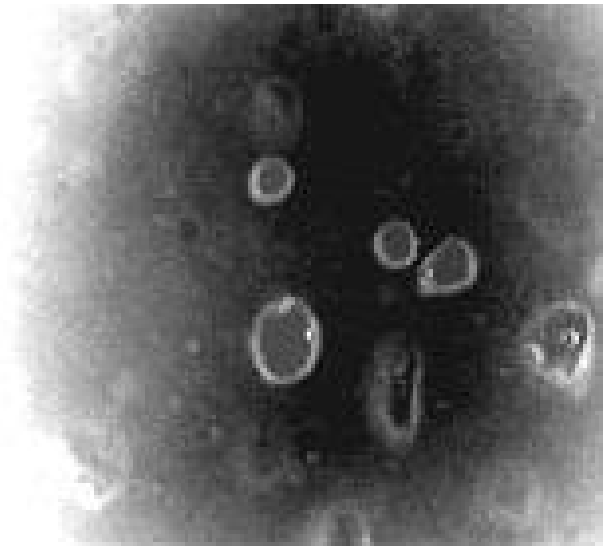

Figure 3.6: Image following inversion and dilation. Image at 7.88 vol% alkane, 5 g/l corn flour and 2 cm/s superficial gas velocity

Following this dilation, the objects were filled using the '`imfill`' function and the image converted to a binary image using the '`im2bw`' function with a default threshold of 65. Bubbles which crossed the image border were incomplete and were removed using the '`imclearborder`' function. This function had a connectivity value of either 4 or 8, which defined the number of connected neighbourhoods for object removal (The Mathworks Inc, 2014b). An example of a binary image, in which objects have been filled is shown in Figure 3.7, below.

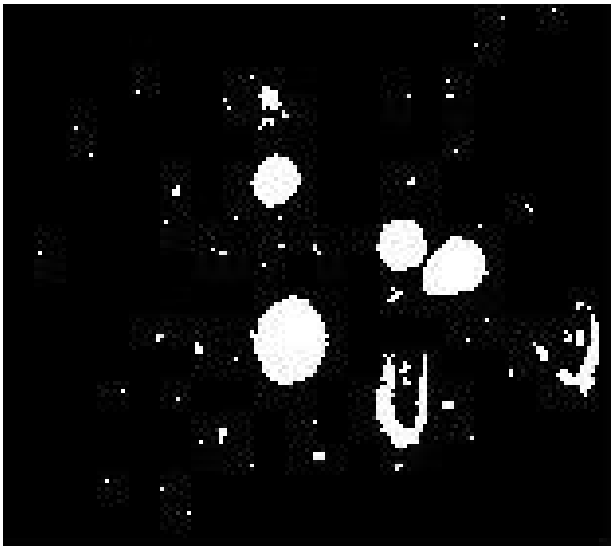

Figure 3.7: Binary image following filling of detected objects. Image at 7.88 vol% alkane, 5 g/l corn flour and 2 cm/s superficial gas velocity

To restore the original image data, the image was eroded back to the original dimensions using the '`imerode`' function. Before data was extracted from the image, the noise was removed using the '`bwareaopen`' function based on a threshold pixel size limit. This function removed all objects with a pixel size lower than the user defined threshold value, based on the assumption that objects below a certain size were false detections (or noise) in the analysis. The image after noise removal is shown in Figure 3.8.

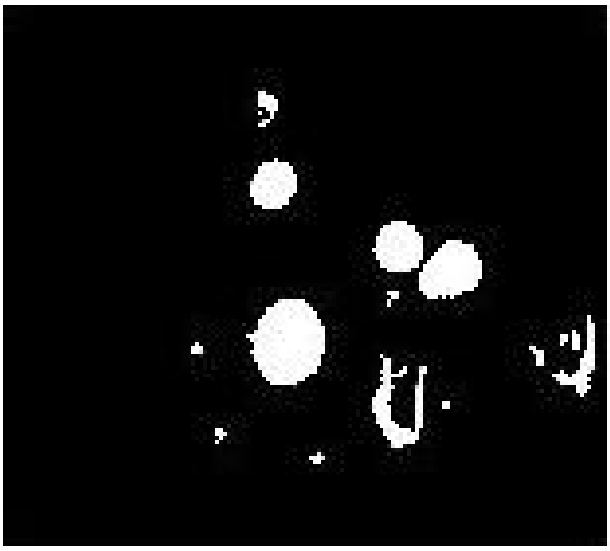

Figure 3.8: Image prior to contrast enhancement and median filtering. Image at 7.88 vol% alkane, 5 g/l corn flour and 2 cm/s superficial gas velocity

3.3.2.3 Boundary Detection and Data Extraction

Once the image had been fully processed, the exterior object boundaries were defined using the 'bwboundaries' function. This function returned an array defining the boundaries in a binary image. The use of the 'noholes' parameter increased the performance of the function by excluding the boundaries of the holes and only identified the exterior boundaries (The Mathworks Inc, 2014c). These boundaries were then superimposed onto the original image, as shown in Figure 3.9, providing a visual representation of the accuracy of the image analysis.

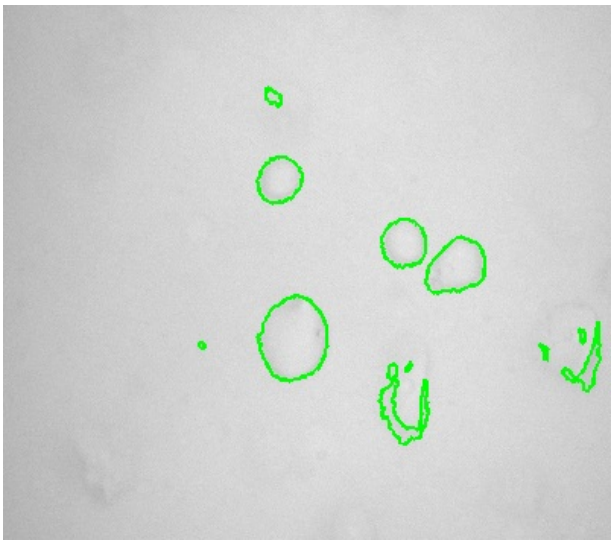

Figure 3.9: Detected boundaries superimposed into original image. Image at 7.88 vol% alkane, 5 g/l corn flour and 2 cm/s superficial gas velocity

To obtain the metric size of the identified bubbles, a scaling parameter was required. An interactive tool was used to allow the user to indicate a reference line of known length on the original image. The length of the reference line was then entered as an input and the scaling conducted to convert from a pixel length to a mm length according to Equation 3.2.

$$Scale = \frac{L_{mm}}{L_{pixel}} \tag{3.2}$$

The function 'regionprops' was then used to extract the object properties. This function provided the area, eccentricity, major and minor axis lengths, perimeter and centroid of each object. The sphericity (between 0 and 1) of individual objects was then calculated according to Equation 3.3. A sphericity of 1 indicated a circle, while values less than 1 indicated deviation from a circular object.

$$Sphericity = \frac{4\pi A}{P^2} \tag{3.3}$$

where A represents the bubble area and P, the perimeter.

Based on a visual investigation of image results, it was determined that a minimum sphericity of 0.76 provided an accurate distinction between bubbles and shadows or poorly defined bubble edges. All objects with a sphericity lower than 0.76 were discarded as false readings.

The bubbles with sphericity greater than the threshold value were then marked and numbered on the original image, as shown in Figure 3.10. The projected area, equivalent diameter, sphericity and coordinates of these bubbles were written to a spreadsheet using the '`xlswrite`' function for use in further calculations.

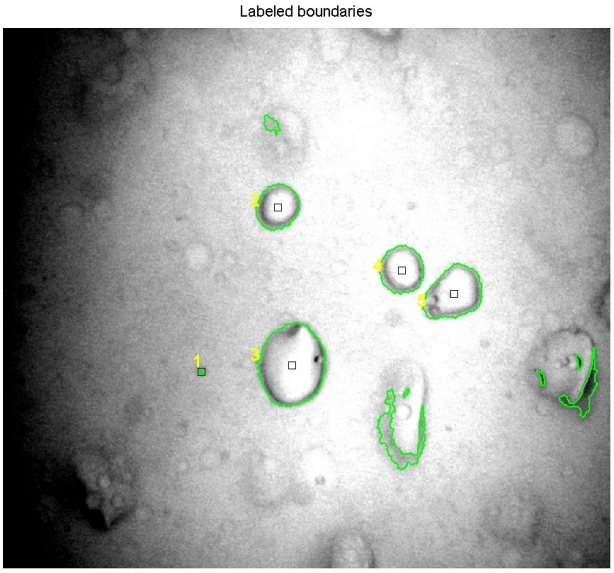

Figure 3.10: Processed image with bubbles labelled and numbered. Image at 7.88 vol% alkane, 5 g/l corn flour and 2 cm/s superficial gas velocity

3.3.3 Measurement of Gas-Liquid Interfacial Area

The data extracted by the MATLAB® '`regionprops`' function provided the equivalent diameter of each of the detected bubbles, which was used to calculate D_{32}. The equivalent diameter is the diameter of a circle with the same surface area, A_p, as the detected bubble (The Mathworks Inc, 2012). Equivalent bubble diameter is also referred to as the Feret diameter, D_F, and was computed according to Equation 3.4 (Mena, 2005).

$$D_F = 2\sqrt{\frac{A_p}{\pi}} = d_m \tag{3.4}$$

To describe the bubble dynamics, a statistical parameter, D_{32}, was used. D_{32} defines the statistical average of bubble diameters in the system and was defined according to d_m, equivalent to D_F (Das *et al.*, 1985; Bouaifi *et al.*, 2001; Vega-Alvarado and Cordova, 2004; Junker, 2006) according to Equation 3.5.

$$D_{32} = \frac{\sum_{i=1}^{N_m} n_i d_{m,j}^3}{\sum_{i=1}^{N_m} n_i d_{m,j}^2} \tag{3.5}$$

ϵ_G defines the volume fraction occupied by the gas phase, and is require to calculate the interfacial area in the system. To determine ϵ_G, the height of the liquid in the column was measured with no aeration, H_0, and again once the air sparging was at steady state at a set u_G, H. The difference between the liquid height in the sparged and unsparged system were used to calculate ϵ_G according to Equation 3.6.

$$\epsilon_G = \frac{H - H_0}{H} \tag{3.6}$$

Using D_{32} and ϵ_G, the gas-liquid interfacial area was calculated according to Equation 3.7. The validity of this calculation is based on the assumption that all detected bubbles were spherical (Mouza *et al.*, 2005; Correia, 2007).

$$a = \frac{6\epsilon_G}{D_{32}} \tag{3.7}$$

3.4 Measurement of the Overall Volumetric Oxygen Transfer Coefficient

To determine K_La in the model hydrocarbon bioprocess, Equation 2.3 was used. This section details the measurement of the τ_P as well as the measurement of the DO behaviour to which K_La was fitted by iterative procedure.

3.4.1 Measurement of the Probe Response Lag

The probe response time is defined by τ_P, the inverse of which is K_P. To measure τ_P, the DO probe was placed in a nitrogen saturated vessel until the calibrated DO sensor reached 0% DO.

Once the probe read 0% DO, it was quickly transferred to the air saturated BCR and the $\frac{C_P}{C_P^*}$ was recorded at 5 second intervals until DO saturation was reached.

To confirm the repeatability of these results, the measurement was conducted 3 times at each process condition (reproducibility is shown in Appendix A.7.

The probe response has been shown to behave as a first order model (Fuchs *et al.*, 1971), where τ_P is defined as the time taken for the DO measurement to reach 63.2% of the saturation DO concentration. To calculate τ_P, linear interpolation was used, based on a plot of $\frac{C_P}{C_P^*}$ values against time An example of a probe response curve is shown in Figure 3.11.

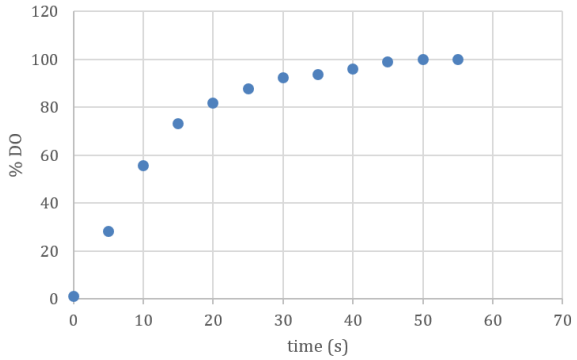

Figure 3.11: Example of probe response data

3.4.2 Incorporation of K_P in the Measurement of K_La

The initial estimate of K_La was determined according to the GOP method discussed in Section 2.2.1. The calibrated DO probe was inserted into the nitrogen sparged BCR (0% DO). A step change in the sparge gas composition was introduced and the DO response ($\frac{C_P}{C^*}$) was recorded at 5 second intervals until air saturation was reached.

The initial estimate of K_La was calculated as described in Section 2.2.1 and was based on the assumption of negligible K_P (Equation 2.1). This estimate was used to ensure model convergence in the calculation of K_La according to Equation 2.3.

Equation 2.3 was used to construct an estimated $\frac{C_P}{C_P^*}$ curve, based on the initial estimate of K_La. These estimated values were then compared to experimental values of $\frac{C_P}{C_P^*}$. The K_La value was iteratively adjusted, using the `lsqcurvefit` function in MATLAB®, to fit the estimated data to the experimental measurement. The source code is provided in Appendix A.4.

3.5 Experimental and Statistical Design

3.5.1 Experimental Design

To evaluate the oxygen transfer behaviour in a model hydrocarbon bioprocess, all variables which potentially influence the oxygen transfer rate must be rigorously evaluated. Based on an evaluation of the literature, several important factors were identified, and their influences on oxygen transfer were evaluated. These variables were alkane concentration, solids loading and u_G. A central composite design was selected to provide sufficient data to identify and statistically evaluate model trends. This experimental design offered a full factorial set of experiments as well as central and axial data points for model development. This was included since previous studies (Correia *et al.*, 2010) showed a peak value of oxygen transfer at alkane concentrations around 5 vol% with an $n - C_{10-13}$ alkane cut. An alpha parameter of 1.414 was selected to define the axial CCD points and to provide the levels typically found in bioprocesses. An n value of 2 was chosen as a sufficient replicate of the central experimental points and to ensure reproducibility of experimental data.

The alkane concentration was varied between 2.5 and 20 vol %, solids loading was evaluated in the range of 0.5 - 6 g/l and u_G between 1 - 3 cm/s. The selected factors and ranges were used to develop the central composite design experiments, provided in Table 3.4. Each experiment was conducted in triplicate to ensure the reproducibility and accuracy of results. This allowed a comprehensive evaluation of the oxygen transfer behaviour. The oxygen transfer behaviour was evaluated by measurement of the ϵ_G, D_{32}, interfacial area, K_P and K_La for each experiment. The experimental results can be found in Appendix A.7

Table 3.4: Experimental Conditions - Conducted in triplicate

	Alkane Concentration	Solids Loading	Superficial Velocity
1	7.88	1.62	1.62
2	7.88	1.62	2.38
3	7.88	4.88	1.62
4	7.88	4.88	2.38
5	14.62	1.62	1.62
6	14.62	1.62	2.38
7	14.62	4.88	1.62
8	14.62	4.88	2.38
9	2.50	3.25	2.00
10	20.00	3.25	2.00
11	11.25	0.50	2.00
12	11.25	6.00	2.00
13	11.25	3.25	1.00
14	11.25	3.25	3.00
15 (C)	11.25	3.25	2.00
16 (C)	11.25	3.25	2.00

3.5.2 Statistical Analysis Procedure

The statistical models were constructed and tested at a 95% confidence interval for all experiments. From the collected data, a Pareto chart, shown for all results, and normal probability plot were constructed to determine which factors (main effects, quadratic effects and linear interactions) were statistically significant at the 95% confidence level.

All statistically non-significant terms were pooled into the error and an ANOVA table was constructed to assess the model regression. Based on the model regression, the statistical model was further refined. Once the model was refined, residual plots were constructed to test the model.

Several residual plots were constructed to test the model fit, the constant vari-

ance assumption and the independence assumption. These plots included a normal plot, a plot of observed values against residuals and a plot of the case numbers against the residual values. Any failure of the data to meet these requirements resulted in repetition of experiments and reanalysis of the experimental data.

Once the statistical model was established and completely refined, surface plots and regression models were constructed, according to Equation 3.8, to allow interpretation of results. Surface plots were constructed with one parameter remaining constant at the midpoint value. The changes in the model were evaluated by plotting these surface plots at low and high constant values to comprehensively evaluate the model behaviour.

$$y = \beta_0 + \sum_i \beta_i x_i + \sum_{i<j} \beta_{ij} x_i x_j + \sum_i \beta_i \beta_{ii} x_i^2 + \epsilon \tag{3.8}$$

To represent the reproducibility of measured data, the average of each measured response variable was plotted against the measured values for the experimental run. Based on the repeatability of the data, the use of averages did not provide a skewed view of the data reproducibility. These plots are provided in Appendix A.7.

Chapter 4

Results and Discussion

Deconstruction of a model hydrocarbon bioprocess with corn flour solids was conducted to facilitate complete understanding of oxygen transfer behaviour with changes in system parameters (u_G, alkane concentration and solids loading). This required the measurement of K_La as well as the interfacial area which underpins the K_La behaviour. To achieve this, the interfacial area was determined from measured D_{32} and ϵ_G.

Following an evaluation of the interfacial area behaviour, the K_La was measured (according to the procedure in Section 3.4). This involved the measurement of the K_P value at each experimental point to accurately account for the influence of the probe response on K_La. The trends identified for interfacial area were used to evaluate the behaviour underpinning the K_La behaviour.

To further the understanding of model hydrocarbon bioprocesses, the interfacial area was also evaluated for non-viable yeast. The trends found in yeast systems were compared to those found for inert solids and this was used to facilitate an understanding of the influence of particle properties on the interfacial area behaviour in the BCR.

4.1 Evaluation of Interfacial Area Behaviour in a Model Hydrocarbon Bioprocess Containing Inert Solids

Accurate measurement of D_{32} is necessary for correct calculation of interfacial area (Equation 3.7). The standard deviation between replicates was below 10% (reported as reasonable for image analysis in review conducted by Junker (2006)) for all experimental conditions.

4.1.1 Dependence of Sauter Mean Diameter on System Parameters

D_{32} data for corn flour systems ($d_p = 13.36\mu m$) determined from the projected bubble area as calculated using the algorithm described in Section 3.3.2, was statistically analysed and standardized effects were represented in the Pareto plot in Figure 4.1, with the 95% confidence interval indicated.

The Pareto plot shows that the most significant parameter influencing D_{32} in the system with corn flour solids is the linear and quadratic influence of u_G. While

the interaction between alkane concentration and u_G (1Lby3L, on the Pareto plot) where not indicated as significant, the fit of the model was substantially improved with the inclusion of this interaction effect.

The other main linear and quadratic effects, alkane concentration and solids loading, were not significant to influence the D_{32}. In addition, the effect of interaction between alkane concentration and solids loading (1Lby2L) and interaction between u_G and solids loading (2Lby3L) were also not significant to influence D_{32}.

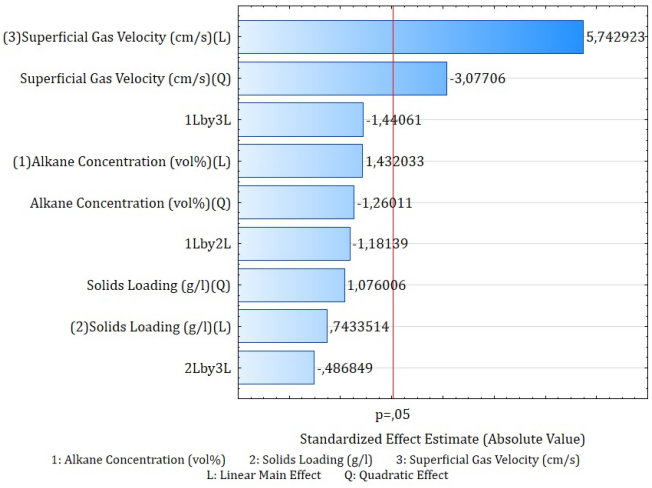

Figure 4.1: Pareto plot from basic statistical model defining the standardized effects on D_{32} in corn flour with 95% confidence level indicated

4.1.1.1 Dependence of Sauter Mean Diameter on Alkane Concentration and Superficial Gas Velocity

Figure 4.2 represents the behaviour of D_{32} with changes in alkane concentration and u_G at constant solids loading (3.25 g/l). This figure shows an increase in D_{32} with increasing alkane concentration at low u_G. As the alkane concentration is increased, the dispersion viscosity also increases and results in greater tendency for coalescence (Mouza *et al.*, 2005) and therefore a greater D_{32}.

As u_G was increased to around 2.2 cm/s, the increase in D_{32} with increasing alkane concentration became less pronounced. As the alkane concentration was increased, the surface tension of the dispersion decreased and resulted in an increase in the tendency for bubble breakup. Simultaneously, the increase in alkane concentration increased the dispersion viscosity and enhanced the tendency for bubble coalescence. Dumont *et al.* (2006); Morao *et al.* (1999) and Kawase and Moo-Young (1990) suggested that at higher u_G, the bubble breakup and coalescence occurred at similar rates and therefore alkane concentration did not have a marked influence on D_{32} at this u_G.

As u_G was further increased, a slight decrease in D_{32} was observed. The increase in alkane concentration in a more turbulent environment resulted in a greater number of alkane droplets in the dispersion. This allowed for more attrition by the alkane droplets, and caused a higher occurrence of bubble breakup in the column, which possibly overcame the effect of increased viscosity on coalescence. The alkane used has shown a tendency to form beads (unpublished work, Hollis), which supported the hypothesis that high alkane concentrations at high u_G would increase the tendency for attrition of bubbles by alkane droplets.

Figure 4.2 also indicated an increase in D_{32} with an increase in u_G. This increase in D_{32} correlated to findings of Camarasa *et al.* (1999), where D_{32} increased with u_G in a porous sparger BCR. This was attributed to an increase in bubble formation time at the sparger and therefore an increase in the size of the bubbles developed at the sparger surface.

However, an increase in u_G above 2.4 cm/s results in a decrease in D_{32} at higher alkane concentration. It is suggested that this is due to a shift in bubble size distribution, where large and small bubbles begin to form at the start of a transition regime. Camarasa *et al.* (1999) suggested that at high u_G in a high viscosity dispersion, smaller bubbles are formed at the sparger.

Since solids loading does not influence the behaviour of D_{32}, the model indicated the same behaviour at low and high solids loading. These figures can be found in Appendix A.8.1.

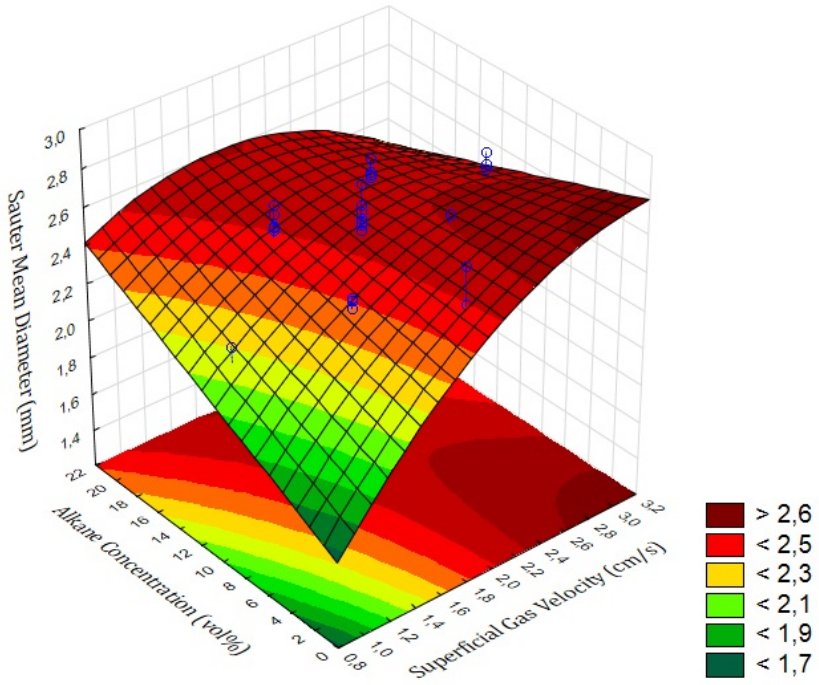

Figure 4.2: Influence of superficial gas velocity and alkane concentration on D_{32} in corn flour at constant solid loading (midpoint at 3.25 g/l)

4.1.1.2 Dependence of Sauter Mean Diameter on Alkane Concentration and Solids Loading

From Figure 4.3 it is evident that at constant u_G the solids loading did not influence D_{32} at any alkane concentration within the parameter range of the experiments. The influence of corn flour solids on the D_{32} has not been described in literature, but the low shear forces in the BCR (Bouaifi *et al.*, 2001) may prevent the bubble breakup in the homogeneous regime.

At low constant u_G, the D_{32} is lower and the D_{32} is higher at higher constant u_G. This supports the findings of Camarasa *et al.* (1999) where D_{32} was found to be dependent only on the size of bubbles formed at the sparger in an aqueous dispersion in a porous sparger BCR. These are provided in Appendix A.8.2.

Figure 4.3, indicates a linear increase in D_{32} with increasing alkane concentration. This trend can be attributed to the increase in viscosity which inhibits bubble breakup as discussed in Section 4.1.1.1. At low constant u_G, the rate of increase in D_{32} is lower than at higher constant u_G (shown in Appendix A.8.2).

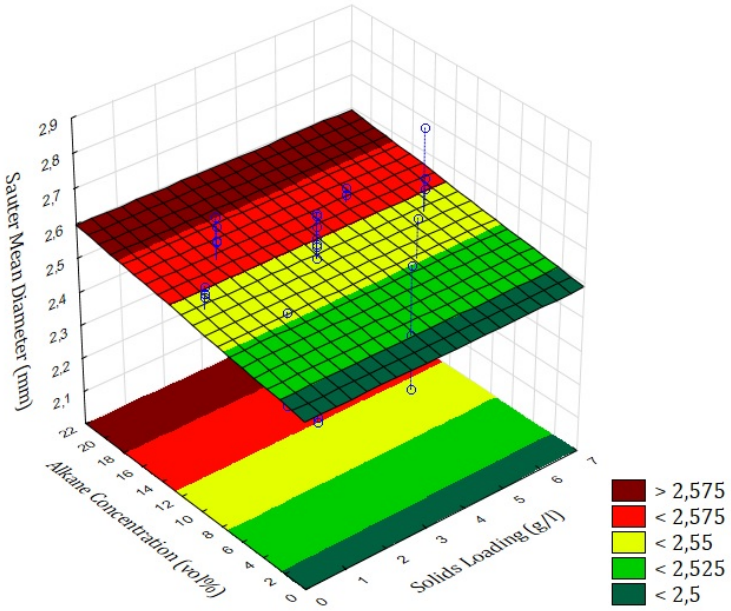

Figure 4.3: Influence of alkane concentration and solid loading on D_{32} in corn flour at constant superficial gas velocity (midpoint at 2 cm/s)

4.1.1.3 Dependence of Sauter Mean Diameter on Superficial Gas Velocity and Solids Loading

Figure 4.4 shows the behaviour of D_{32} with u_G and solids loading at constant alkane concentration (11.25 vol%). This surface plot confirms that solids did not

influence D_{32} in the range considered. Similar surface plots were observed at low and high constant alkane concentration, provided in Appendix A.8.3.

Figure 4.4 clearly indicates changes in D_{32} with increased u_G. D_{32} experienced an initial increase with increasing u_G, a likely consequence of the increase in the size of bubbles formed at the sparger. This D_{32} behaviour was also shown in Figure 4.2, and was discussed in Section 4.1.1.1. Above 2.4 cm/s, the D_{32} started to decrease as a likely result of a transition in operating regime, discussed in Section 4.1.1.1. In addition, at high u_G, the decrease in D_{32} could have been a consequence of attrition by alkane droplets, which behaved as beads in the dispersion (unpublished work, Hollis).

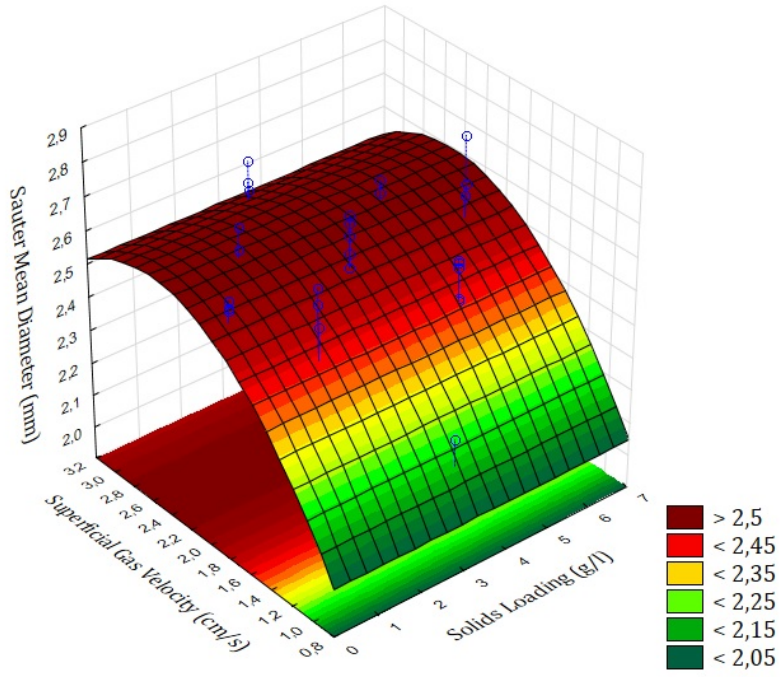

Figure 4.4: Influence of gas velocity and solid loading on D_{32} in corn flour at constant alkane concentration (midpoint at 11.25 vol%)

4.1.2 Dependence of Gas Holdup on System Parameters

The ϵ_G was determined using Equation 3.6 and a statistical analysis of the data provided the Pareto plot in Figure 4.5 with the 95% confidence interval indicated. The behaviour of ϵ_G in systems with corn flour solids showed a significant dependence on u_G. This plot did not indicate any dependence on alkane concentration or solids loading and ϵ_G was not significantly influenced by the interaction between any system parameters in the range considered.

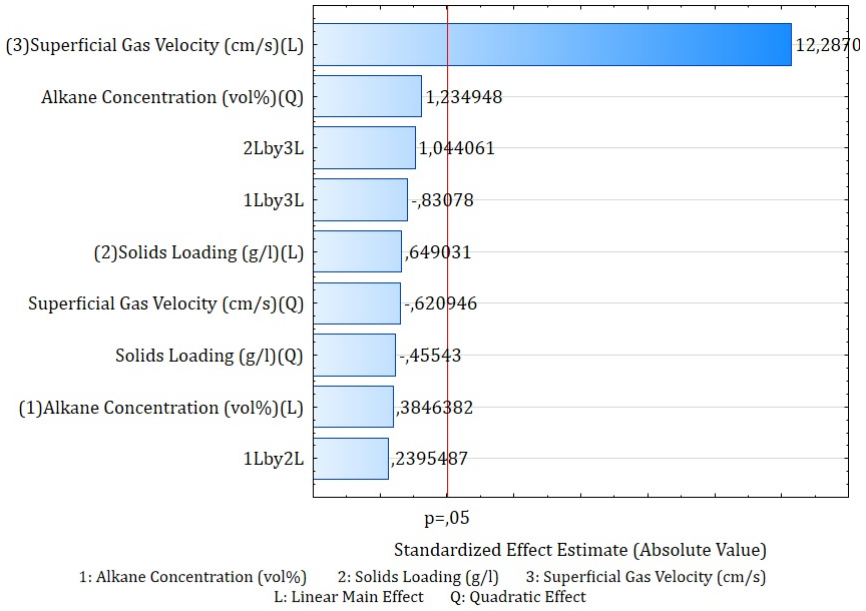

Figure 4.5: Pareto plot from basic statistical model defining the standardized effects on ϵ_G in corn flour with 95% confidence level indicated

4.1.2.1 Dependence of Gas Holdup on Alkane Concentration and Superficial Gas Velocity

The influence of u_G and alkane concentration on ϵ_G at constant solids loading of 3.25 g/l (shown in Figure 4.6) indicated that the alkane concentration did not have an influence on the ϵ_G behaviour over the entire range of u_G. At low and high constant solids loading, similar behaviour was observed with alkane concentration. These surface plots are presented in Appendix A.9.1.

However, ϵ_G increases linearly with increasing u_G at all alkane concentrations in the range considered. The linear increase in ϵ_G with u_G indicated that the column operated in the homogeneous regime (described in Section 2.3.3.2). Mouza *et al.* (2005) reported that as u_G was increased in the homogeneous regime, the number of bubbles in the column increased and interfered with the bubble rise velocity. This interference kept bubbles in the dispersion and increased ϵ_G.

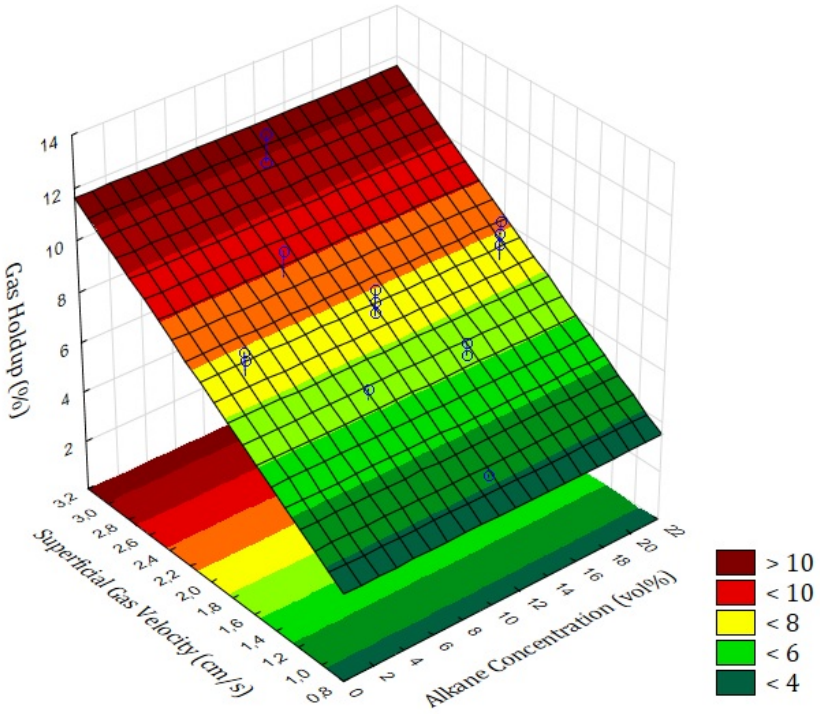

Figure 4.6: Influence of superficial gas velocity and alkane concentration on ϵ_G in corn flour at constant solid loading (midpoint at 3.25 g/l)

4.1.2.2 Dependence of Gas Holdup on Superficial Gas Velocity and Solids Loading

The influence of u_G and solids loading on ϵ_G at constant alkane concentration is shown in Figure 4.7. An increase in solids loading did not influence ϵ_G in the range of u_G considered. Similar behaviour was observed at low and high constant alkane concentration and these surface plots are shown in Appendix A.9.2.

However, a linear increase in ϵ_G was observed with increasing u_G over the range of solids loadings considered. This behaviour was also shown in Figure 4.6 and indicated that the BCR operated in the homogeneous flow regime.

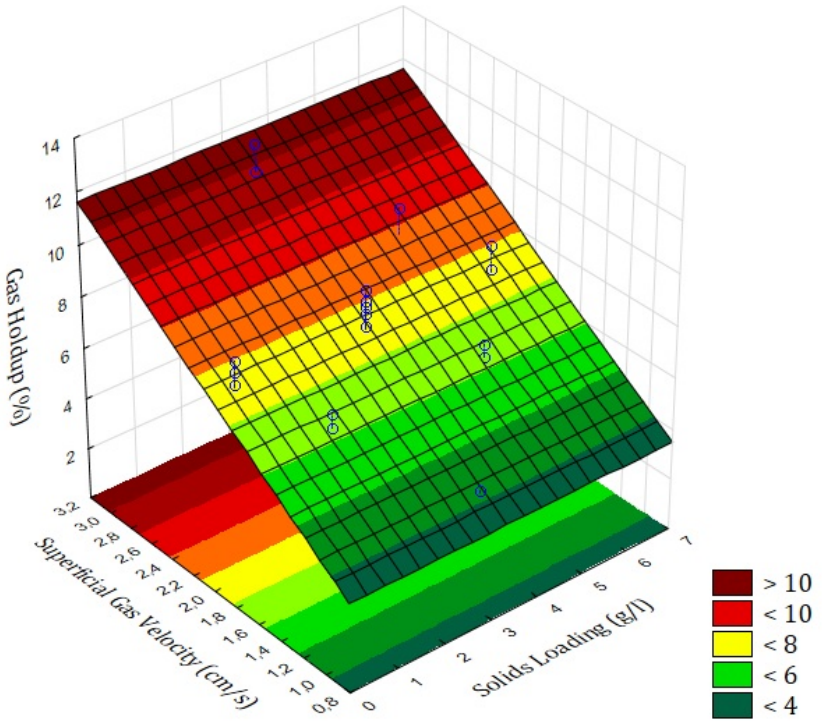

Figure 4.7: Influence of superficial gas velocity and solids loading on ϵ_G in corn flour at constant alkane concentration (midpoint at 11.25 vol%)

4.1.2.3 Dependence of Gas Holdup on Alkane Concentration and Solids Loading

Alkane concentration and solids loading did not have an influence on the ϵ_G and remained constant at 7.38% for all alkane concentration and solids loadings in the range considered. This was experimentally confirmed and is represented by the surface plot shown in Figure 4.8. This behaviour was also observed in Figure 4.6 and Figure 4.7 and confirms the statistical findings shown in Figure 4.5.

At low u_G (constant at 1.62 cm/s), a constant ϵ_G value of 6.27% for all alkane concentrations and solids loadings was observed. At high u_G (constant at 2.38 cm/s) a constant ϵ_G value of 8.73% was found for all alkane concentration and solids loadings investigated. These surface plots are shown in Appendix A.9.3.

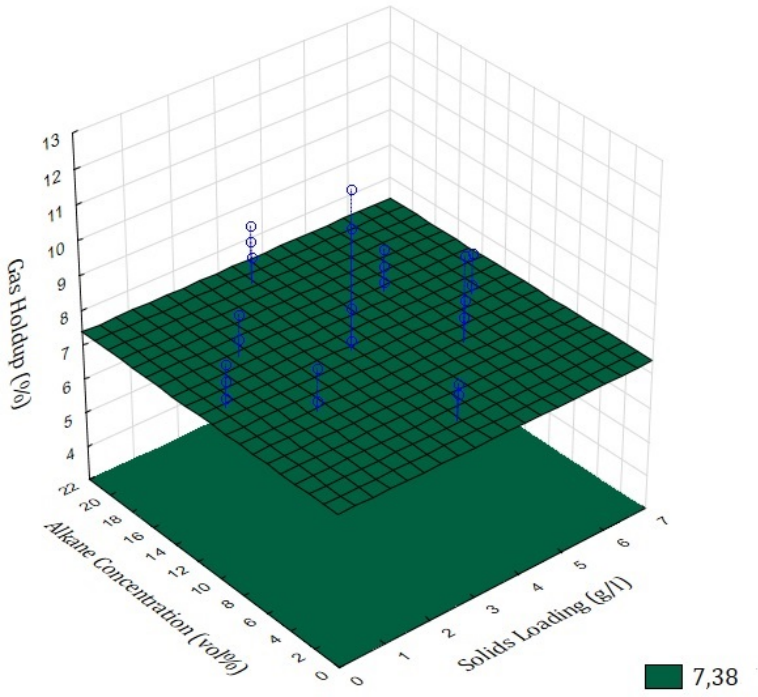

Figure 4.8: Influence of the alkane concentration and solids loading on ϵ_G in corn flour at constant superficial gas velocity (midpoint value of 2 cm/s)

4.1.2.4 Prediction of Gas Holdup

Based on the analyses of ϵ_G behaviour and the statistical analysis shown in Figure 4.5, it was shown that ϵ_G was dependent only on u_G while alkane concentration and solids loading had negligible influence in the range considered. To evaluate the accuracy of this statement, an empirical correlation was developed and is given by Equation 4.1.

$$\epsilon_G = 3.3933 u_G + 0.756 \tag{4.1}$$

A regression analysis of the empirical model for ϵ_G indicated an accuracy of 83.34% for the prediction of ϵ_G. This model was valid across the range of system parameters, alkane concentration (2.5 - 20 vol%), solids loading (0.5 - 6 g/l) and u_G (1 - 3 cm/s). All experimental results are indicated in Figure 4.9 with the empirical model indicated.

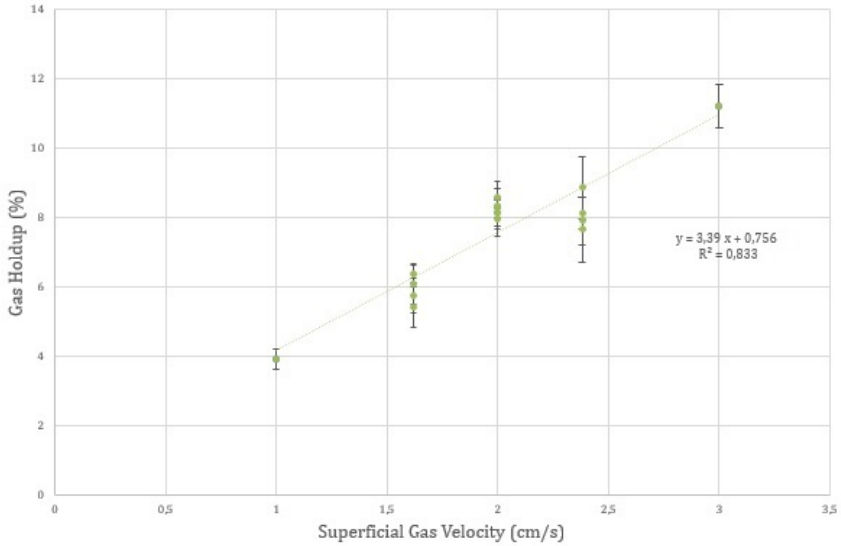

Figure 4.9: Experimental values indicating accuracy of the empirical model for prediction of gas holdup in systems containing corn flour

4.1.3 Dependence of Interfacial Area on System Parameters

The interfacial area was calculated from D_{32} and ϵ_G data according to Equation 3.7. The statistical significance of all system parameters and linear interactions are shown with the 95% confidence level indicated in the Pareto plot in Figure 4.10.

This analysis showed that only the linear effect of u_G was significant at the 95% confidence level. The alkane concentration and solids loading did not influence interfacial area and the interaction between parameters also had no significant influence on interfacial area behaviour.

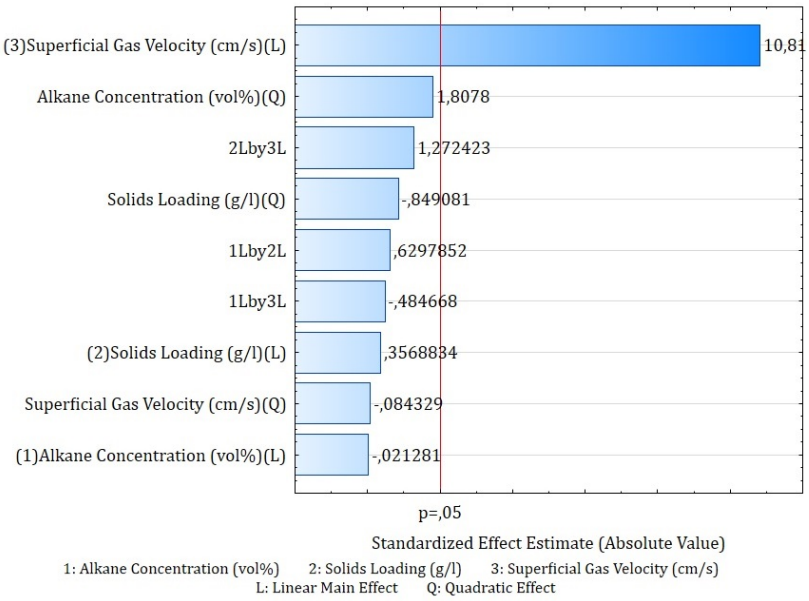

Figure 4.10: Pareto plot from basic statistical model defining the standardized effects on interfacial area in corn flour with 95% confidence level indicated

4.1.3.1 Dependence of Interfacial Area on Alkane Concentration and Superficial Gas Velocity

The behaviour of interfacial area with changes in u_G and alkane concentration is shown in Figure 4.11 at constant solids loading. This figure indicated that the interfacial area was not influenced by the alkane concentration for all u_G values. However, an increase in u_G resulted in a linear increase in the interfacial area at all alkane concentrations. The trends in interfacial area followed the same behaviour as that observed for ϵ_G (shown in Figure 4.6). This indicated that in the current system, the D_{32} did not significantly influence the behaviour of interfacial area. The same behaviour was also found at low and high constant solids loadings, shown in Appendix A.10.1.

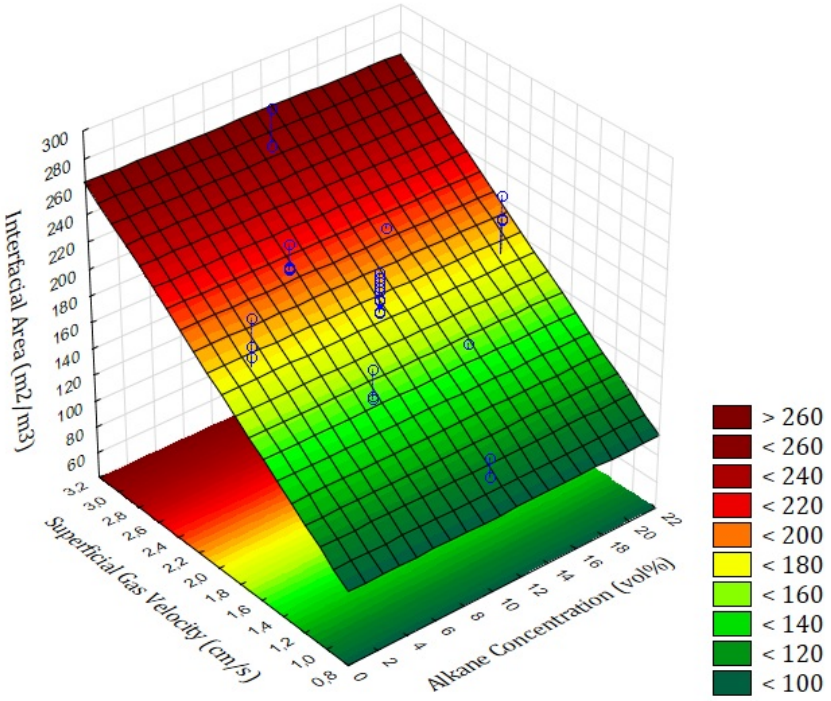

Figure 4.11: Influence of superficial gas velocity and alkane concentration on interfacial area in corn flour at constant solid loading (midpoint at 3.25 g/l)

4.1.3.2 Dependence of Interfacial Area on Superficial Gas Velocity and Solids Loading

The behaviour of interfacial area with u_G and solids loading at constant alkane concentration is shown in Figure 4.12. This figure showed that the interfacial area was not influenced by solids loading for all u_G considered. However, the interfacial area increased linearly with u_G at all solids loadings. This linear relationship between interfacial area and u_G was shown in Figure 4.11. Similar behaviour was observed at low and high constant alkane concentration, provided in Appendix A.10.2.

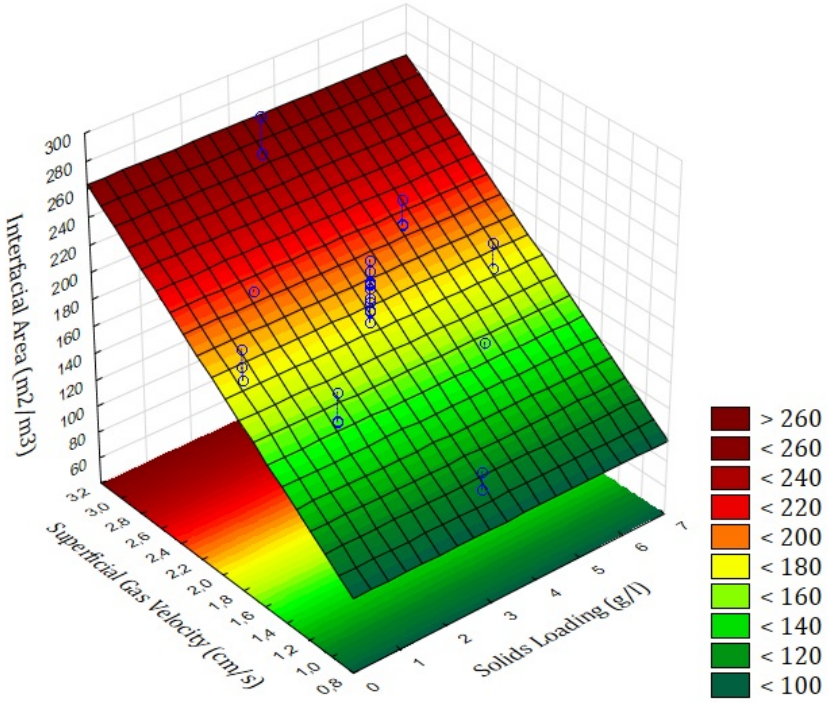

Figure 4.12: Influence of gas velocity and solids loading on interfacial area in corn flour at constant alkane concentration (midpoint at 11.25 vol%)

4.1.3.3 Dependence of Interfacial Area on Alkane Concentration and Solids Loading

The behaviour of interfacial area with alkane concentration and solids loading is shown in Figure 4.13 at constant u_G. This surface plot confirmed the statistical significance shown in Figure 4.10 and indicated that neither alkane concentration nor solids loading influenced interfacial area at constant u_G. This is represented by the constant surface at 179 m^2/m^3.

Similar behaviour was observed at low constant u_G, where a constant interfacial area of 153 m^2/m^3, shown in Figure A.26. At high constant u_G, a constant interfacial area of 206 m^2/m^3 was found, shown in Figure A.27. These are provided in Appendix A.10.3.

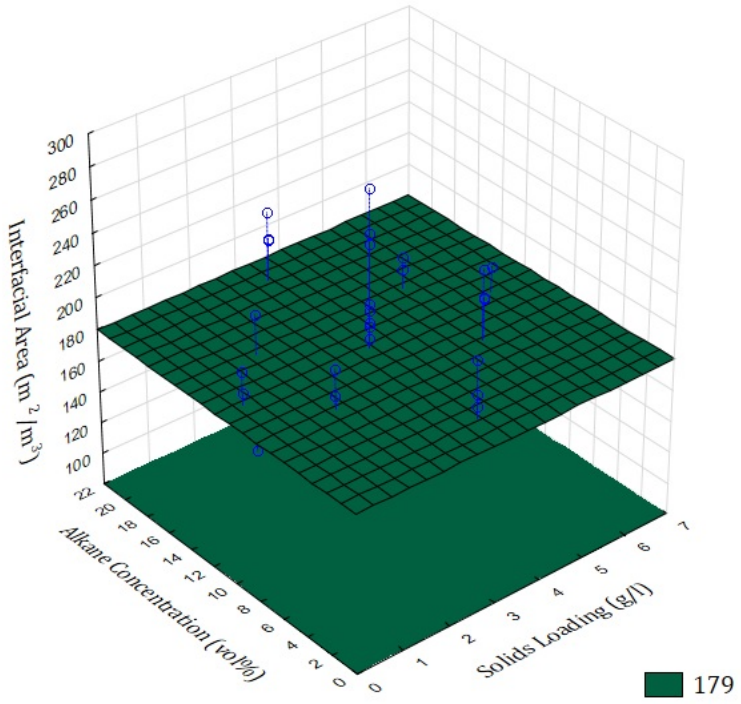

Figure 4.13: Influence of the alkane concentration and solid loading on interfacial area in corn flour at constant superficial gas velocity (midpoint value of 2 cm/s)

4.1.3.4 Prediction of Interfacial Area

The evaluation of the interfacial area behaviour in the model hydrocarbon bioprocess containing inert solids showed that the interfacial area was only influenced by the u_G, with negligible influence of alkane concentration and solids loading (Figure 4.10). This allowed for development of an empirical model to predict interfacial area behaviour for the experimental range evaluated.

The empirical correlation was defined by Equation 4.2 and showed an accuracy of 78.8% for the prediction of interfacial area. The correlation was valid for u_G 1 - 3 cm/s, alkane concentration 2.5 - 20 vol% and solids loading 0.5 - 6 g/l (the experimental range used) and all experimental data is shown in Figure 4.14.

$$Area = 69.665u_G + 40.31 \tag{4.2}$$

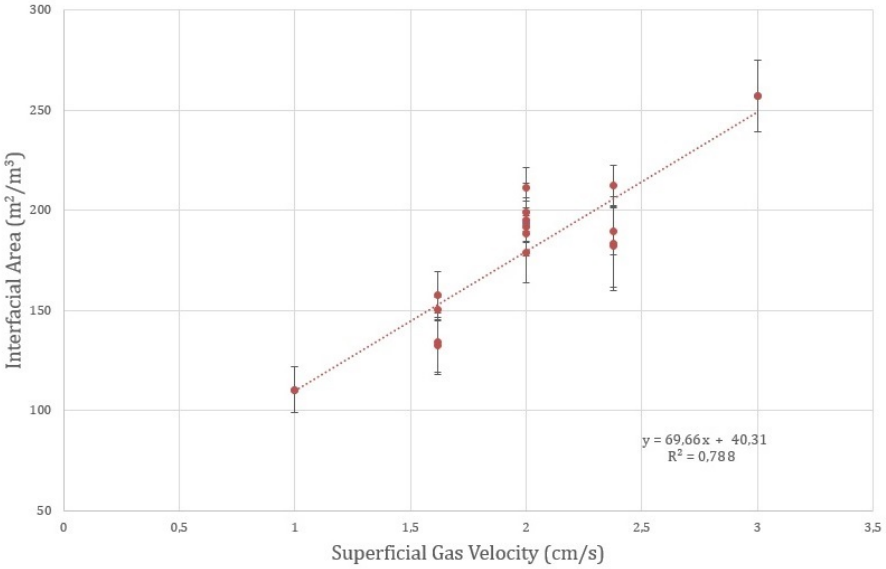

Figure 4.14: Experimental values indicating accuracy of the empirical model for the prediction of interfacial area in ssytems containing corn flour

4.2 Quantification of K_La Accuracy With and Without Consideration of the Probe Response Lag

K_La is often determined according to the GOP described in Section 2.2.1. However, this methodology does not account for the lag associated with the probe. The assumption of negligible probe response can result in a significant underestimation of K_La (Correia and Clarke, 2009; Clarke and Manyuchi, 2012; Tribe *et al.*, 1995).

Figure 4.15 shows the K_La as determined with and without inclusion of K_P. With variation in alkane concentration, the underestimation of K_La varies. Similar behaviour is seen with variation in solids loading, shown in Figure 4.16. In these figures, the K_La is consistently underestimated when K_P is neglected.

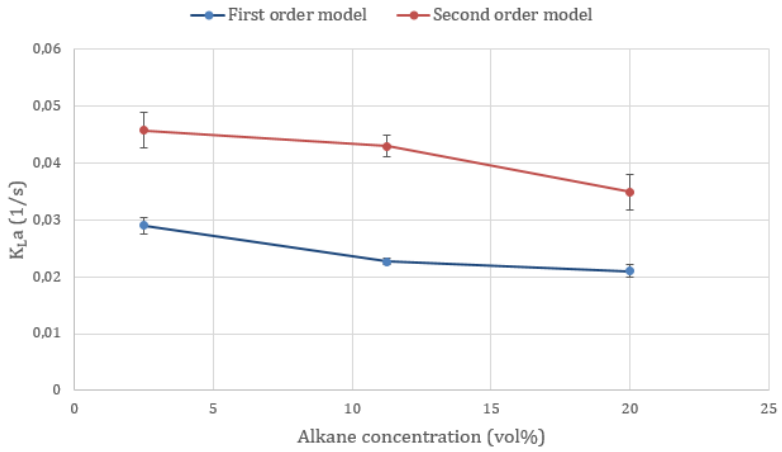

Figure 4.15: Comparison of the K_La as calculated using the first and second order models at constant solids loading (midpoint value of 3.25 g/l) and constant superficial gas velocity (midpoint value at 2 cm/s)

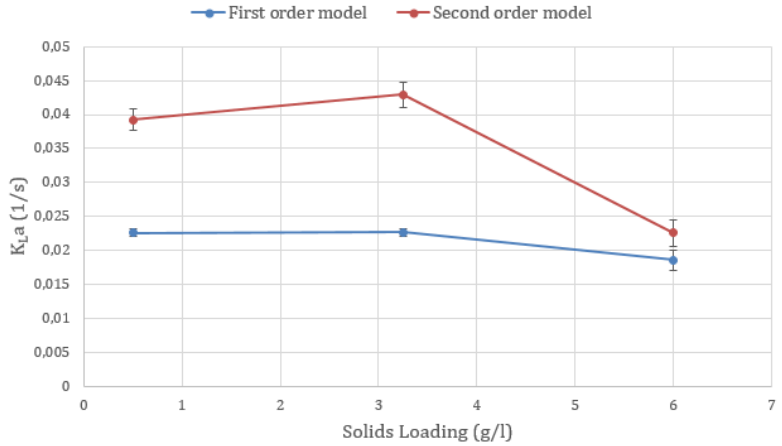

Figure 4.16: Comparison of the K_La as calculated using the first and second order models at constant alkane concentration (midpoint value of 11.25 vol%) and constant superficial gas velocity (midpoint value of 2 cm/s)

Van't Riet (1979) stated that the error introduced by neglecting K_P is less than 6% when K_La is smaller than the inverse of τ_P ($K_La \leq \frac{1}{\tau_P} \approx 0.07s^{-1}$). This relationship suggests that the error introduced by τ_P will be more significant at higher K_La values. This is evidenced in Figure 4.17, where a higher K_La value indicated a greater deviation between K_La measurements with and without consideration of the probe response lag.

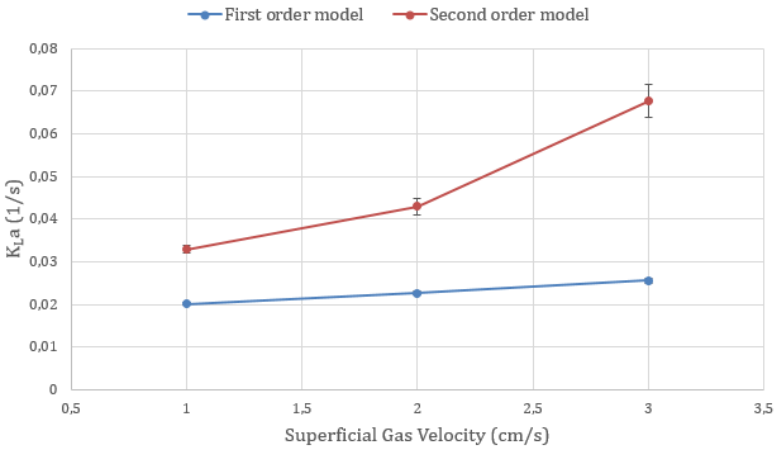

Figure 4.17: Comparison of the K_La as calculated using the first and second order models at constant alkane concentration (midpoint value of 11.25 vol%) and constant solid loading (midpoint value of 3.25 g/l)

4.3 Evaluation of K_La Behaviour in a Model Hydrocarbon Bioprocess Containing Inert Solids

4.3.1 Dependence of K_P on System Parameters

At all experimental conditions, the K_P value was measured and calculated according to the procedure described in Section 3.4.1. These results were measured in triplicate to ensure the repeatability of experiments and ensure correct determination of K_La using Equation 2.3.

The data obtained for K_P was statistically analysed to determine significant parameters at the 95% confidence level. The significance of system parameters and linear interaction of parameters are shown in the Pareto plot in Figure 4.18. This figure indicated that all system parameters and linear interaction between parameters had a significant influence on K_P except u_G.

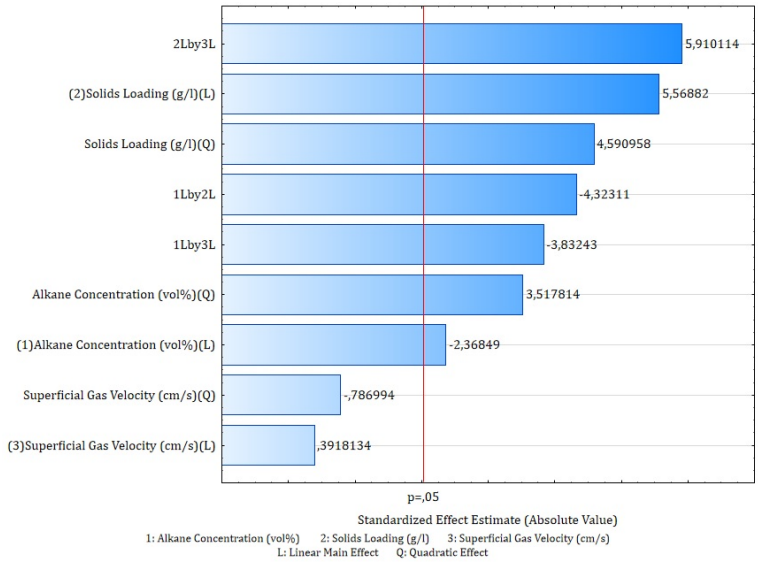

Figure 4.18: Pareto plot from basic statistical model defining the standardized effects on K_P in corn flour with 95% confidence level indicated

The behaviour of K_P with changes in system parameters is not well documented and will require further study to establish and explain trends. The surface plots corresponding to the K_P results obtained here are provided in Figure 4.19, Figure 4.20 and Figure 4.21.

These plots indicate complex interaction of K_P with changes in system parameters. Although Aiba and Huang (1969); Fuchs *et al.* (1971) and Philici and Stenstrom (1989) have reported the dependence of K_P on the properties of the probe, such as the membrane type, membrane thickness, membrane age and the electrolyte usage, the results found here indicate that the K_P was also significantly influenced by the properties of the system in which K_P was measured. Since K_P varies significantly with the dispersion properties, it must be measured at all experimental conditions and the assumption of constant K_P is not valid.

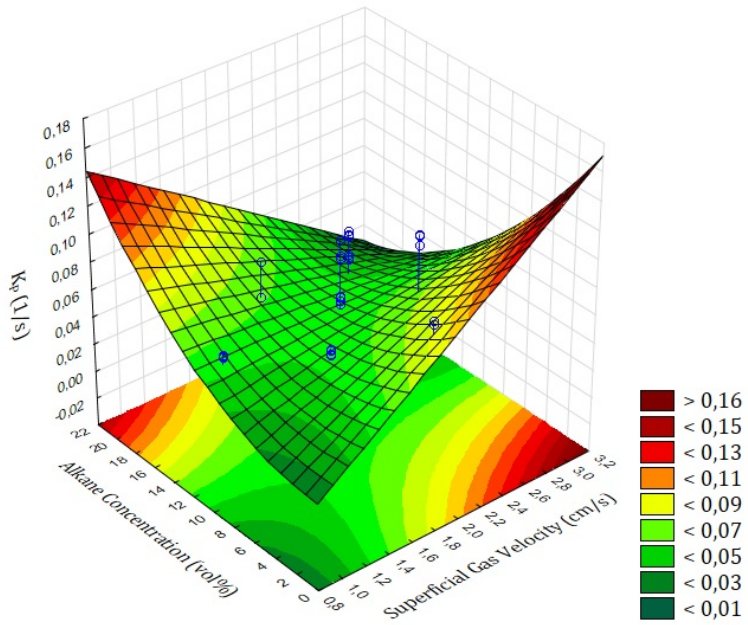

Figure 4.19: Influence of the alkane concentration and superficial gas velocity on K_P in corn flour at constant solids loading (midpoint value of 3.25 g/l)

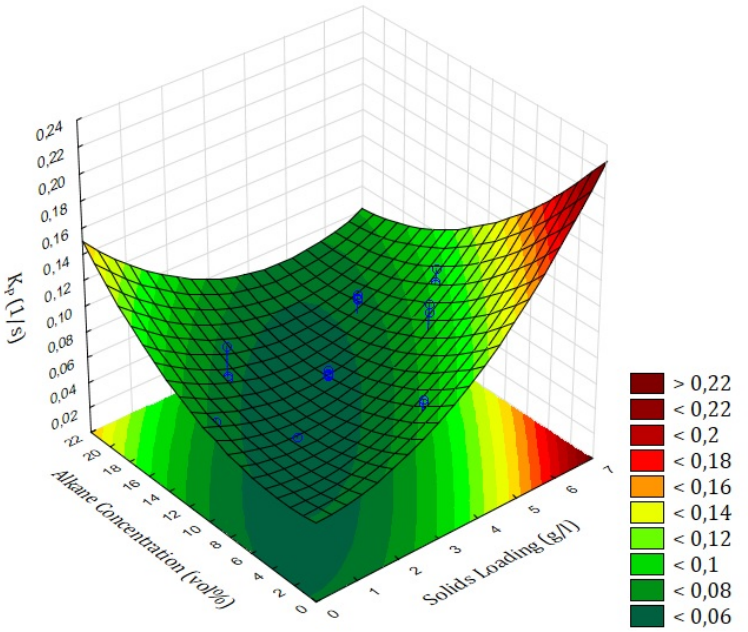

Figure 4.20: Influence of the alkane concentration and solid loading on K_P in corn flour at constant gas velocity (midpoint value of 2 cm/s)

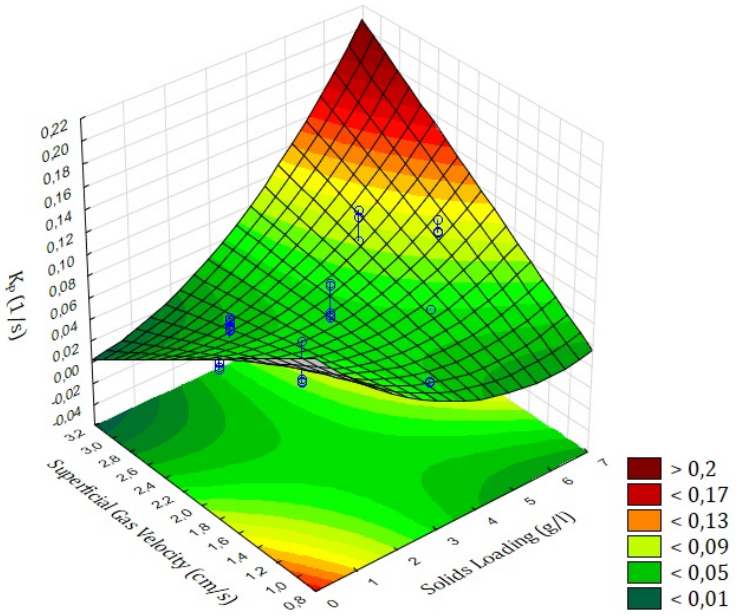

Figure 4.21: Influence of the gas velocity and solid loading on K_P in corn flour at constant alkane concentration (midpoint value of 11.25 vol%)

4.3.2 Dependence of K_La on System Parameters

K_La was calculated according to Equation 2.3 which incorporates the K_P value measured at each experimental condition. These K_La values were statistically analysed to develop a model describing K_La behaviour in the model hydrocarbon bioprocess. The trends observed for interfacial area behaviour (Section 4.1.3) were used to deconstruct the behaviour of K_La in the model hydrocarbon bioprocess and provided understanding of the factors underpinning K_La behaviour in the system.

The statistical analysis of the K_La data, shown in the Pareto plot in Figure 4.22, indicated that all main effects (alkane concentration, solids loading and u_G) influenced the K_La behaviour. Solids loading and u_G also demonstrated significant quadratic influences on K_La. Based on this statistical analysis, no linear interactions between parameters had a significant influence on the K_La at the 95% confidence level.

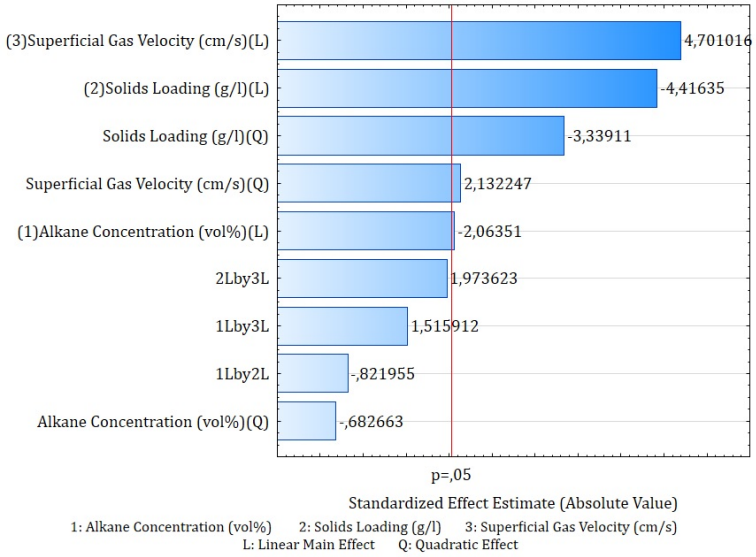

Figure 4.22: Pareto plot from basic statistical model defining the standardized effects on K_La in corn flour with 95% confidence level indicated

4.3.2.1 Dependence of K_La on Alkane Concentration and Superficial Gas Velocity

The behaviour of K_La with alkane concentration and u_G at constant solids loading is shown in Figure 4.23. Similar behaviour of K_La was observed at low and high constant solids loading and these surface plots can be found in Appendix A.12.1.

An increase in K_La was observed with an increase in u_G above 1.4 cm/s. This correlated with the increase in interfacial area associated with increasing u_G, shown in Figure 4.11. This increase was coupled with a more uniform distribution of solid particles, and increased the penetration of particles into the liquid side diffusion film. This resulted in a positive hydrodynamic effect, increasing the K_L (Nguyen-tien *et al.*, 1985; Schumpe and Deckwer, 1987). Coupling of the increased K_L with the increased interfacial area resulted in a substantial increase in the K_La value as the u_G was increased.

However, at low u_G, a slight decrease in the K_La was observed with increasing u_G. At low u_G, there was not enough turbulence in the column to influence the liquid-side film penetration by solids and increase the K_L in the system. This correlated with the findings of Patwari *et al.* (1985), who stated that as viscosity in a BCR was increased, larger particles were required to penetrate the liquid film and cause an increase in K_La.

An increase in alkane concentration resulted in a slight decrease in K_La. This change was a result only of changes in K_L, since the interfacial area did not change with alkane concentration (shown in Figure 4.11). Cascaval *et al.* (2006)

attributed such changes to the increase in dispersion viscosity, which altered the hydrodynamics of the system and resulted in a decrease in the K_L value, and therefore a decrease in system K_La.

A similar decrease in K_La was confirmed by several studies in both STRs and BCRs. Özbek and Gayik (2001) found a decrease in K_La as glycerol concentration was increased in a glycerol-water system. Dumont *et al.* (2006) found a decrease in K_La in an air-water dispersion with the addition of silicone oil. An increase in the concentration of hexadecane in a STR also resulted in a decrease in the K_La value (Nielsen *et al.*, 2003).

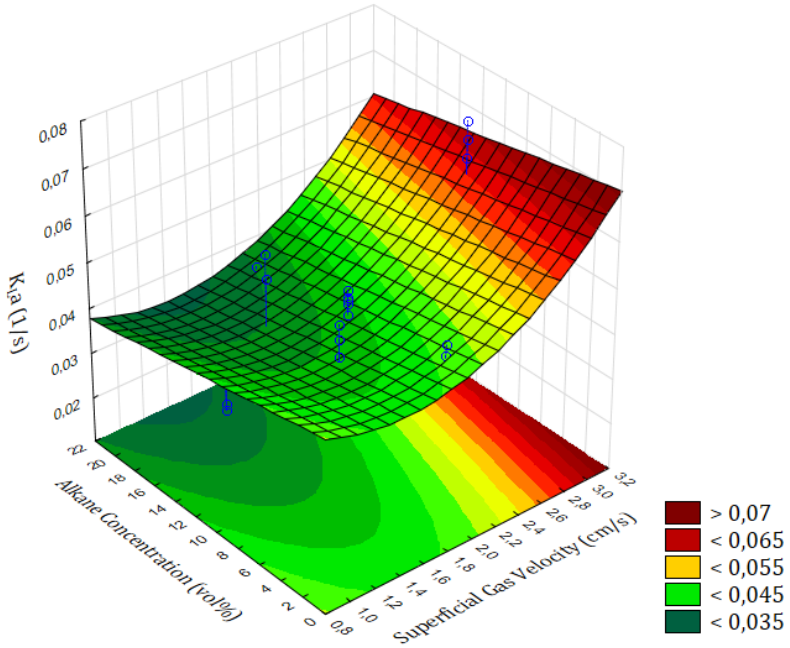

Figure 4.23: Influence of superficial gas velocity and alkane concentration on K_La in corn flour at constant solid loading (midpoint at 3.25 g/l)

4.3.2.2 Dependence of K_La on Alkane Concentration and Solids Loading

The behaviour of K_La with changes in alkane concentration and solids loading at constant u_G is shown in Figure 4.24. This figure showed a similar trend with increasing alkane concentration as the trend shown in Figure 4.23. This behaviour was a result of the decrease in K_L with increasing dispersion viscosity. A similar trend was observed at low and high u_G and these surface plots are provided in Appendix A.12.2.

Consideration of the K_La behaviour with an increase in solids loading indicated an initial increase in K_La, followed by a decrease above 2.5 g/l solids loading. Solids loading did not have an influence on interfacial area (shown in Figure 4.13),

so this behaviour was a result of the K_L behaviour only.

Nguyen-tien *et al.* (1985) and Schumpe and Deckwer (1987) attributed this behaviour in a BCR to the penetration of particles through the liquid-side diffusion film, while Mills *et al.* (1987) reported this as an influence of enhanced interfacial turbulence with low solids loadings (glass beads, 0.1 - 2.5 vol%). Similarly, Yagi and Yoshida (1974) showed that the addition of non-viable microbes to a STR with an aqueous dispersion resulted in a slight increase in the K_L due to the influence on the hydrodynamic conditions at the gas-liquid interface.

As the solids loading was further increased, a decrease in K_La was observed. Chisti and Moo-Young (1988) and Mills *et al.* (1987) suggested that this decrease occurred as a result of diffusion blocking effects in aqueous STRs. Joosten *et al.* (1977) found, in an aqueous dispersion STR using glass beads (53 - 105 μm) an initial increase in K_La followed by a sharp decrease as the solids loading was further increased.

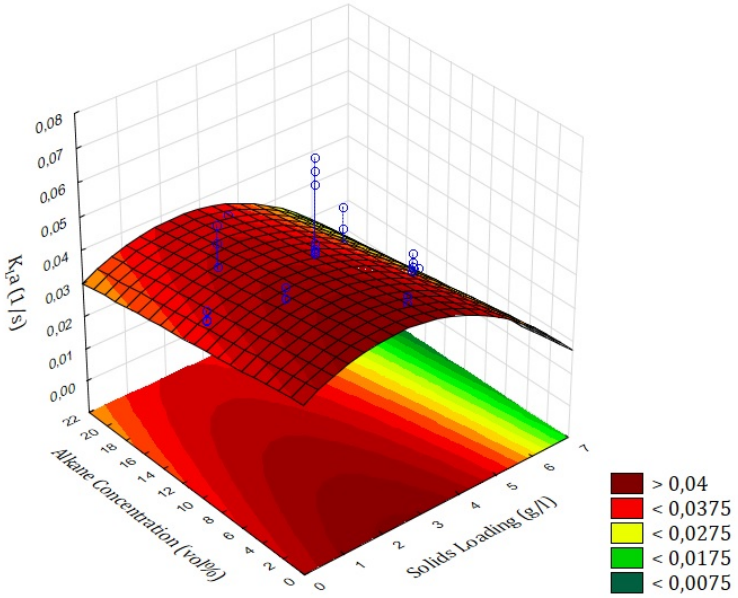

Figure 4.24: Influence of alkane concentration and solids loading on K_La in corn flour at constant superficial gas velocity (midpoint at 2 cm/s)

4.3.2.3 Dependence of K_La on Superficial Gas Velocity and Solids Loading

The influence of u_G and solids loading at constant alkane concentration is shown in Figure 4.25. Similar behaviour was observed at low and high constant alkane concentration and these surface plots are shown in Appendix A.12.3.

The behaviour of K_La with increase in u_G showed similar behaviour to that observed in Figure 4.23 and was largely a result of the increase in interfacial area

(shown in Figure 4.12). The slight initial decrease with increasing u_G was a likely consequence of low liquid-side film penetration, as discussed in Section 4.3.2.1.

As solids loading was increased, similar behaviour to that shown in Figure 4.24 was observed. The initial increase in K_La was attributed to increased interfacial turbulence at low solids loadings and penetration through the liquid-side diffusion film which caused an increase in K_L, as described in Section 4.3.2.2. At solids loadings greater than 2.5 g/l, the decrease in K_La was a likely consequence of the increase in dispersion viscosity, and caused a diffusion blocking effect, decreasing K_L.

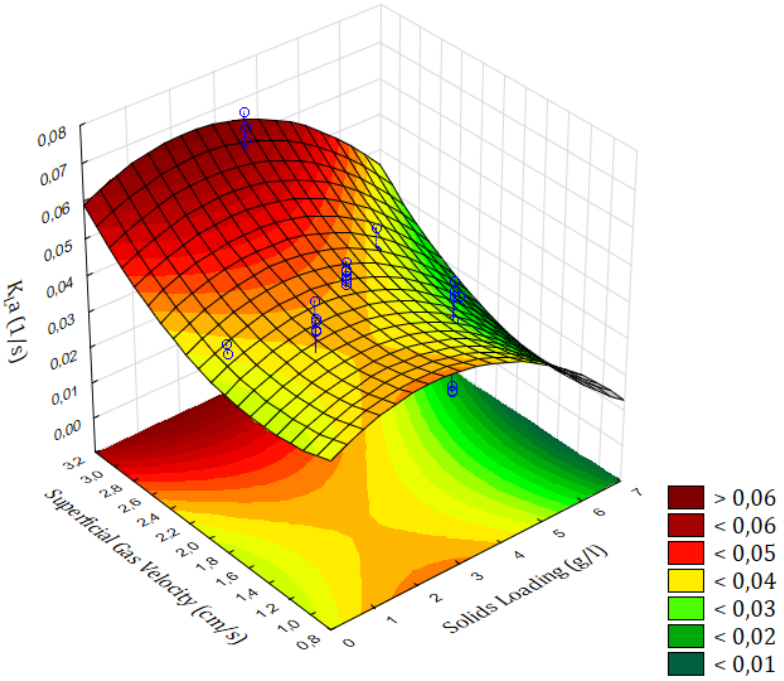

Figure 4.25: Influence of superficial gas velocity and solid loading on K_La in corn flour at constant alkane concentration (midpoint at 11.25 vol%)

Based on the evaluation of results for model hydrocarbon bioprocess using inert solids, it was found that the interfacial area behaviour was dependent only on the u_G and an empirical correlation was developed to predict this behaviour with 78.8% accuracy in the experimental range.

This behaviour of interfacial area was used to define the behaviour underpinning the K_La behaviour in the system. It was found that with an increase in u_G, the K_La increased as a result of the increase in interfacial area as well as the increase in K_L at u_G above 1.2 cm/s.

Since interfacial area was not influenced by increases in solids loading, the behaviour of K_La with increase in solids loading was due to changes in K_L. As solids loadings were increased, an initial increase in K_La was observed as a likely

consequence of liquid-side film penetration. This was followed by a decrease in K_La as solids were increased above 2.5 g/l, likely due to diffusion blocking effects.

4.4 Evaluation of Interfacial Area Behaviour in a Model Hydrocarbon Bioprocess Containing Non-Viable Microbes

The oxygen transfer behaviour in bioprocess systems in a BCR is not well documented and is therefore not well understood. To provide a basis for understanding these systems, the interfacial area was measured for a model hydrocarbon bioprocess with non-viable yeast ($d_p = 5.059\mu m$). Non-viable yeast was selected as a method to simplify the system, by removing substrate utilisation and respiration from the system, but allows an accurate representation of the solid particles present in bioprocess systems.

The D_{32}, ϵ_G and interfacial area data obtained for yeast dispersions was compared to the results obtained with inert solids and facilitated discussion of the influence of solid properties on the behaviour underpinning oxygen transfer behaviour in hydrocarbon bioprocesses.

4.4.1 Dependence of Sauter Mean Diameter on System Parameters

The measured D_{32} data for yeast systems was calculated from projected bubble areas using Equation 3.5. This data was statistically analysed and the Pareto plot shown in Figure 4.26 was constructed with the 95% confidence level indicated.

In systems with non-viable yeast dispersions, all linear main effects (u_G, alkane concentration and solids loading) as well as the quadratic effect of solids loading had a significant influence on D_{32}. For yeast dispersions, no interaction effects influenced D_{32} significantly at the 95% confidence level.

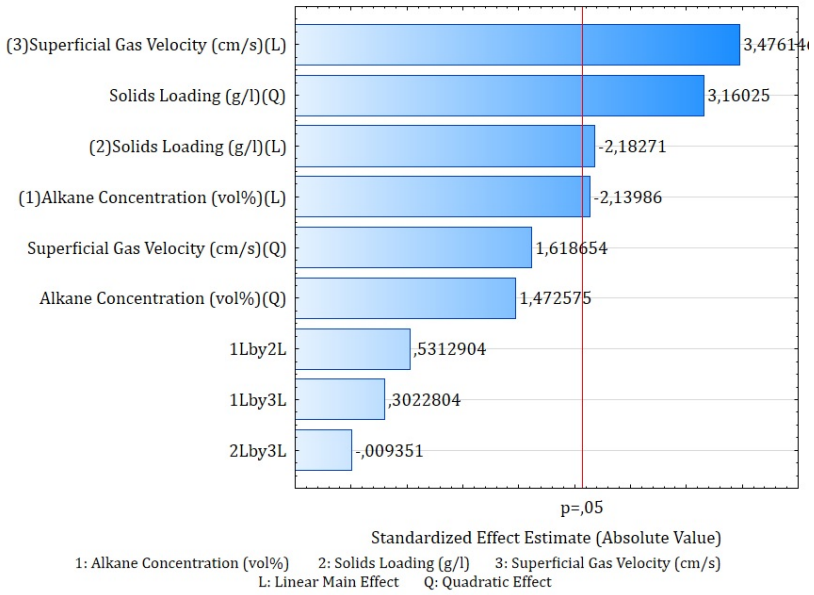

Figure 4.26: Pareto plot from basic statistical model defining the standardized effects on D_{32} in yeast with 95% confidence level indicated

4.4.1.1 Dependence of Sauter Mean Diameter on Alkane Concentration and Superficial Gas Velocity

The behaviour of D_{32} with alkane concentration and u_G at constant yeast loading is shown in Figure 4.27. Similar behaviour was observed at low and high constant yeast loadings and these surface plots are given in Appendix A.13.

Similarly to the behaviour of D_{32} with inert solids, shown in Figure 4.2, an increase in u_G resulted in an increase in the D_{32}. This behaviour was likely a result of changes in the bubble breakup and coalescence behaviour as well as an increase in the size of bubbles released from the sparger. A more detailed discussion of this behaviour is provided in Section 4.1.1.1.

The behaviour of yeast dispersions was different to that of inert solids with increases in alkane concentration. Figure 4.27 showed no influence of alkane concentration on D_{32} for all u_G, while systems with inert solids showed interaction between alkane concentration and u_G (Figure 4.2). This was a likely consequence of the surfactant introduced with the addition of yeast to the system. (Dietrich *et al.*, 1992) reported a decrease in the coalescence rate with the addition of surfactant molecules.

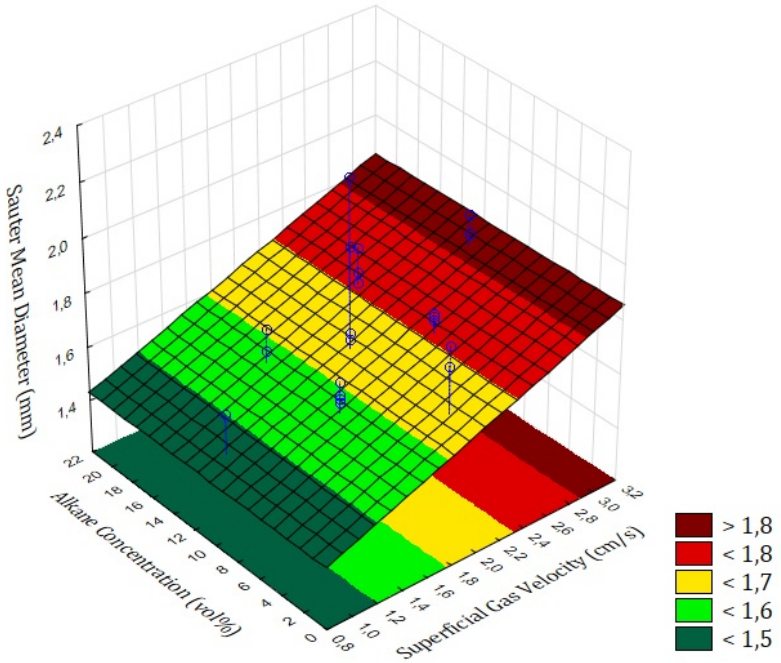

Figure 4.27: Influence of the superficial gas velocity and alkane concentration on D_{32} in yeast at constant solids loading (midpoint value of 3.25 g/l)

4.4.1.2 Dependence of Sauter Mean Diameter on Alkane Concentration and Solids Loading

The behaviour of D_{32} with alkane concentration and yeast loading at constant u_G is shwon in Figure 4.28. The behaviour of D_{32} with alkane concentration shows similar trend as that indicated in Figure 4.27. This was attributed to the presence of surfactant in the yeast suspension which decreases the rate of coalescence in the dispersion at consant yeast loading.

The trend observed with increasing solids loading shows an initial decrease. This decrease results from the adhesion of particles to the bubble surface, decreasing the coalescence behaviour, as well as the presence of surfactants in the yeast suspension. The presence of surfactant will decrease the D_{32} (Galindo *et al.*, 2005) through a decrease in the coalescence rate (Dietrich *et al.*, 1992). These effects increase the relative influence of bubble break up on the D_{32}. As the solids loading is further increased, the influence of surfactant and the behaviour of non-viable yeast cells as particles ceases as the relative viscosity of the dispersion is increased, limiting the bubble breakup behaviour in the column and increasing D_{32}.

The same behaviour with alkane concentration and u_G was observed at constant low and high yeast loading, shown in Appendix A.13.2.

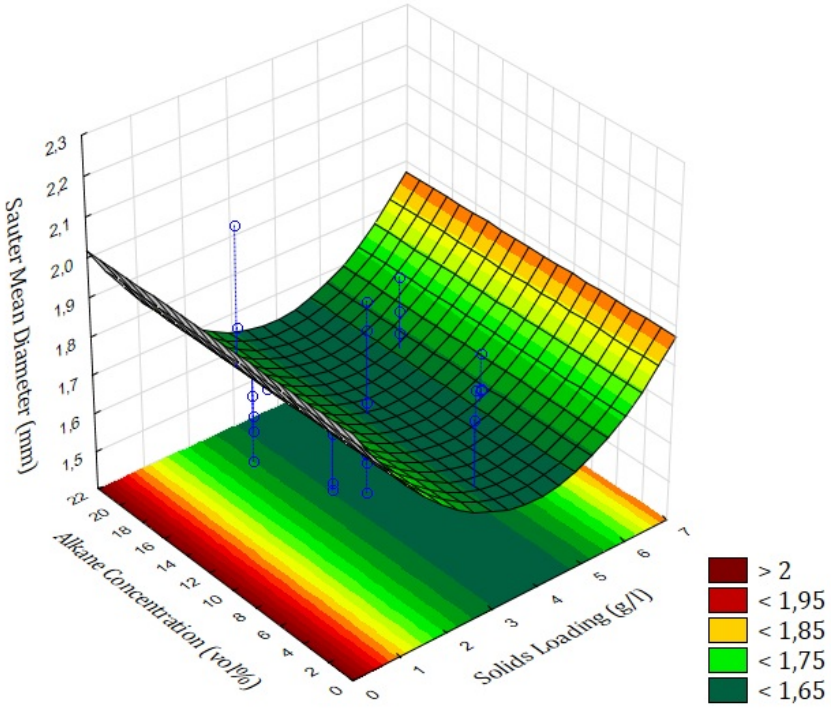

Figure 4.28: Influence of the alkane concentration and solids loading on D_{32} in yeast at constant superficial gas velocity (midpoint value of 2 cm/s)

4.4.1.3 Dependence of Sauter Mean Diameter on Superficial Gas Velocity and Solids Loading

The behaviour of D_{32} with u_G and yeast loading at constant alkane concentration is shown in Figure 4.29. Similar behaviour of D_{32} with increasing u_G was shown in Figure 4.27 and has been discussed in Section 4.4.1.1. The behaviour of D_{32} with increases in yeast loading was also indicated in Figure 4.28 and has been discussed in Section 4.4.1.2 where this was attributed to behaviour of the competing effects of surfactant and increase in apparent dispersion viscosity with fine particles.

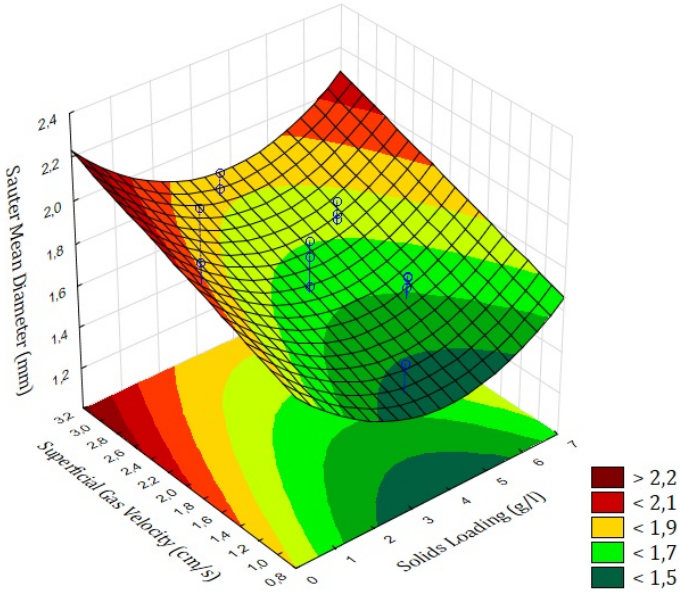

Figure 4.29: Influence of the superficial gas velocity and solids loading on D_{32} in yeast at constant alkane concentration (midpoint value of 11.25 vol%)

4.4.2 Dependence of Gas Holdup on System Parameters

The statistical analysis of the ϵ_G data for systems with non-viable yeast yielded the Pareto plot shown in Figure 4.30. Similarly to the data found with inert solids, the glsuG was the most significant to influence ϵ_G. However, in yeast dispersions, the interaction between alkane concentration and solids loading was also significant to influence the behaviour of ϵ_G

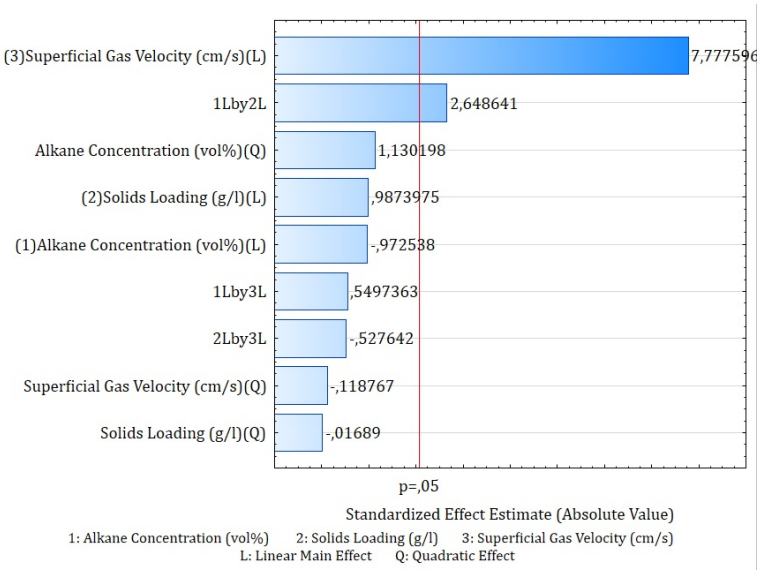

Figure 4.30: Pareto plot from basic statistical model defining the standardized effects on ϵ_G in yeast with 95% confidence level indicated

4.4.2.1 Dependence of Gas Holdup on Alkane Concentration and Superficial Gas Velocity

The influence of u_G and alkane concentration on the ϵ_G at constant solids loading is shown in Figure 4.31. This surface plot indicated that alkane concentration did not have an influence on the ϵ_G behaviour at any u_G. This corresponded well to findings with inert solids, shown in Figure 4.6.

The ϵ_G showed a linear increase with u_G at constant yeast loading. Similar behaviour was observed for inert solids, shown in Figure 4.2 and has been discussed in Section 4.1.2.1. Similar behaviour was observed at low and high solids loadings and these surface plots are provided in Appendix A.14.1.

However, the ϵ_G for yeast dispersions was lower than the ϵ_G found for inert solids with increasing u_G. Khare and Joshi (1990) found similar behaviour and reported that particles with a lower d_p resulted in a lower ϵ_G in isopropanol-aqueous dispersions with suspended alumina particles and glass beads (d_p of 12 - 1300 μm).

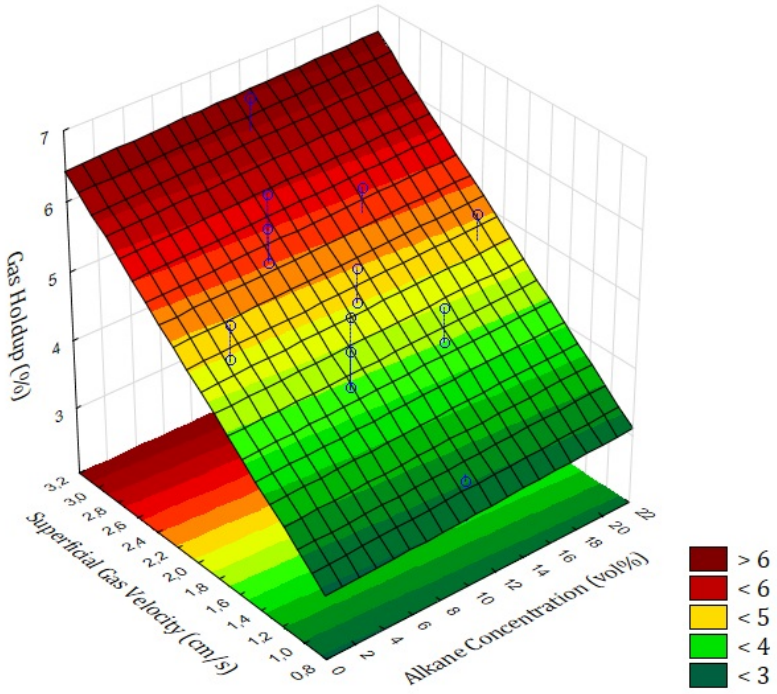

Figure 4.31: Influence of the superficial gas velocity and alkane concentration on ϵ_G in yeast at constant solids loading (midpoint value of 3.25 g/l)

4.4.2.2 Dependence of Gas Holdup on Superficial Gas Velocity and Solids Loading

The behaviour of ϵ_G with changes in u_G and yeast loading at constant alkane concentration is shown in Figure 4.32. This surface plot showed similar behaviour to systems with inert solids as u_G and yeast loading was varied, shown in Figure 4.7. As with inert solids, the solids loading did not have a statistically significant influence on ϵ_G behaviour. Similar trends for yeast dispersions were observed at low and high constant alkane concentration, shown in Appendix A.14.2.

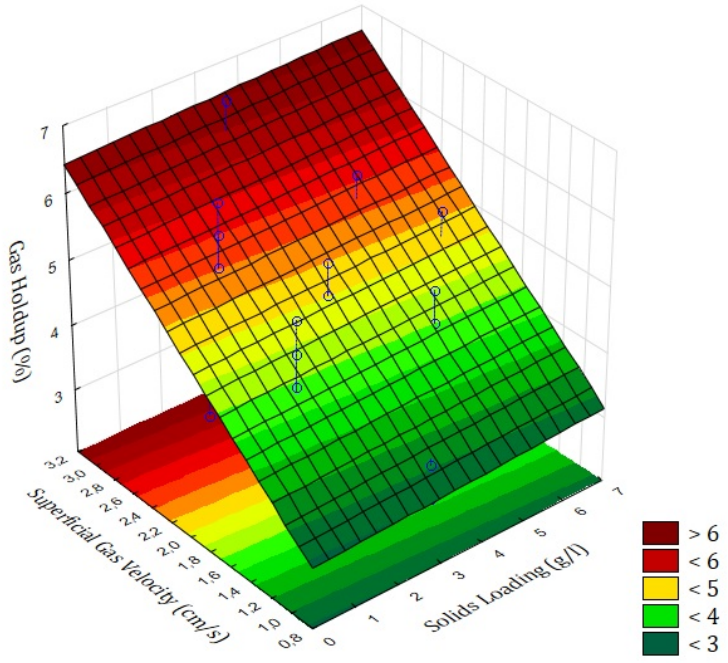

Figure 4.32: Influence of the superficial gas velocity and solids loading on ϵ_G in yeast at constant alkane concentration (midpoint value of 11.25 vol%)

4.4.2.3 Dependence of Gas Holdup on Alkane Concentration and Solids Loading

The behaviour of ϵ_G with alkane concentration and yeast loading at constant u_G is shown in Figure 4.33. This figure indicated an increase in the ϵ_G with increase in both alkane concentration and yeast loading. This behaviour was different to that found with inert solids (Figure 4.8) where these parameters did not influence ϵ_G. The increase observed in this figure corresponded to findings of Khare and Joshi (1990), where an increase in dispersion viscosity increased the ϵ_G across all solids loadings in isopropanol-aqueous dispersions with alumina solids. Similar behaviour was observed at low and high u_G, and these surface plots are provided in Appendix A.14.3.

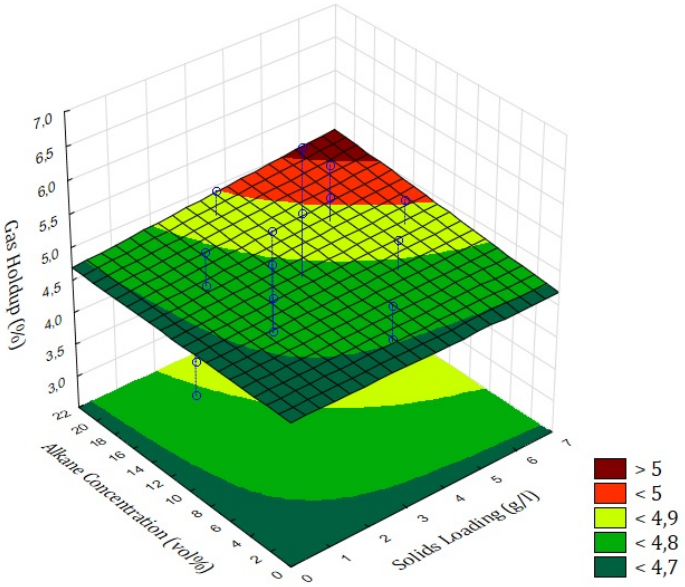

Figure 4.33: Influence of the alkane concentration and solids loading on ϵ_G in yeast at constant superficial gas velocity (midpoint value of 2 cm/s)

4.4.2.4 Prediction of the Gas Holdup Behaviour

Based on the linear behaviour of ϵ_G with u_G, an empirical correlation was developed to predict the ϵ_G behaviour in the experimental range. This empirical model was described by Equation 4.3. All experimental points were plotted in Figure 4.34 with the empirical model indicated. The model could account for 79.58% of all variance in ϵ_G.

$$\epsilon_G = 1.3762 u_G + 2.0337 \tag{4.3}$$

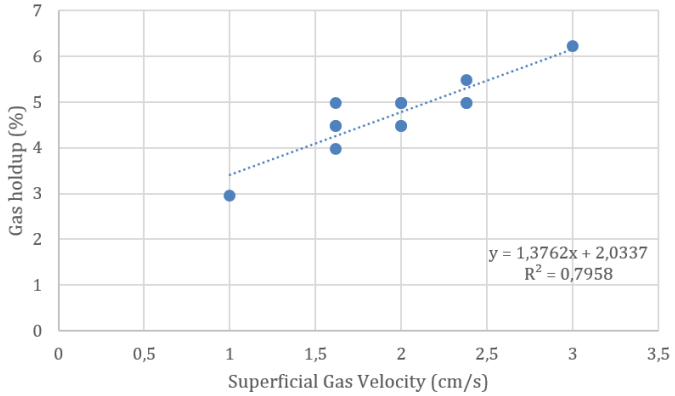

Figure 4.34: Experimental values indicating accuracy of the empirical model for prediction of gas holdup in systems containing yeast

4.4.3 Dependence of Interfacial Area on System Parameters

Statistical analysis of the data obtained for interfacial behaviour in yeast dispersions yielded the Pareto plot in Figure 4.35. A comparison of this Pareto plot with that obtained for inert solids (Figure 4.10) showed the same significant parameters for both systems.

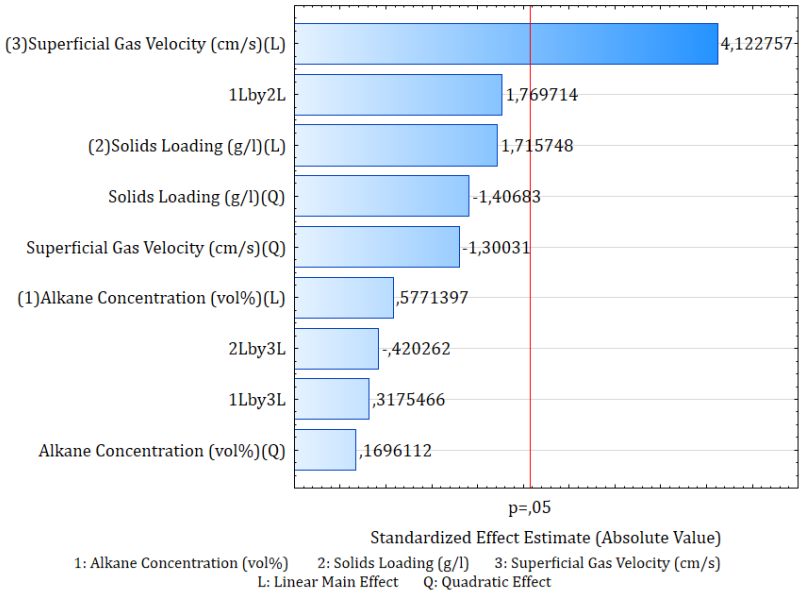

Figure 4.35: Pareto plot from basic statistical model defining the standardized effects on interfacial area in yeast with 95% confidence level indicated

4.4.3.1 Dependence of Interfacial Area on Alkane Concentration and Superficial Gas Velocity

The interfacial area behaviour with changes in alkane concentration and u_G at constant yeast loading is shown in Figure 4.36. Similarly to systems with inert solids, the interfacial area increased linearly with u_G and was not influenced by alkane concentration. These trends were discussed in Section 4.1.3.1. Similar behaviour was found at low and high yeast loading, provided in Appendix A.15.1.

However, the interfacial area obtained in systems containing yeast was lower than that of systems containing inert solids for all conditions. This was a result of the lower average ϵ_G, found in Section 4.4.2.1. This was likely a consequence of the lower d_p, which resulted in a lower ϵ_G.

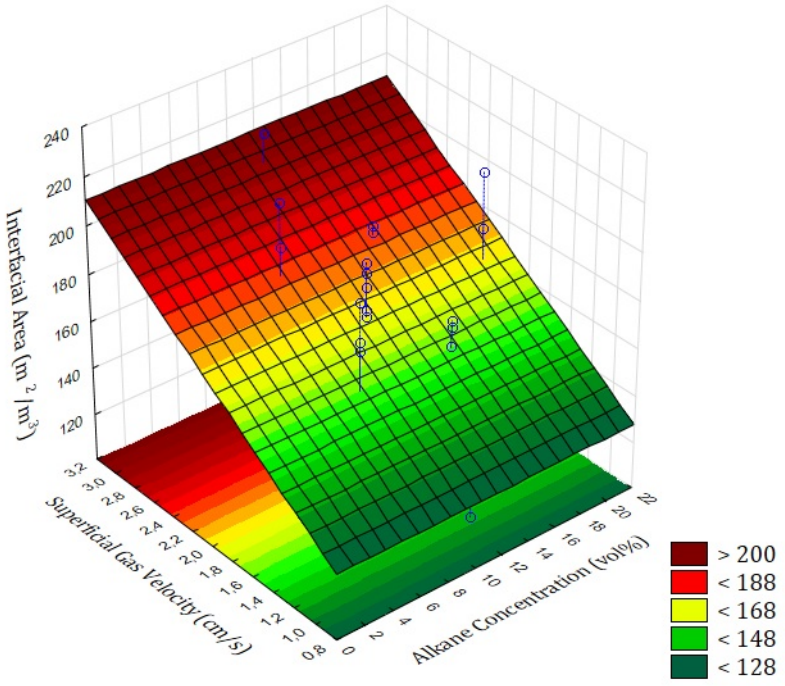

Figure 4.36: Influence of the superficial gas velocity and alkane concentration on interfacial area in yeast at constant solids loading (midpoint value of 3.25 g/l)

4.4.3.2 Dependence of Interfacial Area on Superficial Gas Velocity and Solids Loading

The influence of u_G and solids loading on interfacial area at constant alkane concentration is shown in Figure 4.37. This figure indicated a linear increase with increasing u_G, similar to that shown in Figure 4.36.

The yeast loading did not have an influence on the interfacial area at any u_G. Similar behaviour was found in systems with inert solids, shown in Figure 4.12. However, the interfacial area obtained with yeast was lower than that obtained with inert solids, and was discussed in Section 4.4.3.1. Similar behaviour was observed at low and high constant alkane concentration and are provided in Appendix A.15.2.

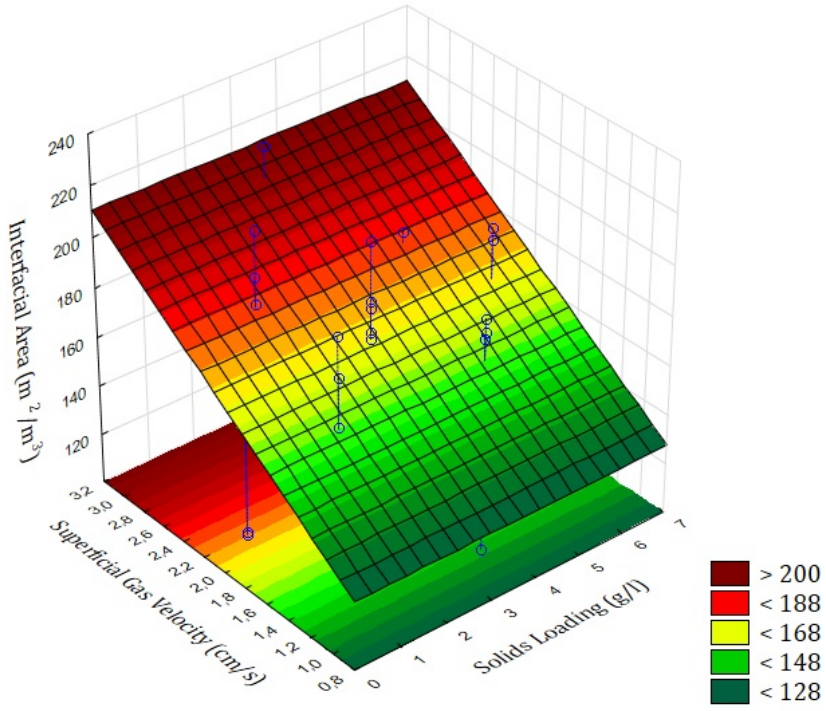

Figure 4.37: Influence of the superficial gas velocity and solids loading on interfacial area in non-viable yeast dispersions at constant alkane concentration (midpoint value of 11.25 vol%)

4.4.3.3 Dependence of Interfacial Area on Alkane Concentration and Solids Loading

The interfacial area behaviour with alkane concentration and yeast loading at constant u_G is shown in Figure 4.38. This surface plot confirmed the findings shown in Figure 4.36 and Figure 4.37, which indicated negligible influence of alkane concentration and yeast loading on interfacial area. At 3.25 g/l yeast loading and 11.25 vol% alkane concentration, the interfacial area remained constant at 169 m^2/m^3 for all u_G.

Similar behaviour was observed at low u_G (1.62 cm/s) where interfacial area had a constant value of 156 m^2/m^3 and at high u_G (2.38 cm/s), where interfacial area was constant at 182 m^2/m^3. These surface plots are shown in Appendix A.15.3.

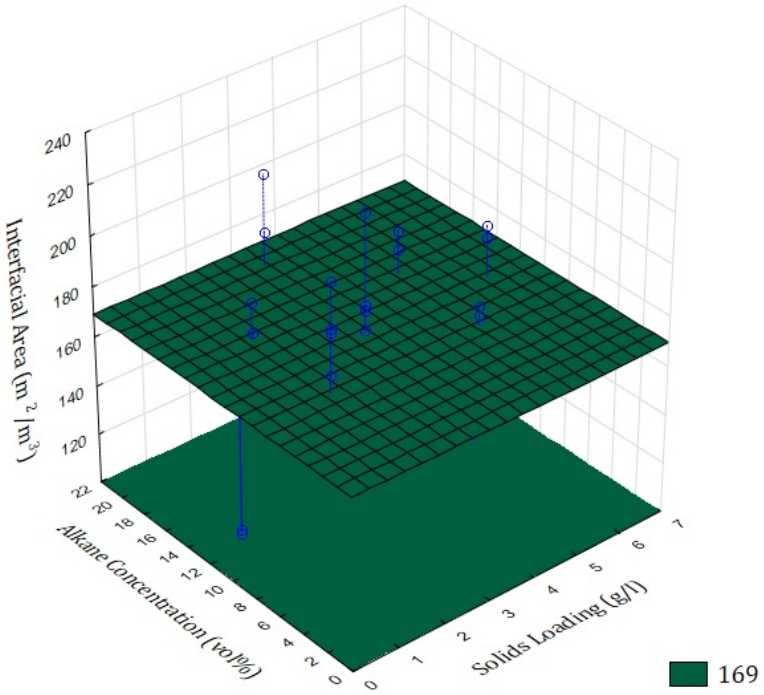

Figure 4.38: Influence of the alkane concentration and solids loading on interfacial area in yeast at constant superficial gas velocity (midpoint value of 2 cm/s)

4.4.3.4 Prediction of Interfacial Area

Statistical evaluation of the interfacial area behaviour with yeast solids showed a linear relationship between interfacial area and u_G. To qualify this relationship, an empirical model was constructed to predict interfacial area in the experimental range. This model is defined by Equation 4.4 and has an accuracy of 85.1%, shown in Figure 4.39. The correlation is valid for alkane concentrations between 7.88 ad 14.62 vol% and yeast loadings between 1.62 and 4.88 g/l across the full experimental range of u_G.

$$Area = 35.252u_G + 95.807 \tag{4.4}$$

Based on the trends observed for interfacial area, a linear relationship exists between the interfacial area and u_G. A plot of the relationship between interfacial area and u_G at midpoint solids loading (3.25 g/l) and midpoint alkane concentration (11.25 vol%) indicates a linear relationship which correlates well to the experimental data. This can be seen in Figure 4.39 which shows a 0.9598 R^2 value. This relationship should be extended and further investigated to ascertain the validity in a wider range of experimental values.

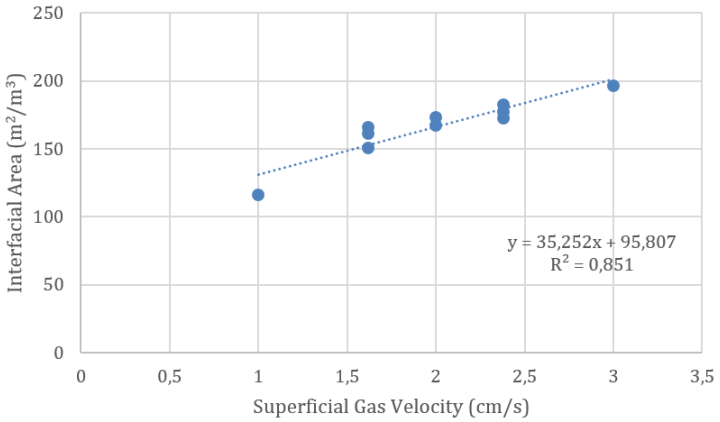

Figure 4.39: Influence of superficial gas velocity on interfacial area in non-viable yeast dispersions at constant alkane concentration (midpoint at 11.25 vol%) and constant solid loading (midpoint at 3.25 g/l)

Chapter 5

Conclusions

This study provides a fundamental understanding of the parameters which underpin oxygen transfer in alkane-aqueous dispersions with suspended solids in a BCR configuration under discrete hydrodynamic conditions. From this information, current knowledge of oxygen transfer prediction can be extended to hydrocarbon-based bioprocesses in column bioreactors.

A model hydrocarbon bioprocess was developed to investigate the behaviour of oxygen transfer in a BCR. The influence of u_G, alkane concentration and solids loading on interfacial area was investigated and used to provide a better understanding of the K_La in a system with inert solids.

In systems with inert solids, D_{32} increased with increasing u_G due to the increase in bubble size formed at the sparger. At higher u_G, the rate of bubble breakup was higher and D_{32} decreased. An increase in the alkane concentration also influenced D_{32} in this system. At low u_G, an increase in alkane concentration resulted in an increase in u_G due to increased dispersion viscosity. At higher u_G, alkane beads caused attrition and increased the rate of bubble breakup, decreasing D_{32}. The ϵ_G was only significantly influenced by u_G in the range of conditions considered. An empirical correlation was developed to predict this ϵ_G behaviour and 83.3% of the variance could be accounted for by u_G.

The interfacial area for corn flour systems was determined from the D_{32} and ϵ_G data. The data analysis showed a linear relationship between interfacial area and u_G, similar to that found for ϵ_G. The increase in interfacial area with u_G confirmed the hypothesised behaviour. An empirical correlation was established for the prediction of interfacial area in systems with inert solids and showed a 78.8% correlation to experimental data in the experimental range evaluated.

Correct determination of K_La was ensured by measurement of K_P. It was shown and can be concluded that the K_P value varied significantly with system parameters and must be measured at all experimental conditions.

K_La increased with u_G as the result of increasing interfacial area and increasing K_L with increases in liquid-film penetration. An increase in solids loading indicated an initial increase, followed by a decrease in K_La due to the influence of liquid-film penetration on K_L at low solids loading and diffusion blocking effects which decreased K_L at solids loading greater than 2.5 g/l.

To consolidate the interfacial area behaviour in a model hydrocarbon bioprocess, measurements were repeated with non-viable yeast and compared to data

obtained with inert solids. With the use of yeast, a small concentration of surfactant was introduced to the system and influenced the coalescence behaviour in the system.

The presence of surfactant molecules in the media inhibited coalescence with yeast loading up to about 3.5 g/l, and resulted in a decrease in D_{32}. Above this yeast loading, the fine yeast particles increased the viscosity sufficiently to overcome the influence of surfactant and increase the D_{32}.

The behaviour of ϵ_G in yeast dispersions was similar to that found with inert solids and demonstrated a linear increase with increased u_G. However, in yeast dispersions, an interaction between alkane concentration and yeast loading was significant to cause a slight increase in dispersion viscosity and increase ϵ_G with increased alkane concentration and yeast loading. Despite this interaction, an empirical correlation to predict the ϵ_G behaviour with increased u_G could still be developed to account for 72.5% of the variance in ϵ_G. Comparison of the yeast and inert solids dispersions indicated a 37.5% lower ϵ_G in yeast dispersions compared to inert solids as a result of the apparent viscosity introduced by finer solid particles. This ϵ_G and D_{32} data resulted in a linear increase in interfacial area with u_G with no significant influence of alkane concentration and yeast loading. This interfacial area was on average 6.7% lower than interfacial area found in inert solid dispersions as a likely consequence of the apparent viscosity with finer particles.

Chapter 6

Recommendations

This investigation provides the basis for further understanding of hydrocarbon bioprocesses in a BCR. The range of conditions investigated here must be expanded to include a wider range of system parameters for the prediction of oxygen transfer behaviour.

The influence of surfactant molecules in yeast dispersions highlighted potential differences between the model hydrocarbon bioprocess and the behaviour of an active hydrocarbon bioprocess. To properly understand the behaviour of an inactive hydrocarbon system, the oxygen transfer must be investigated with the presence of nutrients and other components found in bioprocesses. Once this behaviour is understood and quantified, consideration can be given to the investigation of an active system with measurement of oxygen and substrate utilisation.

To ensure that all aspects of a hydrocarbon bioprocess BCR are fully understood, a comparative study would also be conducted using different BCR configurations. This should include an investigation of the influence of different alkane composition and solids types, as well as different reactor configurations. Comparison of different sparger types in a BCR as well as a more comprehensive comparison between STR and BCR configurations will provide valuable insight for the selection of reactor configurations for specific applications.

The results also indicated important behaviour of K_P with changes in system parameters. The investigation of these influences was outside the scope of this investigation, but should be further investigated to establish the factors influencing K_P behaviour. A complete understanding of these influences will allow for more accurate determination of K_La in the study of oxygen transfer.

References

S. Aiba and S.Y. Huang. Oxygen Permeability and Diffusivity in Polymer Membranes Immersed in Liquids. *Chemical Engineering Science*, 24(7):1149–1159, July 1969.

K Akita and F Yoshida. Bubble Size, Interfacial Area, and Liquid-phase Mass Transfer Coefficient in Bubble Columns. *Industrial & Engineering Chemistry Process Design and Development*, 1974.

P.F.F. Amaral, M.G. Freire, M.H.M. Rocha-lea, and I.M. Marrucho. Optimization of Oxygen Mass Transfer in a Multiphase Bioreactor With Perfluorodecalin as a Second Liquid Phase. *Biotechnology and bioengineering*, 99(3):588–598, 2008.

ASTM International. ASTM E1951 - Standard Guide for Calibrating Reticles and Light Microscope Magnifications, 2007.

M. Bailey, C.O. Gomez, and J.A. Finch. Development and Application of an Image Analysis Method for Wide Bubble Size Distributions. *Minerals Engineering*, 18(12):1214–1221, October 2005.

M. Barigou and M. Greaves. Bubble-size distributions in a mechanically agitated gasliquid contactor. *Chemical Engineering Science*, 47(8):2009–2025, 1992.

T.M. Bartos and C.N. Satterfield. Effects of Finely Divided Solids on Mass Transfer Between a Gas and an Organic Liquid. *AIChE journal*, 32(5):773–781, 1986.

A. Behkish, Z. Men, J.R. Inga, and B.I. Morsi. Mass Transfer Characteristics in a Large-scale Slurry Bubble Column Reactor with Organic Liquid Mixtures. *Chemical Engineering Science*, 57(16):3307–3324, August 2002.

A.A. Benedek and W.J. Heideger. Polarographic Oxygen Analyzer Response: The Effect of Instrument Lag in the Non-steady State Reaeration Test. *Water Research*, 4:627–640, 1970.

M. Bouaifi, G. Hebrard, D. Bastoul, and M. Roustan. A Comparative Study of Gas Holdup, Bubble Size, Interfacial Area and Mass Transfer Coefficients in Stirred Gasliquid Reactors and Bubble Columns. *Chemical Engineering and Processing: Process Intensification*, 40(2):97–111, February 2001.

E. Camarasa, C. Vial, S. Poncin, and G. Wild. Influence of Coalescence Behaviour of the Liquid and of Gas Sparging on Hydrodynamics and Bubble Characteristics in a Bubble Column. *Chemical Engineering and Processing*, 38:329–344, 1999.

D. Cascaval, A.I. Galaction, E. Folescu, and M. Turnea. Comparative Study on the Effects of n-Dodecane Addition on Oxygen Transfer in Stirred Bioreactors for Simulated, Bacterial and Yeasts Broths. *Biochemical Engineering Journal*, 31(1):56–66, August 2006.

M.Y. Chisti and M. Moo-Young. Hydrodynamics and Oxygen Transfer in Pneumatic Bioreactor Devices. *Biotechnology and bioengineering*, 31:487–494, 1988.

K.G. Clarke and L.D.C. Correia. Oxygen Transfer in Hydrocarbonaqueous Dispersions and its Applicability to Alkane Bioprocesses: A Review. *Biochemical Engineering Journal*, 39(3):405–429, May 2008.

K.G. Clarke and M.M. Manyuchi. Methodology For Advanced Measurement Accuracy of the Overall Volumetric Oxygen Transfer Coefficient with Application to Hydrocarbon-aqueous Dispersions. *Journal of Chemical Technology & Biotechnology*, 87(11):1615–1618, November 2012.

K.G. Clarke, P.C. Williams, M.S. Smit, and S.T.L. Harrison. Enhancement and Repression of the Volumetric Oxygen Transfer Coefficient Through Hydrocarbon Addition and its Influence on Oxygen Transfer Rate in Stirred Tank Bioreactors. *Biochemical Engineering Journal*, 28(3):237–242, March 2006.

Cole-Parmer. Rotameters, 2013. URL `http://www.coleparmer.com/TechLibraryArticle/813`.

D. Colella, D. Vinci, R. Bagatin, M. Masi, and E.A. Bakr. A Study on Coalescence and Breakage Mechanisms in Three Different Bubble Columns. *Chemical Engineering Scien*, 54:4767–4777, 1999.

C.M. Cooper, G.A. Fernstrom, and S.A. Miller. Performance of Agitated Gas-liquid Contactors. *Industrial & Engineering Chemistry*, 36(6):504–509, 1944.

L.D.C. Correia. Oxygen Transfer in Hydrocarbon-aqueous Dispersions and its Applicability to Alkane-based Bioprocesses. *http://hdl.handle.net/10019.1/2942*, (December), 2007.

L.D.C. Correia and K.G. Clarke. Measurement of the Overall Volumetric Oxygen Transfer Coefficient in Alkane-aqueous Dispersions. *Journal of Chemical Technology & Biotechnology*, 84(12):1793–1797, December 2009.

L.D.C. Correia, C. Aldrich, and K.G. Clarke. Interfacial Gas-liquid Transfer Area in Alkane-aqueous Dispersions and its Impact on the Overall Volumetric Oxygen Transfer Coefficient. *Biochemical Engineering Journal*, 49(1):133–137, March 2010.

A. Crolla and K.J. Kennedy. Optimization of Citric Acid Production From Candida lipolytica Y- 1095 Using n-Paraffin. *Journal of biotechnology*, 89: 27–40, 2001.

T.R. Das, A. Bandopadhyay, R. Parthasarathy, and R. Kumar. Gas-liquid Interfacial Area in Stirred Vessels: The Effect of an Immiscible Liquid Phase. *Chemical Engineering Science*, 40(2):209–214, January 1985.

W.D. Deckwer and Y. Louisi. Hydrodynamic properties of the Fischer-Tropsch slurry process. *Industrial Engineering Chemical Process Design Development*, 19(4):699–708, 1980.

E. Dietrich, C. Mathieu, H. Delmas, and J. Jenck. Raney-Nickel Catalyzed Hydrogenations: Gas-liquid Mass Transfer in Gas-induced Stirred Slurry Reactors. *Chemical engineering science*, 47(13/14):3597–3604, 1992.

P.M. Doran. *Bioprocess Engineering Principles*, volume 9 of *Pure and applied mathematics (Academic Press) ; 125-126*. Academic Press, 1995. ISBN 0122208552.

E. Dumont and H. Delmas. Mass Transfer Enhancement of Gas Absorption in Oil-in-water Systems: A Review. *Chemical Engineering and Processing: Process Intensification*, 42(6):419–438, June 2003.

E. Dumont, Y. Andrès, and P. Le Cloirec. Effect of Organic Solvents on Oxygen Mass Transfer in Multiphase Systems: Application to Bioreactors in Environmental Protection. *Biochemical Engineering Journal*, 30(3):245–252, June 2006.

P. Fickers, P. Benetti, Y. Waché, A. Marty, S. Mauersberger, M.S. Smit, and J. Nicaud. Hydrophobic Substrate Utilisation by the Yeast Yarrowia lipolytica, and its Potential Applications. *FEMS yeast research*, 5(6-7):527–43, April 2005.

C. Freitas and J.A. Teixeira. Oxygen Mass Transfer in a High Solids Loading Three-phase Internal-loop Airlift Reactor. *Chemical Engineering Journal*, 84 (1):57–61, September 2001.

R. Fuchs, D.D.Y. Ryu, and A.E. Humphrey. Effect of Surface Aeration on Scale-Up Procedures for Fermentation Processes. *Industrial & Engineering Chemistry Process Design and Development*, 10(2):190–196, April 1971.

S. Fukui and A. Tanaka. *Production of useful compounds from alkane media in Japan*. 1980.

A-I. Galaction, D. Cascaval, C. Oniscu, and M. Turnea. Prediction of Oxygen Mass Transfer Coefficients in Stirred Bioreactors for Bacteria, Yeasts and Fungus Broths. *Biochemical Engineering Journal*, 20(1):85–94, August 2004.

A.I. Galaction, E. Folescu, and D. Cascaval. The Effect of n-Dodecane Addition on Oxygen Transfer in Stirred Bioreactors for Saccharomyces cerevisiae Broths. *Chemical Industry and Chemical Engineering Quarterly*, 11(1):1–9, 2005.

E. Galindo, A.W. Pacek, and A.W. Nienow. Study of Drop and Bubble Sizes in a Simulated Mycelial Fermentation Broth of Up to Four Phases. *Biotechnology and bioengineering*, 69(2):213–21, July 2000.

E. Galindo, C.P. Larralde-Corona, Teresa Brito, M.S. Córdova-Aguilar, B. Taboada, L. Vega-Alvarado, and G. Corkidi. Development of Advanced Image Analysis Techniques for the In Situ Characterization of Multiphase Dispersions Occurring in Bioreactors. *Journal of biotechnology*, 116(3):261–70, March 2005.

F. Garcia-Ochoa and E. Gomez. Bioreactor Scale-up and Oxygen Transfer Rate in Microbial Processes: An Overview. *Biotechnology advances*, 27(2):153–76, 2009.

C.L. Hyndman, F. Larachi, and C. Guy. Understanding Gas-phase Hydrodynamics in Bubble Columns: A Convective Model Based on Kinetic Theory. *Chemical engineering science*, 52(1), 1997.

Y. Imai, H. Takei, and M. Matsumura. A simple Na2SO3 Feeding Method for KLa Measurement in Large-scale Fermentors. *Biotechnology and Bioengineering*, 29(8):982–993, 987.

J.R. Inga and B.I. Morsi. Effect of Operating Variables on the Gas Holdup in a Large-Scale Slurry Bubble Column Reactor Operating with an Organic Liquid Mixture. *Industrial & Engineering Chemistry Research*, 38(3):928–937, March 1999.

M. Jamialahmadi and H. Muller-Steinhagen. Effect of Solid Particles on Gas Holdup in Bubble Columns. *The Canadian Journal of Chemical Engineering*, 69:390–393, 1991.

S. Jia, M. Wang, P. Kahar, Y. Park, and M. Okabe. Enhancement of Yeast Fermentation by Addition of Oxygen Vectors in Air-Lift Bioreactor. *Journal of Fermentation and Bioengineering1*, 84(2):176–178, 1997.

W. Jianlong. Enhancement of Citric Acid Production By Aspergillus niger Using n-Dodecane as an Oxygen-vector. *Process Biochemistry*, 35(10):1079–1083, July 2000.

G.E.H. Joosten, J.G.M. Schilder, and J.J. Janssen. The Influence of Suspended Solid Material on the Gas-liquid Mass Transfer in Stirred Gas-Liquid Contactors. *Chemical Engineering Science*, 32:563–566, 1977.

L-K. Ju and A. Sundararajan. The Effects of Cells on Oxygen Transfer in Bioreactors: Physical Presence of Cells as Solid Particles. *The Chemical Engineering Journal and the Biochemical Engineering Journal*, 56(1):B15–B21, December 1994.

B. Junker. Measurement of Bubble and Pellet Size Distributions: Past and Current Image Analysis Technology. *Bioprocess and biosystems engineering*, 29(3):185–206, August 2006.

N. Kantarci, F. Borak, and K.O. Ulgen. Bubble Column Reactors. *Process Biochemistry*, 40(7):2263–2283, June 2005.

Y. Kawase and M. Moo-Young. The effect of Antifoam Agents on Mass Transfer in Bioreactors. *Bioprocess Engineering*, 5:169–173, 1990.

A.S. Khare and J.B. Joshi. Effect of Fine Particles on Gas Hold-up in Three-phase Sparged Reactors. *The Chemical Engineering Journal*, 44(1):11–25, June 1990.

S.L. Kiambi and A.M. Duquenne. Measurements of Local Interfacial Area: Application of Bi-optical Fibre Technique. *Chemical Engineering Science*, 56: 6447–6453, 2001.

M.A. Kohler. Comparison of Mechanically Agitated and Bubble Column Slurry Reactors. *Applied catalysis*, 22:21–53, 1986.

M. Laakkonen, M. Honkanen, P. Saarenrinne, and J. Aittamaa. Local Bubble Size Distributions, Gasliquid Interfacial Areas and Gas Holdups in a Stirred Vessel With Particle Image Velocimetry. *Chemical Engineering Journal*, 109 (1-3):37–47, May 2005.

V. Linek and V. Vacek. Chemical Engineering Use of Catalyzed Sulfite Oxidation Kinetics for the Determination of Mass Transfer Characteristics of Gas-liquid Contactors. *Chemical Engineering Science*, 36(11):1747–1768, 1981.

V. Linek, P. Benes, and V. Vacek. Dynamic Pressure Method for KLa Measurement in Large-scale Bioreactors. *Biotechnology and Bioengineering*, 33(11): 1406–1412, 1989.

V. Linek, P. Benes, J. Sinkule, and T. Moucha. Non-ideal Pressure Step Method for KLa Measurement. *Chemical Engineering Science1*, 48(9):1593–1599, 1993.

J.V. Littlejohns and A.J. Daugulis. Oxygen Transfer in a Gasliquid System Containing Solids of Varying Oxygen Affinity. *Chemical Engineering Journal*, 129:67–74, May 2007.

R. Maceiras, E. Álvarez, and M.A. Cancela. Experimental Interfacial Area Measurements in a Bubble Column. *Chemical Engineering Journal*, 163(3):331–336, October 2010.

P.M.P.N.C. Mena. *Mass transfer and hydrodynamics in multiphase systems*. PhD thesis, University of Porto, Portugal, 2005.

J.C. Merchuk and M. Gluz. The Encyclopedia of Bioprocess Technology: Fermentation, Biocatalysis and Bioseparation. *Encyclopedia of Bioprocess Technology: Fermentation, Biocatalysis and Bioseparation*, 1:320–394, 1999.

D.B. Mills, R. Bar, and D.J. Kirwan. Effect of Solids on Oxygen Transfer in Agitated Three-phase Systems. *AIChE journal*, 33(9):1542–1549, 1987.

A. Morao, C.I. Maia, M.M.R. Fonesca, J.M.T. Vasconcelos, and S.S. Alves. Effect of Antifoam Addition on Gas-liquid Mass Transfer in Stirred Fermenters. *Bioprocess Engineering*, 20:165–172, 1999.

A.A. Mouza, G.K. Dalakoglou, and S.V. Paras. Effect of Liquid Properties on the Performance of Bubble Column Reactors with Fine Pore Spargers. *Chemical Engineering Science*, 60(5):1465–1475, March 2005.

M. Nakanoh and F. Yoshida. Gas Absorption by Newtonian and non-Newtonian Liquids in a Bubble Column. *Industrial Engineering Chemical Process Design Development*, 19:190–195, 1980.

K. Nguyen-tien, A.N. Patwari, A. Schumpe, and W.D. Deckwer. Gas-liquid Mass Transfer in Fluidized Particle Beds. *AIChE Journal*, 31:194–201, 1985.

C. Nicolella, M.C. van Loosdrecht, R.G. van der Lans, and J.J. Heijnen. Hydrodynamic Characteristics and Gas-liquid Mass Transfer in a Biofilm Airlift Suspension Reactor. *Biotechnology and bioengineering*, 60(5):627–35, December 1998.

D.R. Nielsen, A.J. Daugulis, and P.J. McLellan. A Novel Method of Simulating Oxygen Mass Transfer in Two-Phase Partitioning Bioreactors. *Biotechnology and Bioengineering*, 83(6):735–742, September 2003.

H. Oguz, A. Brehm, and W.D. Deckwer. Gas/ Liquid Mass Transfer In Sparged Agitated Slurries. *Chemical Engineering Science*, 42(7):1815–1822, 1987.

B. Özbek and S. Gayik. The Studies on the Oxygen Mass Transfer Coefficient in a Bioreactor. *Process Biochemistry*, 36(8-9):729–741, March 2001.

O. Ozkan, A. Calimli, R. Berber, and H. Oguz. Effect of Inert Solid Particles at Low Concentrations on Gasliquid Mass Transfer in Mechanically Agitated Reactors. *Chemical Engineering Science*, 55:2737–2740, 2000.

S.S. Öztürk and A. Schumpe. The Influence of Suspended Solids on Oxygen Transfer to Organic Liquids in a Bubble Column. *Chemical engineering science*, 42(7):1781–1785, 1987.

A.N. Patwari, K. Nguyen-tien, A. Schumpe, and W.D. Deckwer. Three-phase Fluidized Beds With Viscous Liquid: Hydrodynamics and Mass Transfer. *Chemical Engineering Communication*, 40:49–65, 1985.

T.L. Philici and M.K. Stenstrom. Effects of Dissolved Oxygen Probe Lag on Oxygen Transfer Parameter Estimation. *Journal (Water Pollution Control Federation)*, 61:83–86, 1989.

A. Prakash, A. Margaritis, H. Li, and M.A. Bergougnou. Hydrodynamics and Local Heat Transfer Measurements in a Bubble Column with Suspension of Yeast. *Biochemical Engineering Journal*, 9(2):155–163, December 2001.

G. Quicker, A. Schumpe, and W.D. Deckwer. Gas-liquid Interfacial Areas in a Bubble Column with Suspended Solids. *Chemical Engineering Science*, 39(1): 183–185, 1984.

G. Quijano, M. Hernandez, S. Villaverde, F. Thalasso, and R. Muñoz. A Step-forward in the Characterization and Potential Applications of Solid and Liquid Oxygen Transfer Vectors. *Applied microbiology and biotechnology*, 85(3):543–51, January 2010a.

G. Quijano, J. Rocha-Ríos, M. Hernández, S. Villaverde, S. Revah, R. Muñoz, and F. Thalasso. Determining the Effect of Solid and Liquid Vectors on the Gaseous Interfacial Area and Oxygen Transfer Rates in Two-phase Partitioning Bioreactors. *Journal of hazardous materials*, 175:1085–1089, March 2010b.

J.L. Rols and G. Goma. Enhancement of Oxygen Transfer Rates in Fermentation Using Oxygen-vectors. *Biotechnology advances*, 7:1–14, 1989.

J.L. Rols, J.S. Condoret, C. Fonade, and G. Goma. Mechanism of Enhanced Oxygen Transfer in Fermentation Using Emulsified Oxygen-vectors. *Biotechnology and bioengineering*, 35:427–435, 1990.

M.C. Ruzicka and J. Zahradnik. Homogeneous - Heterogeneous Regime Transition in Bubble Columns. *Chemical Engineering Science*, 56:4609–4626, 2001.

E. Sada and H. Kumazawa. Gas-liquid Mass Transfer Characteristics in a Bubble Column with Suspended Sparingly Soluble Fine Particles. *Industrial Engineering Chemical Process Design Development*, 24(2):255–261, 1985.

E. Sada, H. Kumazawa, and C.H. Lee. Influences of Suspended Fine Particles on Gas Holdup and Mass Transfer Characteristics in a Slurry Bubble Column. *AIChE Journal*, 32(5):853–856, 1986.

J.A. Sánchez Pérez, E.M. Rodríguez Porcel, J.L. Casas López, J.M. Fernández Sevilla, and Y. Chisti. Shear Rate in Stirred Tank and Bubble Column Bioreactors. *Chemical Engineering Journal*, 124:1–5, November 2006.

R. Schafer, C. Merten, and G. Eigenberger. Bubble Size Distributions in a Bubble Column Reactor Under Industrial Conditions. *Experimental Thermal and Fluid Science*, 26:595–604, 2002.

A. Schumpe and W.D. Deckwer. Viscous Media in Tower Bioreactors: Hydrodynamic Characteristics and Mass Transfer Properties. *Bioprocess Engineering*, 2:79–94, 1987.

B. Taboada, P. Larralde, T. Brito, L. Vega-Alvarado, R. Diaz, E. Galindo, and G. Corkidi. Images Acquisition of Multiphase Dispersions in Fermentation Processes. *Journal of Applied Science and Technology*, 1(1):78–84, 2003.

B. Taboada, L. Vega-Alvarado, M. S. Córdova-Aguilar, E. Galindo, and G. Corkidi. Semi-automatic Image Analysis Methodology for the Segmentation of Bubbles and Drops in Complex Dispersions Occurring in Bioreactors. *Experiments in Fluids*, 41(3):383–392, June 2006.

W.T. Tang and L.S. Fan. Gas-liquid Mass Transfer in a Three-phase Fluidized Bed Containing Low Density Particles. *Industrial & Engineering Chemistry Research*, 29(1):128–133, 1990.

The Mathworks Inc. Matlab Help File, 2012.

The Mathworks Inc. edge, 2014a.

The Mathworks Inc. imclearborder, 2014b.

The Mathworks Inc. bwboundaries, 2014c.

J.T. Trevors, R.L. Merrick, I. Russell, and G.G. Stewart. A Comparison of Methods for Assessing Yeast Viability. *Biotechnology Letters*, 5(2):131–134, 1983.

L.A. Tribe, C.L. Briens, and A. Margaritis. Determination of the Volumetric Mass Tansfer Coefficient (kLa) Using the Dynamic "Gas Out-Gas In" Method: Analysis of Errors Caused by Dissolved Oxygen Probes. *Biotechnology and Bioengineering*, 46:338–392, 1995.

C.O. Vandu, K. Koop, and R. Krishna. Volumetric Mass Transfer Coefficient in a Slurry Bubble Column Operating in the Heterogeneous Flow Regime. *Chemical Engineering Science*, 59(22-23):5417–5423, November 2004.

K. Van't Riet. Review of Measuring Methods and Results in Nonviscous Gas-Liquid Mass Transfer in Stirred Vessels. *Industrial & Engineering Chemistry Process Design and Development*, 18(3):357–364, July 1979.

L. Vega-Alvarado and M.S. Cordova. Online Sauter Diameter Measurement of Air Bubbles and Oil Drops in Stirred Bioreactors by Using Hough Transform. *Image Analysis and Recognition*, pages 834–840, 2004.

S.D. Vlaev and M. Fialova. Bubble Column Bioreactors: Comparison with Stirred Fermenters Based on Local Gas Hold-up Distribution. *The Canadian Journal of Chemical Engineering*, 81:535–542, 2003.

D.L. Vu, M. Sys, and L. Červenka. The Effect of Various Potentials on the Attachment of Saccharomyces Cerevisiae and Staphylococcus Epidermidis to Carbon Paste Electrodes. *International Journal of Electrochemical Science*, 6: 5265–5274, 2011.

A. Wentzel, T.E. Ellingsen, H. Kotlar, S.B. Zotchev, and M. Throne-Holst. Bacterial Metabolism of Long-chain n-Alkanes. *Applied microbiology and biotechnology*, 76(6):1209–21, October 2007.

P.M. Wilkinson, A. Van Schayk, J.P.M. Spronken, and L.L. Van Dierendonck. The Influence of Gas Density and Liquid Properties on Bubble Breakup. *Chemical Engineering Science*, 48(7):1213–1226, April 1993.

H. Yagi and F. Yoshida. Oxygen Absorption in Fermenters: Effects of Surfactants, Antifoaming Agents, and Sterilized Cells. *Journal of Fermentation Technology*, 52(12):905–916, 1974.

F. Yoshida, T. Yamane, and Y. Miyamoto. Oxygen Absorption into Oil-in-Water Emulsions. A Study on Hydrocarbon Fermentors. *Industrial & Engineering Chemistry Process Design and Development*, 9(4):570–577, October 1970.

J. Zahradnik and L. Drápal. Hydrodynamic and Mass Transfer Characteristics of Sectionalized Aerated Slurry Reactors. *Chemical Engineering and Processing*, 31:263–272, 1992.

D.G. Zill and M.R. Cullen. *Advanced Engineering Mathematics*. Jones and Bartlett, Sudbury, 3rd edition, 2005.

Appendix A

A.1 Analytical Derivation of Second Order Model for Oxygen Transfer

As stated previously, and repeated here for completeness, the first order model for oxygen transfer can be written as shown in Equation A.1.

$$\frac{dC}{dt} = K_L a(C^* - C) \tag{A.1}$$

And the probe response lag can be written using Equation A.2

$$\frac{dC_P}{dt} = K_P(C - C_P) \tag{A.2}$$

To combine these two models, we must define the dimensionless parameters, Y and Y_P, given in Equations A.3 and Equation A.4 respectively (Fuchs *et al.*, 1971)

$$Y = \frac{C^* - C}{C^* - C_0} \tag{A.3}$$

$$Y_P = \frac{C_P^* - C_P}{C_P - C_{P0}} \tag{A.4}$$

Substitution of Equation A.3 into Equation A.1 yields Equation A.5

$$\frac{dY}{dt} = -K_L a Y \tag{A.5}$$

Similarly, substitution of Equation A.4 into Equation A.4 yields Equation A.6

$$\frac{dY_P}{dt} = K_P(Y - Y_P) \tag{A.6}$$

Rearranging Equation A.5 and Equation A.6 gives Equation A.7 and Equation A.8,

$$\frac{dY}{Y} = -K_L a dt \tag{A.7}$$

$$\frac{dY_P}{dt} = K_P Y - K_P Y_P \tag{A.8}$$

Equation A.7 can then be integrated and rearranged to give Equation A.9

$$Y = I\mathrm{e}^{-K_L at} \tag{A.9}$$

Substitution of Equation A.9 into Equation A.8 yields Equation A.10

$$\frac{dY_P}{dt} = K_P I\mathrm{e}^{-K_L at} - K_P Y_P \tag{A.10}$$

Where Equation A.10 is a linear differential equation and can be solved through the method of separation and integration of variables. The solution for a linear differential equation is the sum of the homogeneous and non-homogeneous solutions (Zill and Cullen, 2005). The format of this solution is given in Equation A.11

$$Y' = Y_C + Y_P \tag{A.11}$$

The homogeneous differential equation (also the separable differential equation) is shown below in Equation A.12

$$\frac{dY_P}{dt} + K_P Y_P = 0 \tag{A.12}$$

Integration of Equation A.12 gives Equation A.13, where J is an integration constant.

$$Y_P = J\mathrm{e}^{-K_P t} \tag{A.13}$$

Expressing this in function form, Equation A.13 becomes Equation A.14

$$f = A'\mathrm{e}^{-B't} \tag{A.14}$$

With the complimentary form given in Equation A.15

$$Y_C = A'\mathrm{e}^{-B't} \tag{A.15}$$

Similarly, the complimentary form of Equation A.10 is given in Equation A.16

$$dY_C + K_P Y_C = K_P A'\mathrm{e}^{-B't} - A'B'\mathrm{e}^{-B't} \tag{A.16}$$

But it also follows directly from Equation A.10, that Equation A.17 holds,

$$dY_C + K_P Y_C = K_P I \mathrm{e}^{-K_L a t} \tag{A.17}$$

And, Equation A.16 and Equation A.17 are equivalent, yielding Equation A.18

$$(K_P A' - A'B')\mathrm{e}^{-B't} = K_P I \mathrm{e}^{-K_L a t} \tag{A.18}$$

Setting the base units and the exponents equal yields Equation A.19 and Equation A.20, respectively

$$K_P A' - A'B' = K_P I \tag{A.19}$$

$$B' = K_L a \tag{A.20}$$

Manipulation of Equation A.18 gives Equation A.21

$$A' = \frac{K_P I}{K_P - B'} \tag{A.21}$$

Substituting Equation A.20 into Equation A.21 gives the particular solution for the differential equation. This solution is given in Equation A.22

$$A' = \frac{K_P I}{K_P - K_L a} \tag{A.22}$$

Substitution of Equation A.13 and A.15 into the general solution (Equation A.11) gives Equation A.23

$$Y' = J\mathrm{e}^{-K_P t} + A'\mathrm{e}^{-B't} \tag{A.23}$$

And substitution of solutions for A' and B', given in Equation A.20 and Equation A.22 yields Equation A.24

$$Y'(K_P - K_L a) = (K_P - K_L a)J\mathrm{e}^{-K_P t} + K_P I \mathrm{e}^{-K_L a t} \tag{A.24}$$

Rearranging Equation A.24 yields Equation A.25,

$$Y' = \frac{1}{K_P - K_L a}\left[J(K_P - K_L a)\mathrm{e}^{-K_P t} + K_P I \mathrm{e}^{-K_L a t}\right] \tag{A.25}$$

Setting I = 1, allows for the determination of J, given in Equation A.26

$$J = \frac{-K_L a}{K_P - K_L a} \tag{A.26}$$

Substituting Equation A.26 into Equation A.25 yields Equation A.27

$$Y' = \frac{1}{K_P - K_L a}[-K_L a \mathrm{e}^{-K_P t} + K_P I \mathrm{e}^{-K_L a t}] \tag{A.27}$$

Since Y' is relationship for the DO with probe response included, the previously defined dimensionless quantity holds as a relationship for Y' as given in Equation A.28

$$Y' = \frac{C_P^* - C_P}{C_P^* - C_{P0}} \tag{A.28}$$

Substituting Equation A.28 into Equation A.27 and setting the initial concentration (at t=0) of the oxygen probe to zero (Fuchs *et al.*, 1971), yields the second order model for oxygen transfer as given in Equation A.29

$$\frac{C_P}{C_P^*} = 1 - \frac{1}{K_P - K_L a}[K_P \mathrm{e}^{-K_L a t} - K_L a \mathrm{e}^{-K_P t}] \tag{A.29}$$

A.2 Rotameter Calibration

The operational principle of a rotameter (or variable area flowmeter) is the balance of forces underneath the rotameter float with gravity. This is achieved by a uniformly tapered tube with a float of diameter almost equivalent to that of the tube at the inlet. Based on these forces a proportional relationship exists between the float height and the flow rate (Cole-Parmer, 2013).

For rotameters operating with gases, the compressibility of the gases are greatly influenced by operating pressure. Therefore, the rotameter must be calibrated to correct for pressure and temperature differences, as well as to correct for different gases. Since air was used in this study, no correction needs to be calculated for gas density and only the pressure and temperature need adjustment, according to Equation A.30.

$$q'_A = q^o_A \sqrt{\frac{P}{760} . \frac{530}{T}} \tag{A.30}$$

Where

q'_A is the corrected flow rate
q^o_A is the standard air flow rate
P is the absolute pressure at rotameter inlet in mmHg
T is the absolute temperature in $^\circ$ R

The working pressure, between the rotameter and column inlet, was measured for each rotameter scale reading. This working pressure was used to correct the rotameter calibration curve according to Equation A.30. Since the laboratory is air conditioned and maintained at a constant temperature of 21 °C, it was not necessary to adjust for temperature.

The data pertaining to the rotameter and float specifications as well as the standard calibration conditions are given in Table A.1. The flow rates at each scale reading, under standard metering conditions, are given in Table A.2.

The corrected calibration curve calculated using this data can be found in Figure A.1.

Table A.1: Rotameter Calibration Specifications

Maximum Flow Rate	45227	**Minimum Flow Rate**	2182
Units	std ml/min	**Metering Fluid**	air
Date	30 Nov 1999		

Tube Number	044-40-ST	**Metering Pressure**	14,70 psia
Float Material	316 Stainless Steel	**Metering Density**	0,001200 g/ml
Float Density	8,04 g/ml	**Metering Viscosity**	0,01812 cp
Standard Conditions	STP: 1atm @ 70° F	**Density at STP**	0,001200 g/ml
Room Temperature	70° F	**Accuracy**	Standard
Metering Temperature	70° F	**Barometric Pressure**	14,70 psia

Table A.2: Cole Parmer Flow Rates at Each Scale Reading

Scale Readings at Centre of Float	
Scale Reading [mm]	**Flow Rate [ml/min]**
150	45227
140	41968
130	38315
120	35172
110	31655
100	28245
90	25161
80	22199
70	19057
60	16007
50	12988
40	10040
30	7256
20	4668
10	2182

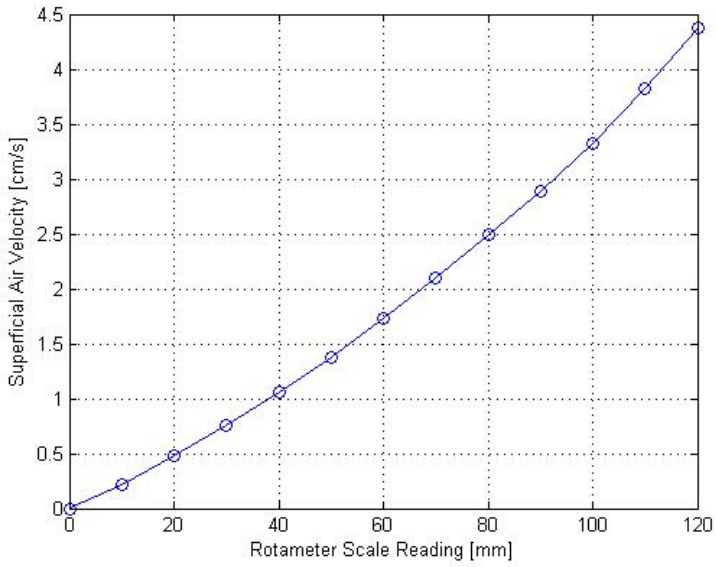

Figure A.1: Corrected superficial gas velocities for rotameter calibration

A.3 Stepwise Experimental Procedure

Before the start of each experiment, the following procedure was followed to ensure correct operation. For all experiments involving deactivated yeast, the yeast was deactivated according to the procedure described in Section 3.1.2.2 before beginning other experimental preparation.

Prior to the start of each experiment, the column was flushed with clean water to remove any residual solids and alkane in the column. Thereafter, the column was drained and all outlet valves were closed. The water level in the perspex box was checked to ensure that the area for image acquisition was completely submerged. Ice was added to the pump bath to circulate cold water to the condenser for removal of any alkane in the gas vent.

Once all initial checks had been conducted, the column contents were measured out and added to the column and the initial liquid height measured. Once the column lid was secured, the air inlet was opened and adjusted to 4cm/s superficial velocity to allow for initial mixing of the column contents. This initial mixing was carried out for a period of 5 minutes before adjusting the rotameter to the desired set point according to the calibration given in A.2 and allowed 2 minutes to reach steady state velocity.

During this initial mixing period, the electrolyte in the DO probe was replaced and the probe visually inspected for damage. The focal distance of the camera was also adjusted to 7.5cm, with the use of a grid to ensure the camera focus was within the visible range. The camera could then be positioned perpendicular to the column at a set distance, with a height of 30cm above the sparger.

Once steady state gas flow and bubble dynamics had been reached, the gas holdup was measured and images were obtained according to the image acquisition procedure outlined in Section 3.3.1. For each experimental run, 150 images were captured to ensure sufficient sample size, with more than 300 detected bubbles. Thereafter, the measurement of K_P and K_La were conducted in triplicate, according to the procedure described in Section 3.4.

Once all required measurements were taken, the column was drained and rinsed with clean water to ensure the removal of all solid and alkane residues. The valves were again closed, the pump switched off and the equipment safely stored.

A.4 MATLAB Code for Determination of K_La

```
clear, clc
dirname = 'C:\Users\Jannean\Desktop\Kla Data';
filename = ['<filename.xlsx>'];

%% Step 1: Read data for Kla and Kp
%Must read both the time intervals and the DO readings at
    correct matrix
%lengths
%%Kla data
time1a = xlsread(fullfile(dirname, filename), 'Rep1', 'H9
    :H49');
C1a    = xlsread(fullfile(dirname, filename), 'Rep1', 'I9
    :I49');
time1b = xlsread(fullfile(dirname, filename), 'Rep1', 'H9
    :H45');
C1b    = xlsread(fullfile(dirname, filename), 'Rep1', 'K9
    :K45');
time1c = xlsread(fullfile(dirname, filename), 'Rep1', 'H9
    :H44');
C1c    = xlsread(fullfile(dirname, filename), 'Rep1', 'M9
    :M44');

%% Kp data
time2a = xlsread(fullfile(dirname, filename), 'Rep1', 'A9
    :A21');
Cp1a   = xlsread(fullfile(dirname, filename), 'Rep1', 'B9
    :B21');
time2b = xlsread(fullfile(dirname, filename), 'Rep1', 'A9
    :A27');
Cp1b   = xlsread(fullfile(dirname, filename), 'Rep1', 'D9
    :D27');
time2c = xlsread(fullfile(dirname, filename), 'Rep1', 'A9
    :A21');
Cp1c   = xlsread(fullfile(dirname, filename), 'Rep1', 'F9
    :F21');

%% Step 2: Normalise data for C/C* and Cp/Cp*
% To scale all data to the correct range between 0 and
    100% DO

```

```
for j = 1:length(Cp1a)
    Cp1a_norm(j) = Cp1a(j)/Cp1a(length(Cp1a)); %Cp/Cp* Rep1
end
for j = 1:length(Cp1b)
    Cp1b_norm(j) = Cp1b(j)/Cp1b(length(Cp1b)); %Cp/Cp* Rep2
end
for j = 1:length(Cp1c)
    Cp1c_norm(j) = Cp1c(j)/Cp1c(length(Cp1c)); %Cp/Cp* Rep3
end

for j = 1:length(C1a)
    C1a_norm(j) = C1a(j)/C1a(length(C1a)); %C/C*
end
for j = 1:length(C1b)
    C1b_norm(j) = C1b(j)/C1b(length(C1b)); %C/C*
end
for j = 1:length(C1c)
    C1c_norm(j) = C1c(j)/C1c(length(C1c)); %C/C*
end

%% Calculate Kp data by linearisation and straight line fit
lnCp1a = log(1-Cp1a_norm); %linearised model - Rep1
lnCp1b = log(1-Cp1b_norm); %linearised model - Rep2
lnCp1c = log(1-Cp1c_norm); %linearised model - Rep3

%figure, plot(time2, lnCp1, 'o'), grid %Plot data points
%xlabel('time(s)'), ylabel('ln(1-C/C*)'), title('Linearised KP data based on first-order model for estimate KLa value')
lnCp1a = lnCp1a'; %Convert to row vector - Rep1
lnCp1b = lnCp1b'; %Convert to row vector - Rep2
lnCp1c = lnCp1c'; %Convert to row vector - Rep3

polylen2a = length(lnCp1a)-3; %Fit of a straight line - Rep1, coefficient is -Kp
polylen2b = length(lnCp1b)-4; %Fit of a straight line - Rep2, coefficient is -Kp
polylen2c = length(lnCp1c)-5; %Fit of a straight line - Rep3, coefficient is -Kp
```

```
61
62 [coeff2a, Kp_curvea] = polyfit(time2a(1:polylen2a),
       lnCp1a(1:polylen2a), 1) % - Rep1
63 [coeff2b, Kp_curveb] = polyfit(time2b(1:polylen2b),
       lnCp1b(1:polylen2b), 1) % - Rep2
64 [coeff2c, Kp_curvec] = polyfit(time2c(1:polylen2c),
       lnCp1c(1:polylen2c), 1) % - Rep3
65
66 Kpa = -coeff2a(1)
67 Kpb = -coeff2b(1)
68 Kpc = -coeff2c(1)
69
70 C1a_norm = C1a_norm'; %Convert to row vector
71 C1b_norm = C1b_norm'; %Convert to row vector
72 C1c_norm = C1c_norm'; %Convert to row vector
73 %%%%%%%%%%%%%%%%%%%%%%%%%%%%%%%%%%%%%%%%%%%%%%%%%%%%%%%%%%%%%%%%%%%%%%%%%%%%
74
75 %%%%%%%%%%%%%%%%%%%%%%%%%%%%%%%%%%%%%%%%%%%%%%%%%%%%%%%%%%%%%%%%%%%%%%%%%%%%
76 %%% Calculation of Kla data for 1st order model and
       linearisation to fit a
77 %%% straight line with gradient = -Kla
78 %%%%%%%%%%%%%%%%%%%%%%%%%%%%%%%%%%%%%%%%%%%%%%%%%%%%%%%%%%%%%%%%%%%%%%%%%%%%
79 lnC1a = log(1-C1a_norm'); %linearised model of C/C* -
       Rep1
80 lnC1b = log(1-C1b_norm'); %linearised model of C/C* -
       Rep2
81 lnC1c = log(1-C1c_norm'); %linearised model of C/C* -
       Rep3
82
83 lnC1a = lnC1a';    %Convert to row vector - Rep1
84 lnC1b = lnC1b';    %Convert to row vector - Rep2
85 lnC1c = lnC1c';    %Convert to row vector - Rep3
86
87 polylena = length(lnC1a)-1; % - Rep1
88 polylenb = length(lnC1b)-1; % - Rep2
89 polylenc = length(lnC1c)-1; % - Rep3
90
91 [coeffa, Kla_curvea] = polyfit(time1a(1:polylena), lnC1a
       (1:polylena), 1); %Fit of str line to data - Rep1
92 [coeffb, Kla_curveb] = polyfit(time1b(1:polylenb), lnC1b
       (1:polylenb), 1); %Fit of str line to data - Rep2
93 [coeffc, Kla_curvec] = polyfit(time1c(1:polylenc), lnC1c
       (1:polylenc), 1); %Fit of str line to data - Rep3
```

```
94
95  Kla_est1a = -coeffa(1) % - Rep1
96  Kla_est1b = -coeffb(1) % - Rep2
97  Kla_est1c = -coeffc(1) % - Rep3
98  %%%%%%%%%%%%%%%%%%%%%%%%%%%%%%%%%%%%%%%%%%%%%%%%%%%%%%%%%%%%%%%%%%%%%%%%%%%%
99
100 %%%%%%%%%%%%%%%%%%%%%%%%%%%%%%%%%%%%%%%%%%%%%%%%%%%%%%%%%%%%%%%%%%%%%%%%%%%%
101 %%% Fit of a Kla value to the obtained C/C* data using
        lsqcurvefit
102 %%%%%%%%%%%%%%%%%%%%%%%%%%%%%%%%%%%%%%%%%%%%%%%%%%%%%%%%%%%%%%%%%%%%%%%%%%%%
103 funK1a = @(Kla1a, time1a) 1 - exp(-Kla1a*time1a)
104 Kla1a = lsqcurvefit(funK1a, 0.02, time1a, C1a_norm)
105 Kla_esta = Kla1a;
106
107 funK1b = @(Kla1b, time1b) 1 - exp(-Kla1b*time1b)
108 Kla1b = lsqcurvefit(funK1b, 0.02, time1b, C1b_norm)
109 Kla_estb = Kla1b; %should be 0.0272
110
111 funK1c = @(Kla1c, time1c) 1 - exp(-Kla1c*time1c)
112 Kla1c = lsqcurvefit(funK1c, 0.02, time1c, C1c_norm)
113 Kla_estc = Kla1c; %should be 0.0272
114 %%%%%%%%%%%%%%%%%%%%%%%%%%%%%%%%%%%%%%%%%%%%%%%%%%%%%%%%%%%%%%%%%%%%%%%%%%%%
115
116 %%%%%%%%%%%%%%%%%%%%%%%%%%%%%%%%%%%%%%%%%%%%%%%%%%%%%%%%%%%%%%%%%%%%%%%%%%%%
117 %%% Fit of the 2nd order Kla value ot the C/C* data using
        lsqcurvefit
118 %%%%%%%%%%%%%%%%%%%%%%%%%%%%%%%%%%%%%%%%%%%%%%%%%%%%%%%%%%%%%%%%%%%%%%%%%%%%
119 funK2a = @(Kla_esta, time1a) 1 - 1/(Kpa - Kla_esta) * (
      Kpa*exp(-Kla_esta*time1a) - Kla_esta*exp(-Kpa*time1a))
      ;
120 Kla2a = lsqcurvefit(funK2a, Kla1a, time1a, C1a_norm)
121 Cpa = 1 - 1/(Kpa - Kla2a) * (Kpa*exp(-Kla2a*time1a) -
      Kla2a*exp(-Kpa*time1a));
122
123 funK2b = @(Kla_estb, time1b) 1 - 1/(Kpb - Kla_estb) * (
      Kpb*exp(-Kla_estb*time1b) - Kla_estb*exp(-Kpb*time1b))
      ;
124 Kla2b = lsqcurvefit(funK2b, Kla1b, time1b, C1b_norm)
125 Cpb = 1 - 1/(Kpb - Kla2b) * (Kpb*exp(-Kla2b*time1b) -
      Kla2b*exp(-Kpb*time1b));
126
127 funK2c = @(Kla_estc, time1c) 1 - 1/(Kpc - Kla_estc) * (
      Kpc*exp(-Kla_estc*time1c) - Kla_estc*exp(-Kpc*time1c))
```

```
    ;
Kla2c = lsqcurvefit(funK2c, Kla1c, time1c, C1c_norm)
Cpc = 1 - 1/(Kpc - Kla2c) * (Kpc*exp(-Kla2c*time1c) -
    Kla2c*exp(-Kpc*time1c));
%%%%%%%%%%%%%%%%%%%%%%%%%%%%%%%%%%%%%%%%%%%%%%%%%%%%%%%%%%%%%%%%%%%%%%%%%%%%

%%%%%%%%%%%%%%%%%%%%%%%%%%%%%%%%%%%%%%%%%%%%%%%%%%%%%%%%%%%%%%%%%%%%%%%%%%%%
%%% Write the results of Kp and Kla to excel file
%%%%%%%%%%%%%%%%%%%%%%%%%%%%%%%%%%%%%%%%%%%%%%%%%%%%%%%%%%%%%%%%%%%%%%%%%%%%
xlswrite(fullfile(dirname, filename), Kpa,    'Rep1', 'F2'
    );
xlswrite(fullfile(dirname, filename), Kpb,    'Rep1', 'F3'
    );
xlswrite(fullfile(dirname, filename), Kpc,    'Rep1', 'F4'
    );
Kpa, Kpb, Kpc %Output calculated values

xlswrite(fullfile(dirname, filename), Kla1a, 'Rep1', 'J2'
    );
xlswrite(fullfile(dirname, filename), Kla1b, 'Rep1', 'J3'
    );
xlswrite(fullfile(dirname, filename), Kla1c, 'Rep1', 'J4'
    );
Kla1a, Kla1b, Kla1c %Output calculated values

xlswrite(fullfile(dirname, filename), Kla2a, 'Rep1', 'N2'
    );
xlswrite(fullfile(dirname, filename), Kla2b, 'Rep1', 'N3'
    );
xlswrite(fullfile(dirname, filename), Kla2c, 'Rep1', 'N4'
    );
Kla2a, Kla2b, Kla2c %Output calculated values
%%%%%%%%%%%%%%%%%%%%%%%%%%%%%%%%%%%%%%%%%%%%%%%%%%%%%%%%%%%%%%%%%%%%%%%%%%%%
```

A.5 MATLAB Code for Image Analysis

A.5.1 Source Code for Bubble Detection

```
% close all; clear all; clc;
dirname = '<Insert file directory here>';
dirfiles = dir(fullfile(dirname,'*.jpg'));
imfiles = {dirfiles.name};
imInds = listdlg('ListString',imfiles,'PromptString','
    Select images for processing');

doCropping = false; % true|false
showFigures = false; % true|false
saveFigures = true; % true|false
saveExt = '.png';

%% Detecting an object using image segmentation
% An object can be easily detected in an image if the
    object has
% sufficient contrast from the background. We use edge
    detection and
% basic morphology tools to detect air bubbles in an
    alkane-aqueous
% suspension.

%% Step 1: Read image and crop
% Read in the |test.jpg| image, which is a test image.
warning('off','images:initSize:adjustingMag')
counter = 0;
summaryResults = zeros(length(imInds),1);
for imi = imInds
    counter = counter+1;
    if counter >=2, close all, end

    fname = imfiles{imi};
    fprintf('\n Processing: %s\n',fname)
    rawI = imread(fullfile(dirname,fname));

    if doCropping
        I = imcrop(rawI(:,:,1));
        close(gcf)
    else
```

```
35          I = rawI(:,:,1);
36      end
37
38      %% Step 2: Enhance Image
39      % To enhance the image for processing, several
            options are
40      % available:
41      %   'sharpen'    Sharpening
42      %   'filter'     Median Filtering
43      %   'contrast'   Contrast adjustment
44
45      enhOptions.sharpen.param = 0.2; % value 0 to 1
46      % contrast adjustment settings
47      % to determine settings visually, use imtool(I)
48      enhOptions.contrast.low  = 50;
49      enhOptions.contrast.high = 140;
50      enhOptions.order = {'contrast'};
51
52      enhobj = enhanceImage(enhOptions,showFigures);
53      enhI = enhobj.execute(I);
54
55      %% Step 3: Analyse Image
56      % Image analysis involves any combination of the
            following steps to
57      % effectively segement an image
58      %   'edge'          Bubble edge detection using
            filters
59      %   'dilate'        Image dilation (expand white
            pixels)
60      %   'erode'         Image erosion (expand black
            pixels)
61      %   'remborderobj'  Removing objects on border
62      %   'remnoise'      Removing noise (objects smaller
            than a certain size)
63      %   'binary'        Convert to binary image
64
65      % set analysis options
66      anOptions.edge.type               = 'sobel'; % 'sobel
            '|'canny'
67      anOptions.dilate.strel            = strel('disk',3);
68      anOptions.erode.strel             = strel('disk',5);
69      anOptions.remborderobj.threshold = 8; % 4|8
70      anOptions.remnoise.threshold      = 200;
```

```
71      anOptions.binary.threshold        = 65;
72      anOptions.fill                    = true;
73      anOptions.order = {'fill','erode','dilate','
            remborderobj','binary','remnoise'};
74
75      % analyse image
76      anobj = analyseImage(anOptions,showFigures);
77      anI = anobj.execute(enhI);
78
79      %% Step 4: Find the boundaries
80      % Concentrate only on the exterior boundaries.
            Option 'noholes'
81      % will accelerate the processing by preventing
            bwboundaries
82      % from searching for inner contours.
83
84      [B,L,N] = bwboundaries(anI,'noholes');
85      fprintf('\t %d boundaries detected\n',size(B,1))
86
87      if showFigures
88          % Display the label matrix and draw each boundary
89          figure('Units','normalized','Position',[0 0 1 1])
90          subplot(1,2,1), imshow(label2rgb(L, @jet, [.5 .5
                .5])), title('Boundaries')
91          % impixelinfo
92          hold on
93          for k = 1:length(B)
94              boundary = B{k};
95              plot(boundary(:,2), boundary(:,1), 'g', '
                    LineWidth', 1)
96          end
97
98          % superimpose boundaries onto original image
99          subplot(1,2,2), imshow(I), title('Superimposed')
100         hold on
101         for k = 1:length(B)
102             boundary = B{k};
103             plot(boundary(:,2), boundary(:,1), 'g', '
                    LineWidth', 1)
104         end
105
106         if saveFigures
107             saveas(gcf,fullfile(dirname,[fname,'
```

```
                _boundaries',saveExt]))
108         end
109     end
110
111     %% Step 5: Scaling
112     % Scaling is made easy using an interactive tool
113     % The tool allows the user to draw a line over a
            reference of known
114     % dimensions in the original image. Once satisfied
            with the selection,
115     % double click on the line to return the dimensions.
            It doesn't matter if
116     % the line is vertical or horizontal, the direction
            of greatest magnitude
117     % will be used.
118
119     % scaling only required for first image, assuming
            their the same for all
120     % images
121     if counter == 1
122         figure('Units','normalized','Position',[0 0 1 1])
123         imshow(rgb2gray(rawI));
124         refH = imline(gca);
125         position = wait(refH);
126         close(gcf)
127         pixLength = max(position(3),position(4));
128
129         answer = inputdlg({'Reference length (mm)'},...
130             'Reference measurements',1,{'10'});
131         mmLength = str2double(answer{1});
132
133         scale = mmLength/pixLength; % mm/pix
134     end
135
136     %% Step 6: Extract Data
137     % Estimate each object's area and perimeter. Use
            these results to
138     % form a simple metric indicating the roundness of an
            object:
139     %  metric = 4*pi*area/perimeter^2.
140     % This metric is equal to one only for a circle and
            it is less
141     % than one for any other shape. The discrimination
```

```
142     % process can be controlled by setting an appropriate threshold. In this example
143     % use a threshold of 0.76.
144
145     % get statistics
146     stats = regionprops(L, 'Area', 'Majoraxislength','Minoraxislength',...
147         'Eccentricity', 'EquivDiameter' ,'Perimeter', 'Centroid','Orientation');
148
149     % centroid has 2 entries, handle separately
150     centroid = vertcat(stats.Centroid);
151     orientation = vertcat(stats.Orientation);
152     eccentricity = vertcat(stats.Eccentricity);
153     % area scales differently, handle separately
154     area = vertcat(stats.Area)*scale^2;
155
156     % rest of stats all scale the same, handle as matrix
157     stats = rmfield(stats,{'Centroid','Area','Orientation','Eccentricity'});
158     stats_cell = struct2cell(stats);
159     stats_mat = cell2mat(stats_cell)';
160     stats_mat = stats_mat*scale;
161     heads = fieldnames(stats);
162
163     % calculate metric
164     perimCol = strcmpi('Perimeter',heads');
165     metric = 4*pi*area./(stats_mat(:,perimCol).^2);
166
167     % combine information in matrix
168     results = horzcat(area,stats_mat,metric,centroid,eccentricity);
169     headings = ['Area',heads','Metric','Centroid x','Centroid y','Eccentricity'];
170
171     % Display boundary overlays
172     figure, imshow(I), title('Superimposed boundaries with centroid overlays')
173     hold on
174     for k = 1:length(B)
175         boundary = B{k};
176         plot(boundary(:,2), boundary(:,1), 'g', '
```

```
            LineWidth', 1)
177         hold on
178         %     viscircles(centroid(k,:),stats(k).
                EquivDiameter,'EdgeColor','r','LineStyle',':')
179         %     ellipse(stats(k).MajorAxisLength,stats(k).
                MinorAxisLength,...
180         %         orientation(k,:),centroid(k,1),centroid
                (k,2))
181     end
182     hold on, plot(centroid(:,1),centroid(:,2),'*r')
183
184     if saveFigures
185         saveas(gcf,fullfile(dirname,[fname,'
                _boundaryOverlays',saveExt]));
186     end
187
188     % Display labeled bubbles
189     % objects with sphericity larger than threshold are
            marked with a
190     % black square and number
191     sphThresh = 0.6; % sphericity threshold
192     sphMask = metric>sphThresh;
193     sphNum = find(sphMask==1);
194     fprintf('\t %d boundaries labeled\n', length(sphNum))
195
196     figure, imshow(I), title('Labeled boundaries')
197     hold on
198     bCount = 0;
199     for k = 1:length(B)
200         boundary = B{k};
201         plot(boundary(:,2), boundary(:,1), 'g', '
                LineWidth', 1)
202         hold on
203         if sphMask(k)
204             bCount = bCount+1;
205             metricStr = num2str(bCount);
206             hold on, plot(centroid(k,1),centroid(k,2),'sk
                    ')
207             hold on, text(boundary(1,2)-10,boundary(1,1)
                    -13,metricStr,...
208                 'Color','y','FontSize',12,'FontWeight','
                        bold');
209         end
```

```
210         end
211         if saveFigures
212             saveas(gcf,fullfile(dirname,[fname,'_labeled',
                    saveExt]))
213         end
214
215         % creat summary results
216         validArea = results(sphMask,1);
217         summaryResults(counter,1) = median(validArea);
218         summaryResults(counter,2) = mean(validArea);
219         summaryHeadings = {'MedianArea','MeanArea'};
220
221         %% Step 7: Write data to excel spreadsheet
222         savename = sprintf('%s.xlsx',strrep(fname,'.bmp',''))
                ;
223         xlswrite(fullfile(dirname,savename),headings,1,'A1')
224         xlswrite(fullfile(dirname,savename),results,1,'A2')
225
226
227 end
228
229 % Save summary results to excel
230 summaryName = 'Summary.xlsx';
231 imnames = imfiles(imInds);
232 xlswrite(fullfile(dirname,summaryName),imnames',1,'A2')
233 xlswrite(fullfile(dirname,summaryName),summaryHeadings,1,
        'B1')
234 xlswrite(fullfile(dirname,summaryName),summaryResults,1,'
        B2')
```

A.5.2 Class Definition for Image Enhancement

```
1  classdef enhanceImage < handle
2
3      properties
4          Show
5          Options
6          Image
7          ExecuteOrder
8
9          FigHandel
10         Counter
11         Rows
```

```
12          Cols
13
14      end
15
16      methods
17
18          function this = enhanceImage(options,show)
19
20              this.Options = options;
21              this.Show = show;
22          end
23
24          function I = execute(this,I)
25              this.Image = I;
26              order = this.Options.order;
27
28              if this.Show
29                  this.FigHandel = figure('Units','
                        normalized','Position',[0 0 1 1]);
30                  this.Counter = 0;
31                  this.Rows = 3;
32                  this.Cols = 3;
33                  this.plotImage('Original image')
34              end
35
36              for i = 1:length(order)
37                  fcn = order{i};
38                  this.(fcn);
39              end
40              I = this.Image;
41
42          end
43
44
45          %% Sharpen Image
46          function sharpen(this)
47              param = this.Options.sharpen.param;
48
49              % The FSPECIAL function produces several
                    kinds of predefined
50              %filters, in the form of correlation kernels.
51              sfilt = fspecial('unsharp', param); % '
                    unsharp',0.5
```

```
52
53              %This may be applied directly to the image
                    data using IMFILTER.
54              this.Image = imfilter(this.Image, sfilt);
55
56              if this.Show
57                  this.plotImage({'Sharpened';sprintf('
                        Degree: %g',param)});
58              end
59          end
60
61          %% Median filtering
62          % Median filtering produces each output pixel as
                an average of
63          % the pixel values in the neighborhood of the
                correpsonding input
64          % pixel as determined by the median of the
                neighborhood pixels.
65          function filter(this)
66              this.Image = medfilt2(this.Image);
67              if this.Show
68                  this.plotImage('Median filtered');
69              end
70          end
71
72          %% Enhance Contrast
73          function contrast(this)
74              low = this.Options.contrast.low;
75              high = this.Options.contrast.high;
76
77              this.Image = imadjust(this.Image,[low/255
                    high/255]);
78
79              if this.Show
80                  this.plotImage({'Contrast Enhanced';
                        sprintf('low: %g    high: %g',low,high)
                        });
81              end
82
83          end
84
85          function plotImage(this,text)
86              this.Counter = this.Counter + 1;
```

```
87                subplot(this.Rows,this.Cols,this.Counter)
88                imshow(this.Image)
89                title(text)
90            end
91
92        end
93    end
```

A.5.3 Class Definition for Image Analysis

```
1   classdef analyseImage < handle
2
3       properties
4           IsInverted % true: background black
5           IsBinary
6           Show
7           Options
8           Image
9           ExecuteOrder
10
11          FigHandel
12          Counter
13          Rows
14          Cols
15      end
16
17      methods
18          function this = analyseImage(options,show)
19
20              this.Options = options;
21              this.Show = show;
22              this.IsInverted = false;
23          end
24
25          function I = execute(this,I)
26              this.Image = I;
27              order = this.Options.order;
28
29              if this.Show
30                  this.FigHandel = figure('Units','
                        normalized','Position',[0 0 1 1]);
31                  this.Counter = 0;
32                  this.Rows = 3;
```

```
33                  this.Cols = 3;
34                  this.plotImage('Original image')
35              end
36
37              for i = 1:length(order)
38                  fcn = order{i};
39                  this.(fcn);
40              end
41              I = this.Image;
42
43          end
44
45          %% Edge detection
46          function edge(this)
47              type = this.Options.edge.type;
48              [this.Image, ~] = edge(this.Image, type);
49
50              if this.Show
51                  this.plotImage({'Edge detect:',type})
52              end
53
54              this.IsInverted = true;
55          end
56
57          %% Dilate image
58          function dilate(this)
59
60              seD = this.Options.dilate.strel;
61              this.Image = imdilate(this.Image,seD);
62
63              if this.Show
64                  this.plotImage({'Dilated'})
65              end
66
67          end
68
69          %% Fill image
70          function fill(this)
71
72              % invert only if not using edge detection
73              if ~this.IsInverted
74                  this.Image = imsubtract(uint8(255*ones(
                        size(this.Image))),this.Image);
```

```
75              end
76
77              this.Image = imfill(this.Image,'holes');
78              if this.Show
79                  this.plotImage('Filled')
80              end
81
82          end
83
84          %% Create binary
85          function binary(this)
86              if this.IsBinary
87                  return
88              end
89              thresh = this.Options.binary.threshold;
90              this.Image = im2bw(this.Image,thresh/255);
91
92              if this.Show
93                  this.plotImage({'Binary image',sprintf('%
                        g threshold',thresh)})
94              end
95
96          end
97
98          %% Remove connected objects on border
99          function remborderobj(this)
100             thresh = this.Options.remborderobj.threshold;
101
102             this.Image = imclearborder(this.Image, thresh
                    );
103
104             if this.Show
105                 this.plotImage({'Border connections
                        removed',sprintf('threshold: %g',
                        thresh)})
106             end
107         end
108
109         %% Errode the object
110         function erode(this)
111             seE = this.Options.erode.strel;
112             this.Image = imerode(this.Image, seE);
113
```

```
114                 if this.Show
115                     this.plotImage('Erroded')
116                 end
117             end
118
119             %% Remove the noise
120             function remnoise(this)
121                 thresh = this.Options.remnoise.threshold;
122
123                 this.Image = bwareaopen(this.Image,thresh);
124
125                 if this.Show
126                     this.plotImage({'Noise removed',sprintf('
                            threshold %g',thresh)})
127                 end
128
129             end
130
131             function plotImage(this,text)
132                 this.Counter = this.Counter + 1;
133                 subplot(this.Rows,this.Cols,this.Counter)
134                 imshow(this.Image)
135                 title(text)
136             end
137         end % method
138 end % classdef
```

A.6 Experimental Results

Table A.3: Sauter Mean Diameter data obtained in corn flour systems

Experiment	Alkane concentration (vol %)	Solids Loading (g/l)	Superficial Gas Velocity (cm/s)	Replicate 1	Replicate 2	Replicate 3
1	7,88	1,62	1,62	2,29	2,34	2,27
2	7,88	1,62	2,38	2,45	2,54	2,52
3	7,88	4,88	1,62	2,43	2,44	2,38
4	7,88	4,88	2,38	2,35	2,64	2,50
5	14,62	1,62	1,62	2,65	2,54	2,61
6	14,62	1,62	2,38	2,61	2,51	2,68
7	14,62	4,88	1,62	2,54	2,52	2,55
8	14,62	4,88	2,38	2,54	2,60	2,58
9	2,5	3,25	2	2,34	2,70	2,50
10	20	3,25	2	2,38	2,43	2,50
11	11,25	0,5	2	2,61	2,57	2,58
12	11,25	6	2	2,64	2,78	2,61
13	11,25	3,25	1	2,07	2,05	2,24
14	11,25	3,25	3	2,58	2,60	2,67
15	11,25	3,25	2	2,48	2,49	2,67
16	11,25	3,25	2	2,64	2,58	2,54

Table A.4: Gas Holdup data obtained in corn flour systems

Experiment	Alkane concentration (vol %)	Solids Loading (g/l)	Superficial Gas Velocity (cm/s)	Replicate 1	Replicate 2	Replicate 3
1	7,88	1,62	1,62	5,73	6,70	5,73
2	7,88	1,62	2,38	7,65	6,70	8,59
3	7,88	4,88	1,62	4,74	5,73	5,73
4	7,88	4,88	2,38	8,12	9,86	8,59
5	14,62	1,62	1,62	5,24	6,22	5,73
6	14,62	1,62	2,38	7,18	8,59	7,89
7	14,62	4,88	1,62	6,22	6,22	6,70
8	14,62	4,88	2,38	8,12	7,65	8,59
9	2,5	3,25	2	8,40	8,40	8,12
10	20	3,25	2	8,12	9,05	8,59
11	11,25	0,5	2	8,12	8,59	7,65
12	11,25	6	2	8,59	7,65	7,65
13	11,25	3,25	1	4,23	3,72	3,72
14	11,25	3,25	3	11,92	10,84	10,84
15	11,25	3,25	2	7,65	8,59	8,59
16	11,25	3,25	2	8,59	7,65	8,59

Table A.5: Interfacial area data obtained in corn flour systems

Experiment	Alkane concentration (vol %)	Solids Loading (g/l)	Superficial Gas Velocity (cm/s)	Replicate 1	Replicate 2	Replicate 3
1	7,88	1,62	1,62	149,9	171,6	151,4
2	7,88	1,62	2,38	187,6	158,3	204,8
3	7,88	4,88	1,62	117,2	141,1	144,1
4	7,88	4,88	2,38	207,0	224,1	205,9
5	14,62	1,62	1,62	118,4	146,9	131,8
6	14,62	1,62	2,38	164,9	204,9	176,6
7	14,62	4,88	1,62	146,7	147,8	157,8
8	14,62	4,88	2,38	192,1	176,6	199,6
9	2,5	3,25	2	215,2	186,9	194,9
10	20	3,25	2	204,9	223,0	205,9
11	11,25	0,5	2	187,1	200,1	177,7
12	11,25	6	2	195,3	165,1	176,2
13	11,25	3,25	1	122,7	108,8	99,8
14	11,25	3,25	3	277,4	249,9	244,0
15	11,25	3,25	2	185,4	207,0	192,8
16	11,25	3,25	2	195,4	177,7	202,6

Table A.6: K_P data obtained in corn flour systems

Experiment	Alkane Concentration (vol %)	Solids Loading (g/l)	Superficial Gas Velocity (cm/s)	Replicate 1	Replicate 2	Replicate 3
1	7,88	1,62	1,62	0,0490	0,0526	0,0501
2	7,88	1,62	2,38	0,0507	0,0518	0,0545
3	7,88	4,88	1,62	0,0564	0,0530	0,0562
4	7,88	4,88	2,38	0,102	0,109	0,109
5	14,62	1,62	1,62	0,0859	0,0861	0,0860
6	14,62	1,62	2,38	0,0610	0,0592	0,0633
7	14,62	4,88	1,62	0,0606	0,0604	0,0688
8	14,62	4,88	2,38	0,0801	0,0778	0,0764
9	2,5	3,25	2	0,0892	0,0869	0,0891
10	20	3,25	2	0,0583	0,0586	0,0584
11	11,25	0,5	2	0,0599	0,0636	0,0576
12	11,25	6	2	0,0909	0,0926	0,103
13	11,25	3,25	1	0,0584	0,0583	0,0592
14	11,25	3,25	3	0,0430	0,0443	0,0455
15	11,25	3,25	2	0,0474	0,0478	0,0483
16	11,25	3,25	2	0,0579	0,0598	0,0629

Table A.7: $K_L a$ data obtained in corn flour systems

Experiment	Alkane Concentration (vol %)	Solids Loading (g/l)	Superficial Gas Velocity (cm/s)	Replicate 1	Replicate 2	Replicate 3
1	7,88	1,62	1,62	0,0456	0,0457	0,0489
2	7,88	1,62	2,38	0,0384	0,0390	0,0390
3	7,88	4,88	1,62	0,0418	0,0392	0,0376
4	7,88	4,88	2,38	0,0336	0,0320	0,0365
5	14,62	1,62	1,62	0,0482	0,0535	0,0536
6	14,62	1,62	2,38	0,0369	0,0412	0,0396
7	14,62	4,88	1,62	0,0275	0,0313	0,0294
8	14,62	4,88	2,38	0,0426	0,0360	0,0360
9	2,5	3,25	2	0,0486	0,0462	0,0424
10	20	3,25	2	0,0348	0,0381	0,0319
11	11,25	0,5	2	0,0381	0,0410	0,0384
12	11,25	6	2	0,0209	0,0248	0,0221
13	11,25	3,25	1	0,0324	0,0338	0,0326
14	11,25	3,25	3	0,0716	0,0638	0,0676
15	11,25	3,25	2	0,0465	0,0442	0,0449
16	11,25	3,25	2	0,0398	0,0387	0,0435

Table A.8: Sauter mean diameter data obtained in non-viable yeast systems

Experiment	Alkane concentration (vol %)	Solids Loading (g/l)	Superficial Gas Velocity (cm/s)	Replicate 1	Replicate 2	Replicate 3
1	7,88	1,62	1,62	1,61	1,63	1,62
2	7,88	1,62	2,38	1,77	1,76	1,77
3	7,88	4,88	1,62	1,64	1,69	1,67
4	7,88	4,88	2,38	1,69	1,78	1,74
5	14,62	1,62	1,62	1,62	1,54	1,58
6	14,62	1,62	2,38	1,66	1,71	1,69
7	14,62	4,88	1,62	1,54	1,70	1,62
8	14,62	4,88	2,38	1,76	1,85	1,80
9	2,5	3,25	2	1,89	1,81	1,85
10	20	3,25	2	1,56	1,53	1,54
11	11,25	0,5	2	2,01	2,26	2,13
12	11,25	6	2	1,50	1,70	1,60
13	11,25	3,25	1	1,61	1,44	1,52
14	11,25	3,25	3	1,86	1,93	1,90
15	11,25	3,25	2	1,67	1,54	1,61
16	11,25	3,25	2	1,52	1,58	1,55

Table A.9: Gas Holdup data obtained in non-viable yeast systems

Experiment	Alkane concentration (vol %)	Solids Loading (g/l)	Superficial Gas Velocity (cm/s)	Replicate 1	Replicate 2	Replicate 3
1	7,88	1,62	1,62	4,74	5,24	4,99
2	7,88	1,62	2,38	5,73	6,22	5,97
3	7,88	4,88	1,62	4,23	4,74	4,48
4	7,88	4,88	2,38	4,74	5,24	4,99
5	14,62	1,62	1,62	4,23	3,72	3,98
6	14,62	1,62	2,38	4,74	5,24	4,99
7	14,62	4,88	1,62	4,23	4,74	4,48
8	14,62	4,88	2,38	5,24	5,73	5,48
9	2,5	3,25	2	5,24	4,74	4,99
10	20	3,25	2	4,74	5,24	4,99
11	11,25	0,5	2	3,72	4,23	3,98
12	11,25	6	2	4,74	5,24	4,99
13	11,25	3,25	1	3,21	2,69	2,95
14	11,25	3,25	3	5,73	6,70	6,22
15	11,25	3,25	2	4,74	4,23	4,48
16	11,25	3,25	2	4,23	4,74	4,48

Table A.10: Interfacial area data obtained in non-viable yeast systems

Experiment	Alkane concentration (vol %)	Solids Loading (g/l)	Superficial Gas Velocity (cm/s)	Replicate 1	Replicate 2	Replicate 3
1	7,88	1,62	1,62	176,2	192,7	184,4
2	7,88	1,62	2,38	193,9	212,3	203,1
3	7,88	4,88	1,62	154,4	167,9	161,2
4	7,88	4,88	2,38	168,3	176,3	172,3
5	14,62	1,62	1,62	156,8	145,0	150,9
6	14,62	1,62	2,38	171,2	183,3	177,3
7	14,62	4,88	1,62	164,8	167,3	166,0
8	14,62	4,88	2,38	178,8	186,3	182,6
9	2,5	3,25	2	166,3	156,6	161,5
10	20	3,25	2	182,1	205,6	193,8
11	11,25	0,5	2	111,1	112,5	111,8
12	11,25	6	2	189,8	185,0	187,4
13	11,25	3,25	1	119,7	112,0	115,8
14	11,25	3,25	3	184,8	207,9	196,3
15	11,25	3,25	2	169,7	165,0	167,4
16	11,25	3,25	2	167,1	179,6	173,4

A.7 Reproducibility of Data

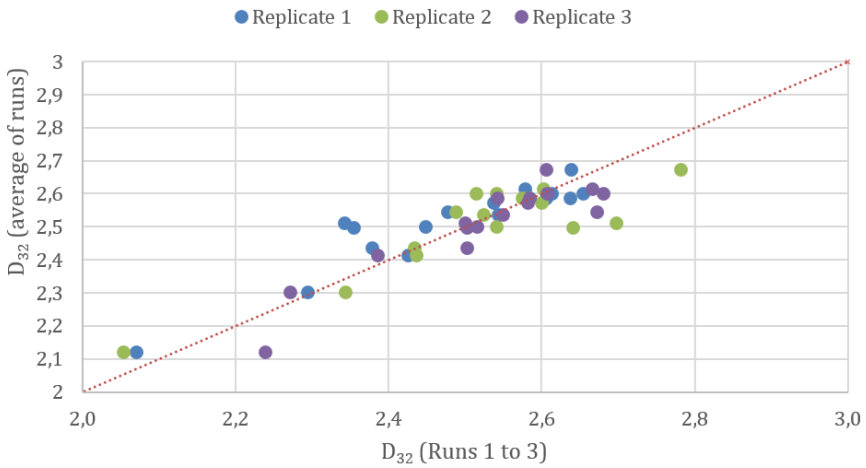

Figure A.2: Reproducibility of Sauter Mean Diameter values obtained in systems containing inert solids

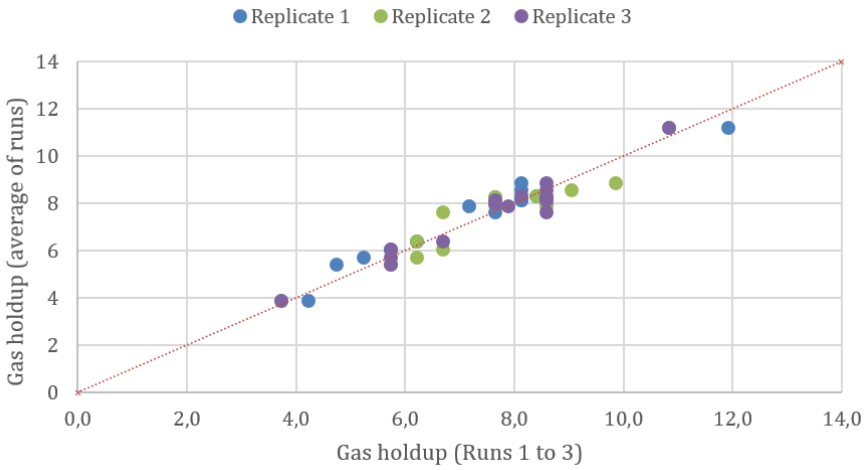

Figure A.3: Reproducibility of gas holdup values obtained in systems containing inert solids

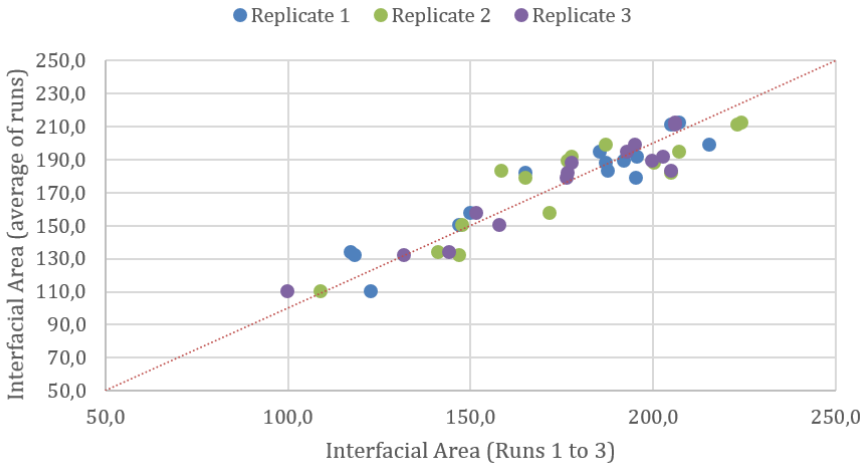

Figure A.4: Reproducibility of interfacial area values obtained in systems containing inert solids

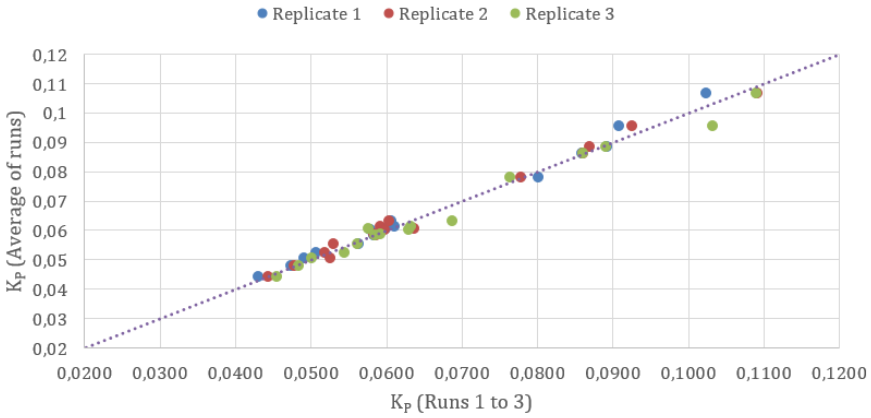

Figure A.5: Reproducibility of K_P values obtained in systems containing inert solids

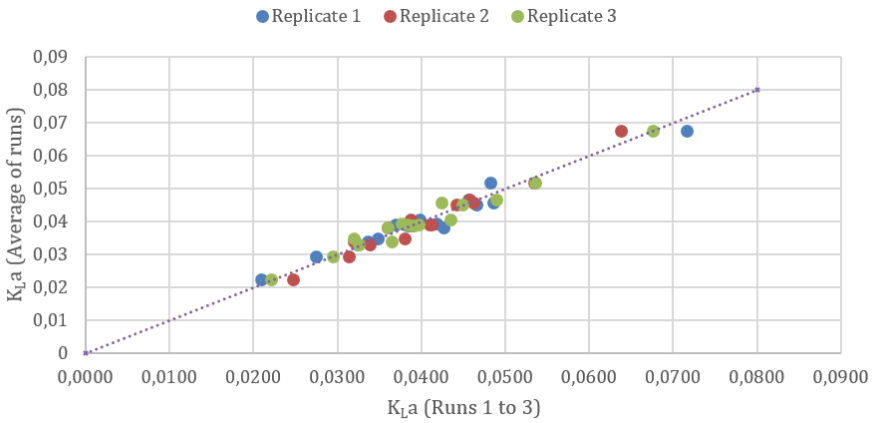

Figure A.6: Reproducibility of K_La values obtained in systems containing inert solids

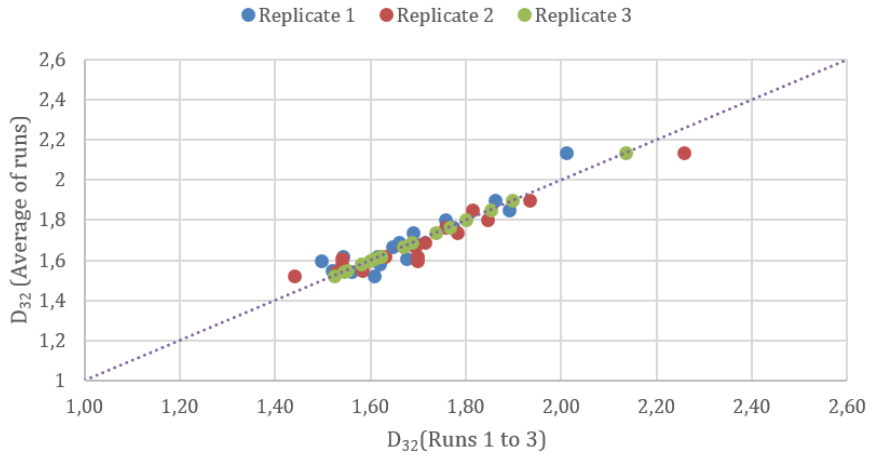

Figure A.7: Reproducibility of Sauter Mean Diameter values obtained in systems containing yeast solids

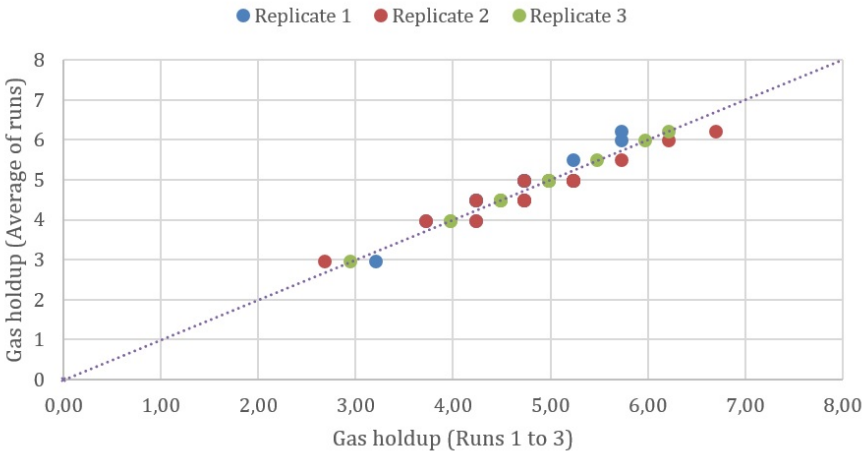

Figure A.8: Reproducibility of gas holdup values obtained in systems containing yeast solids

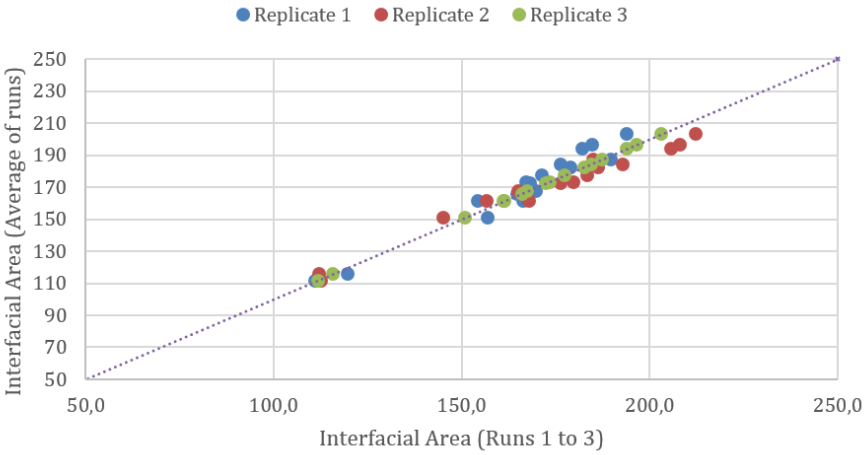

Figure A.9: Reproducibility of interfacial area values obtained in systems containing yeast solids

A.8 Sauter Mean Diameter in Systems Containing Inert Solids

A.8.1 Dependence of Sauter Mean Diameter on Alkane Concentration and Superficial Gas Velocity at Constant Solids Loading

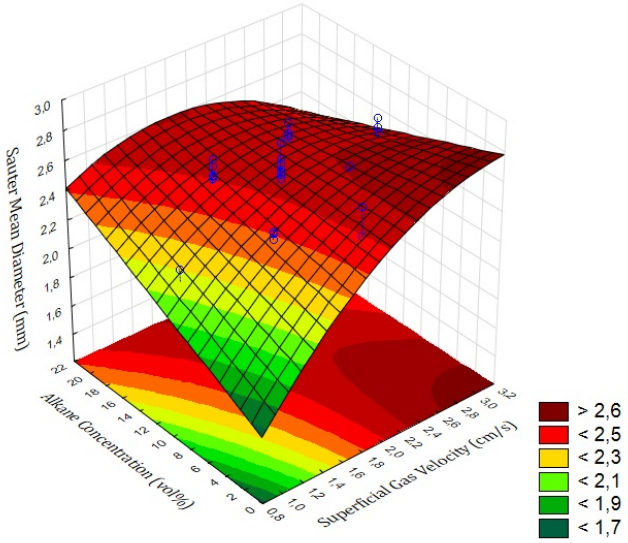

Figure A.10: Influence of the alkane concentration and superficial gas velocity on D_{32} in corn flour at constant solids loading (low value of 1.62 g/l)

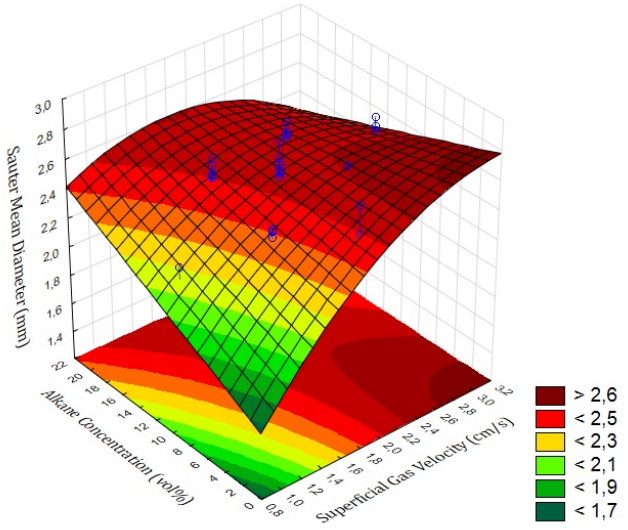

Figure A.11: Influence of the alkane concentration and superficial gas velocity on D_{32} in corn flour at constant solids loading (high value of 4.88 g/l)

A.8.2 Dependence of Sauter Mean Diameter on Alkane Concentration and Solids Loading at Constant Superficial Gas Velocity

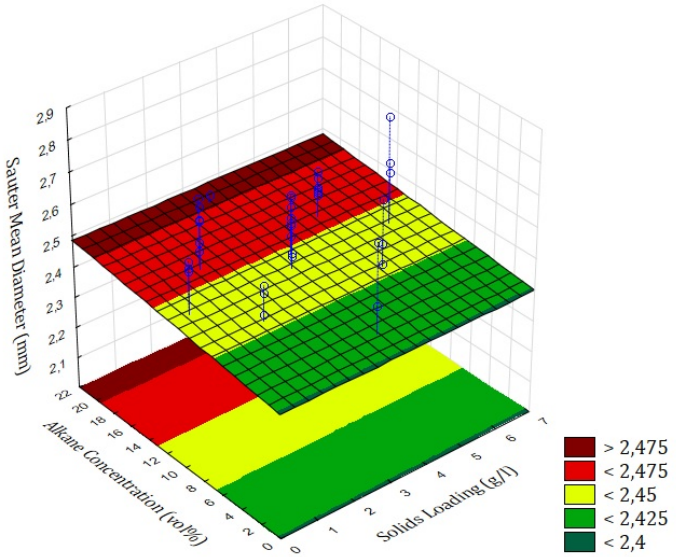

Figure A.12: Influence of the alkane concentration and solid loading on D_{32} in corn flour at constant superficial gas velocity (low value of 1.62 cm/s)

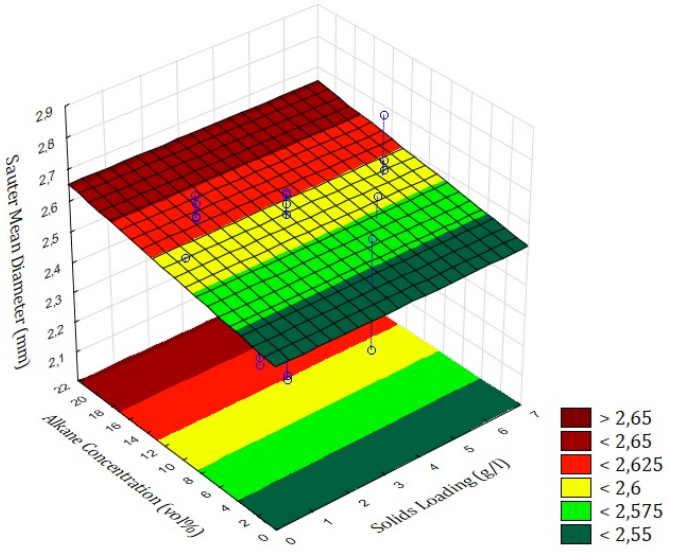

Figure A.13: Influence of the alkane concentration and solid loading on D_{32} in corn flour at constant superficial gas velocity (high value of 2.38 cm/s)

A.8.3 Dependence of Sauter Mean Diameter on Superficial Gas Velocity and Solids Loading at Constant Alkane Concentration

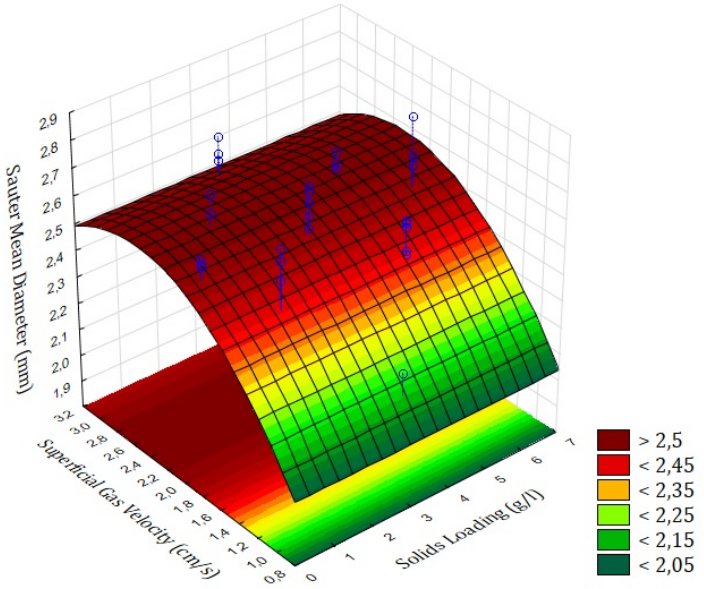

Figure A.14: Influence of the superficial gas velocity and solid loading on D_{32} in corn flour at constant alkane concentration (low value of 7.88 vol%)

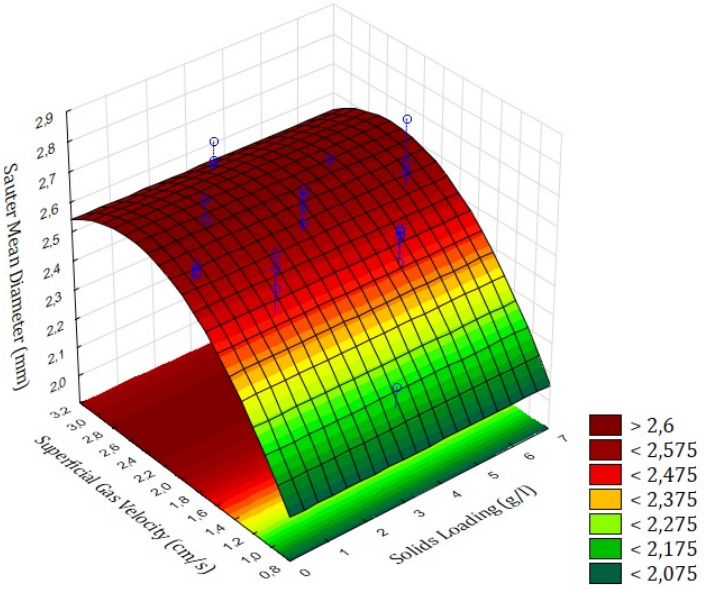

Figure A.15: Influence of the superficial gas velocity and solid loading on D_{32} in corn flour at constant alkane concentration (high value of 14.62 vol%)

A.9 Gas Holdup in Systems Containing Inert Solids

A.9.1 Dependence of Gas Holdup on Alkane Concentration and Superficial Gas Velocity at Constant Solids Loading

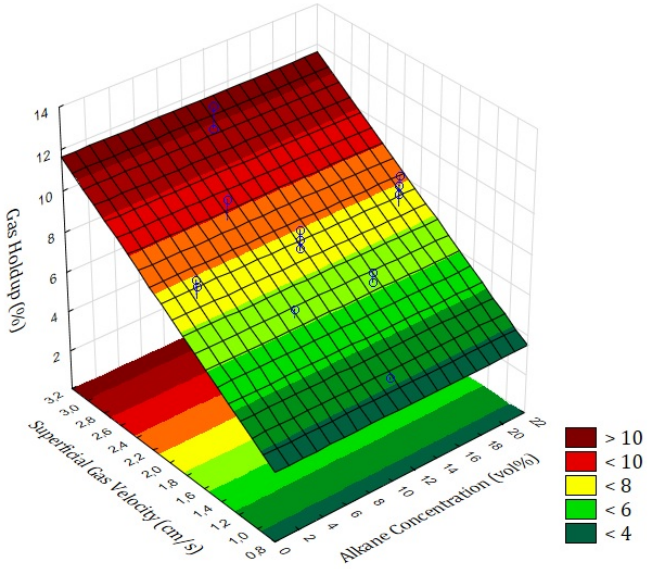

Figure A.16: Influence of the superficial gas velocity and alkane concentration on ϵ_G in corn flour at constant solid loading (low value of 1.62 g/l)

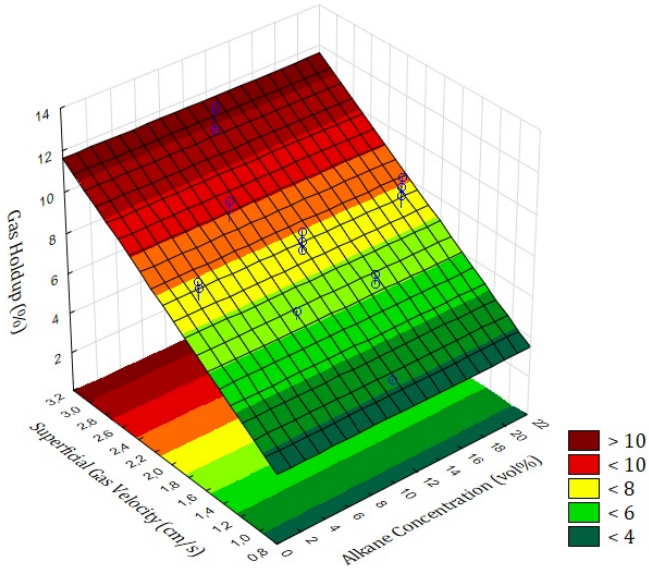

Figure A.17: Influence of the superficial gas velocity and alkane concentration on ϵ_G in corn flour at constant solid loading (high value of 4.88 g/l)

A.9.2 Dependence of Gas Holdup on Superficial Gas Velocity and Solids Loading at Constant Alkane Concentration

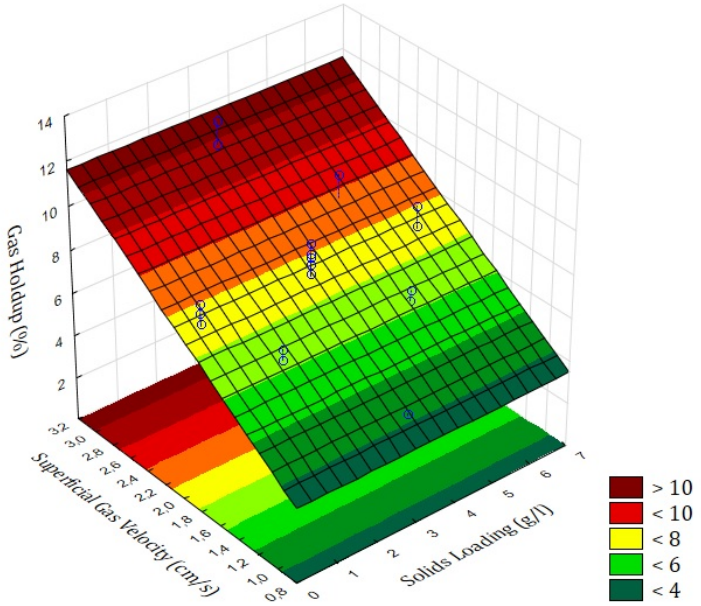

Figure A.18: Influence of the superficial gas velocity and solid loading on ϵ_G in corn flour at constant alkane concentration (low value of 7.88 vol%)

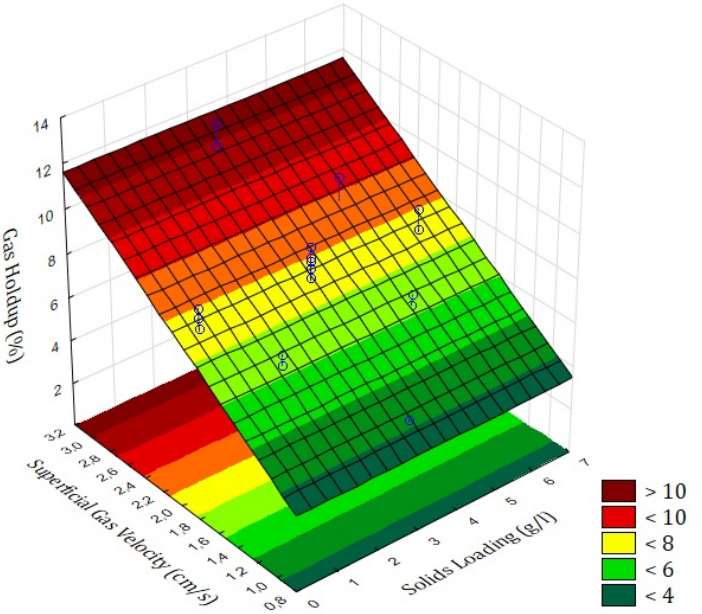

Figure A.19: Influence of the superficial gas velocity and solid loading on ϵ_G in corn flour at constant alkane concentration (high value of 14.62 vol%)

A.9.3 Dependence of Gas Holdup on Alkane Concentration and Solids Loading at Constant Superficial Gas Velocity

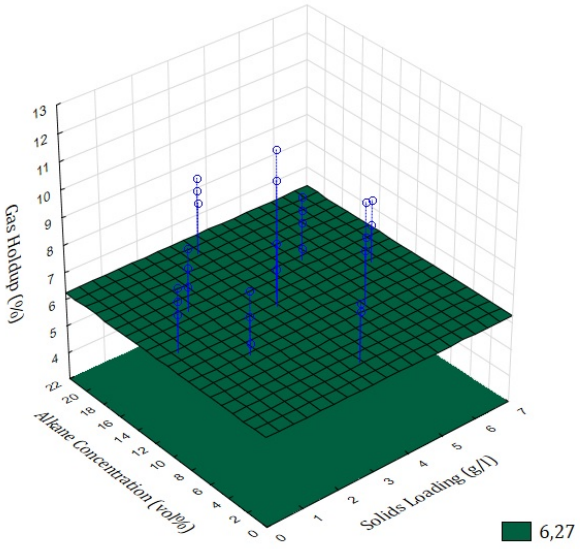

Figure A.20: Influence of the alkane concentration and solid loading on ϵ_G in corn flour at constant superficial gas velocity (low value of 1.62 cm/s)

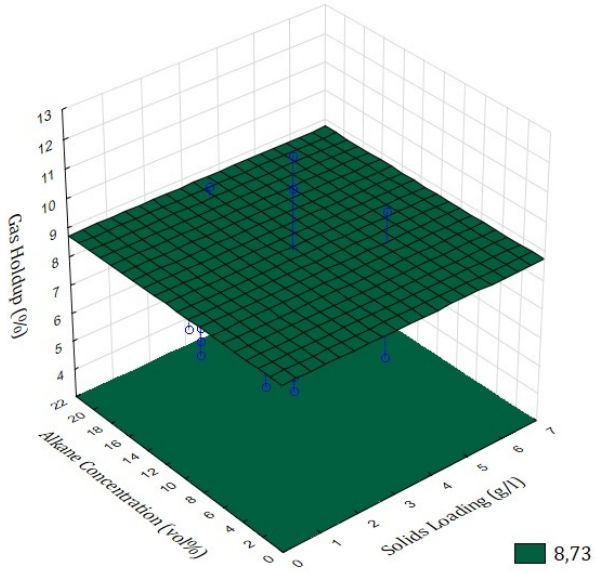

Figure A.21: Influence of the alkane concentration and solid loading on ϵ_G in corn flour at constant superficial gas velocity (high value of 2.38 cm/s)

A.10 Interfacial Area in Systems Containing Inert Solids

A.10.1 Dependence of Interfacial Area on Alkane Concentration and Superficial Gas Velocity at Constant Solids Loading

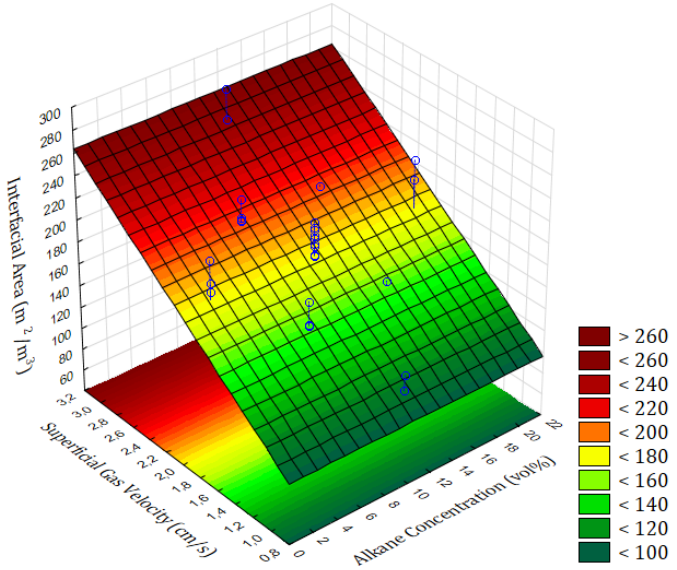

Figure A.22: Influence of the alkane concentration and superficial gas velocity on interfacial area in corn flour at constant solid loading (low value of 1.62 g/l)

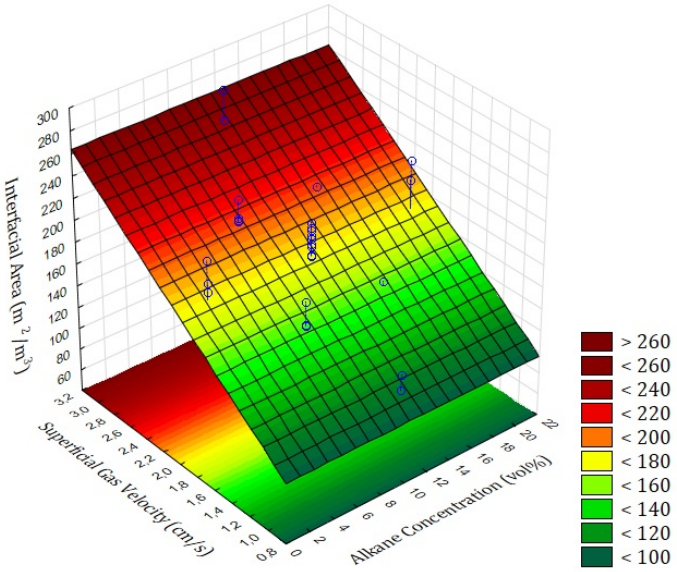

Figure A.23: Influence of the alkane concentration and superficial gas velocity on interfacial area in corn flour at constant solid loading (high value of 2.38 g/l)

A.10.2 Dependence of Interfacial Area on Superficial Gas Velocity and Solids Loading at Constant Alkane Concentration

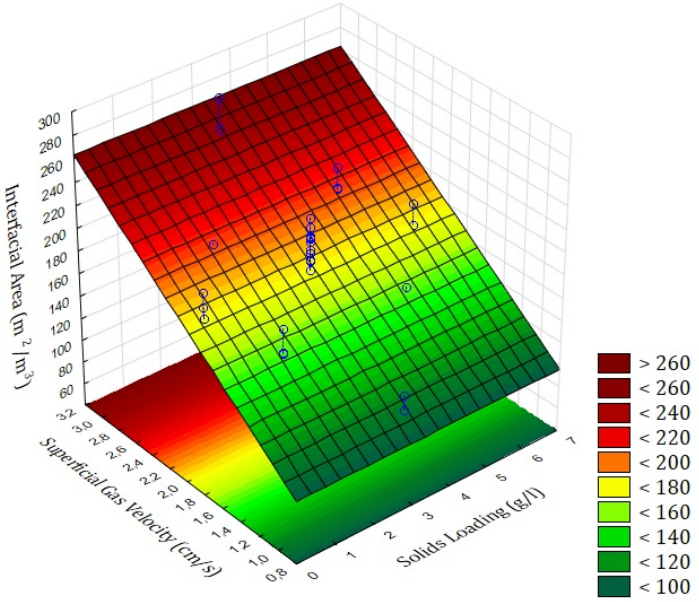

Figure A.24: Influence of the superficial gas velocity and solid loading on interfacial area in corn flour at constant alkane concentration (low value of 7.88 vol%)

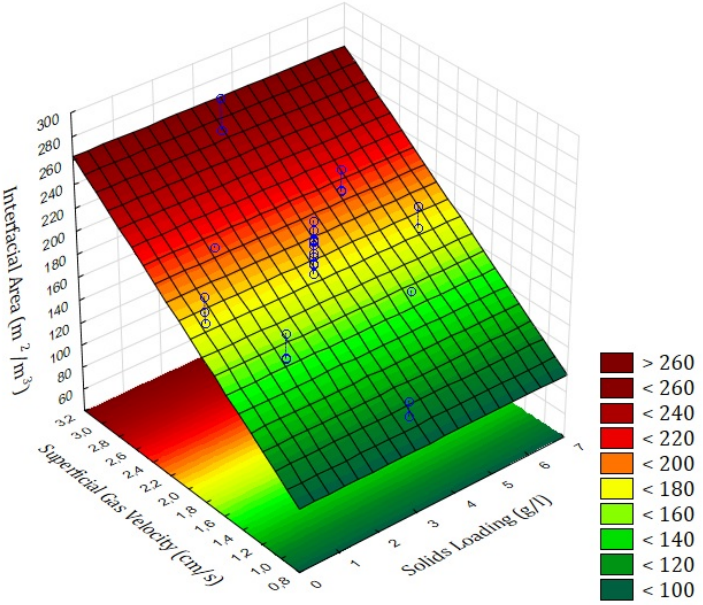

Figure A.25: Influence of the superficial gas velocity and solid loading on interfacial area in corn flour at constant alkane concentration (high value of 14.62 vol%)

A.10.3 Dependence of Interfacial Area on Alkane Concentration and Solids Loading at Constant Superficial Gas Velocity

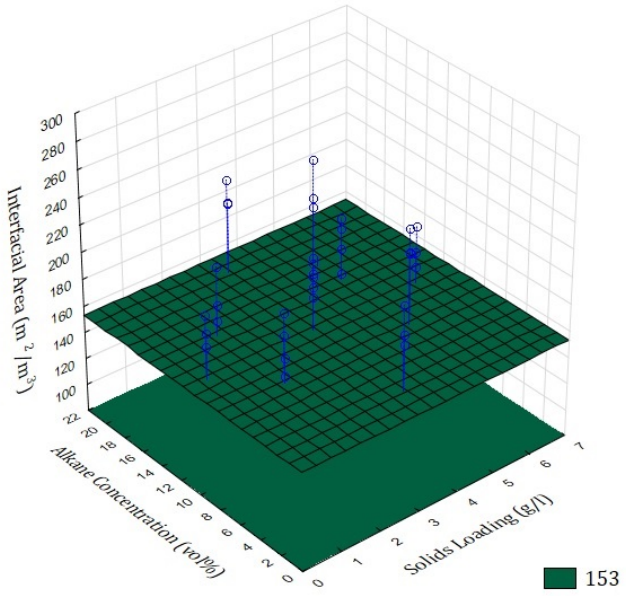

Figure A.26: Influence of the alkane concentration and solid loading on interfacial area in corn flour at constant superficial gas velocity (low value of 1.62 cm/s)

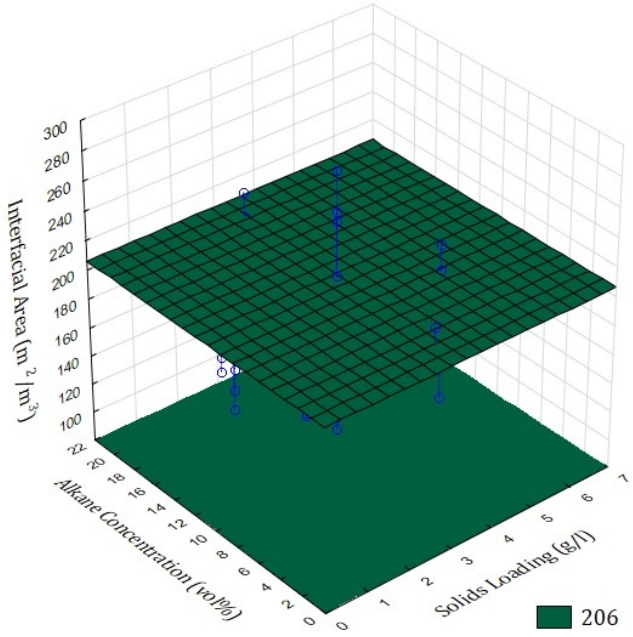

Figure A.27: Influence of the alkane concentration and solid loading on interfacial area in corn flour at constant superficial gas velocity (high value of 2.38 cm/s)

A.11 K_P in Systems Containing Inert Solids

A.11.1 Dependence of K_P on Alkane Concentration and Superficial Gas Velocity at Constant Solids Loading

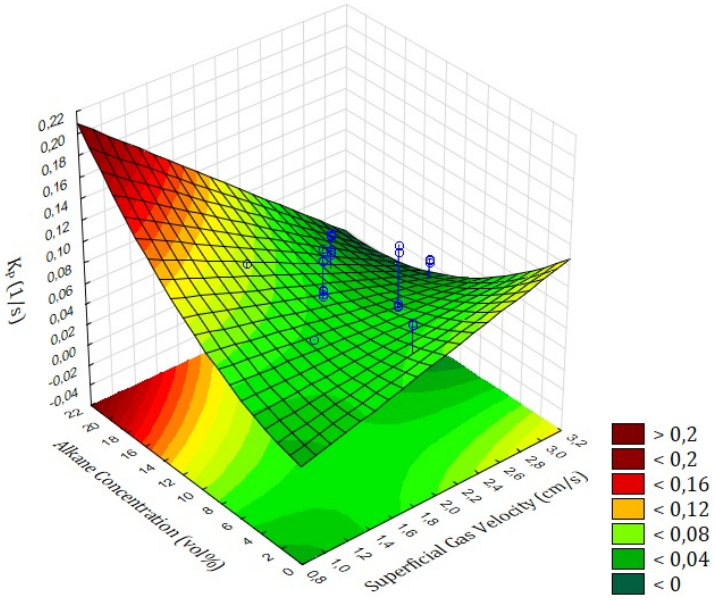

Figure A.28: Influence of the alkane concentration and superficial gas velocity on K_P in corn flour at constant solids loading (low value of 1.62 g/l)

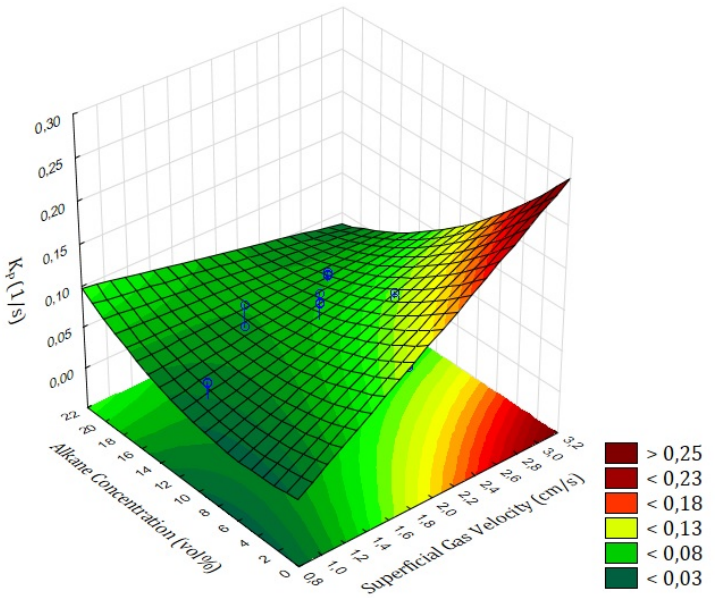

Figure A.29: Influence of the alkane concentration and superficial gas velocity on K_P in corn flour at constant solids loading (high value of 4.88 g/l)

A.11.2 Dependence of K_P on Alkane Concentration and Solids Loading at Constant Superficial Gas Velocity

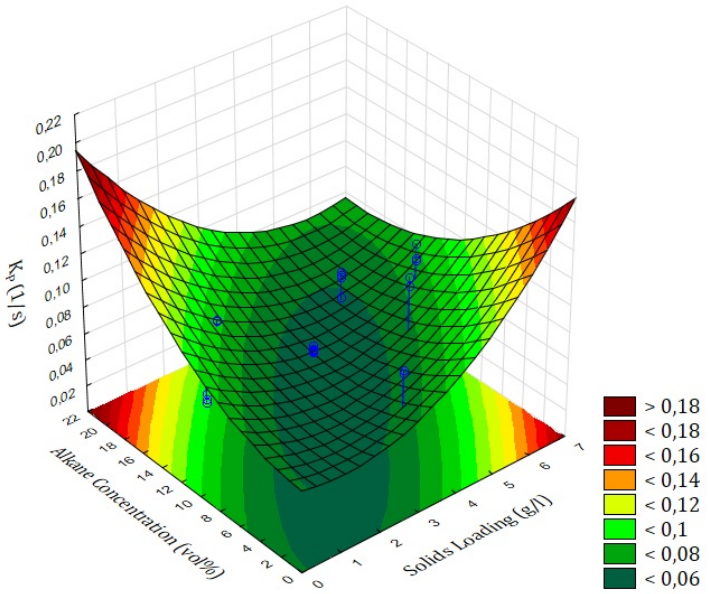

Figure A.30: Influence of the alkane concentration and solid loading on K_P in corn flour at constant superficial gas velocity (low value of 1.62 cm/s)

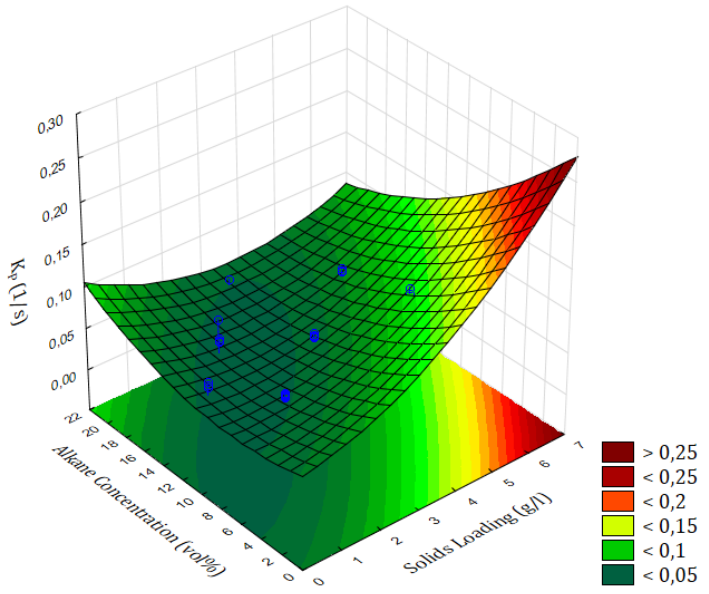

Figure A.31: Influence of the alkane concentration and solid loading on K_P in corn flour at constant superficial gas velocity (high value of 2.38 cm/s)

A.11.3 Dependence of K_P on Superficial Gas Velocity and Solids Loading at Constant Alkane Concentration

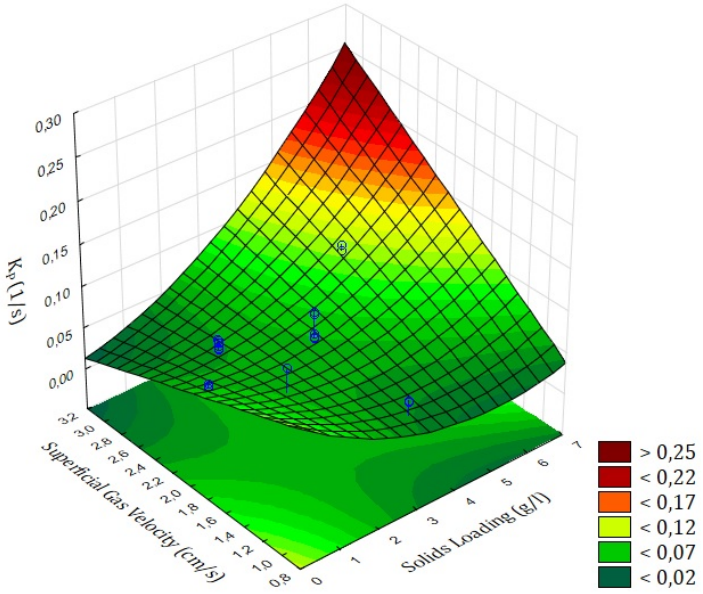

Figure A.32: Influence of the superficial gas velocity and solid loading on K_P in corn flour at constant alkane concentration (low value of 7.88 vol%)

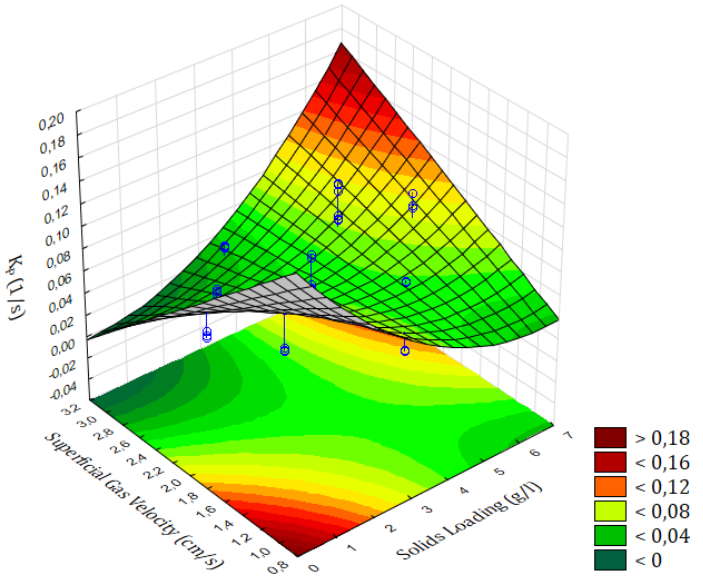

Figure A.33: Influence of the superficial gas velocity and solid loading on K_P in corn flour at constant alkane concentration (high value of 14.62 vol%)

A.12 K_La in Systems Containing Inert Solids

A.12.1 Dependence of K_La on Alkane Concentration and Superficial Gas Velocity at Constant Solids Loading

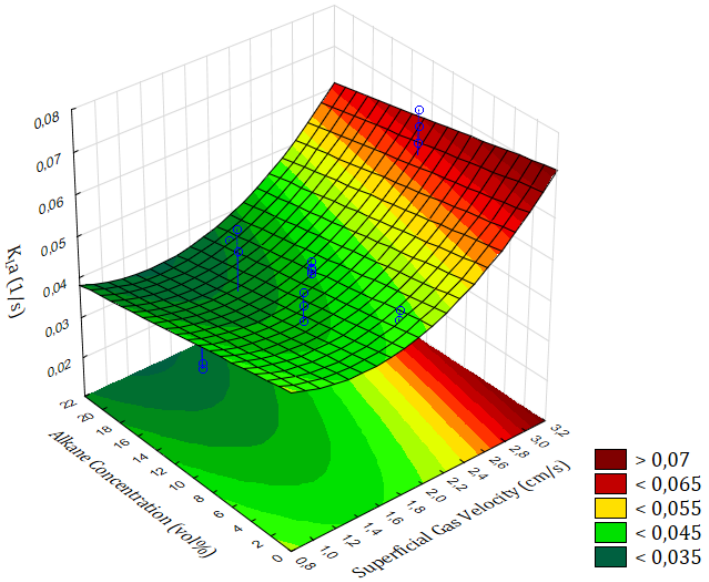

Figure A.34: Influence of the alkane concentration and superficial gas velocity on K_La in corn flour at constant solids loading (low value of 1.62 g/l)

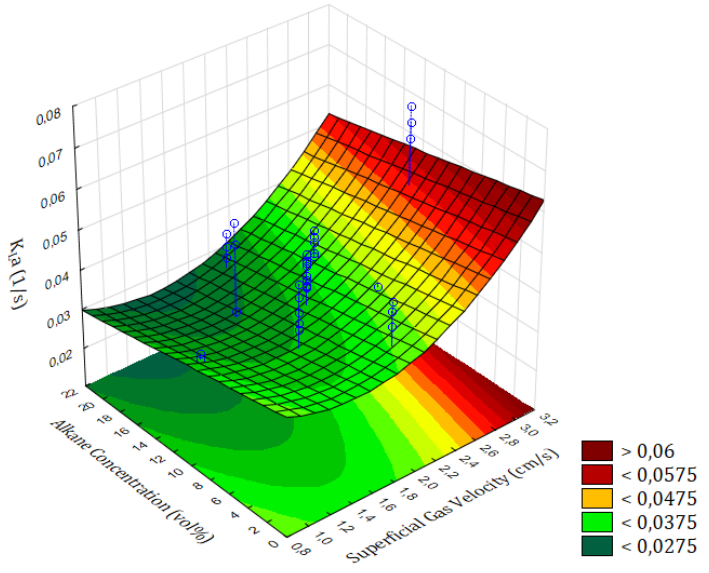

Figure A.35: Influence of the alkane concentration and superficial gas velocity on K_La in corn flour at constant solids loading (high value of 4.88 g/l)

A.12.2 Dependence of K_La on Alkane Concentration and Solids Loading at Constant Superficial Gas Velocity

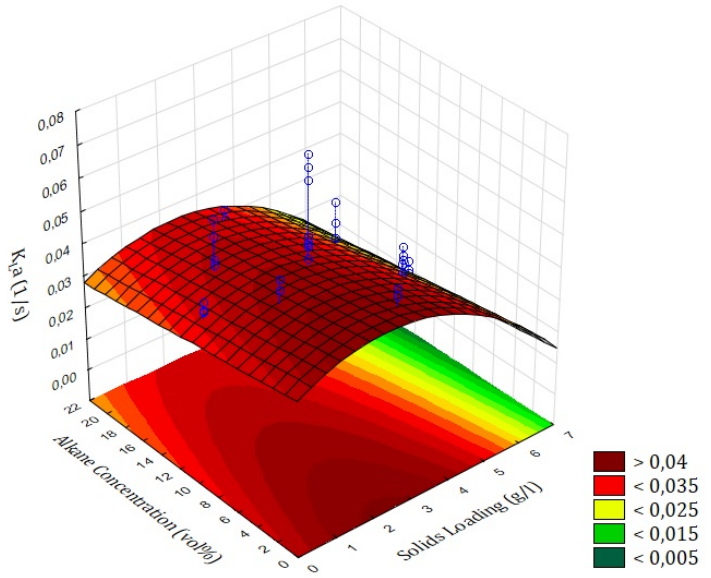

Figure A.36: Influence of the alkane concentration and solid loading on K_La in corn flour at constant superficial gas velocity (low value of 1.62 cm/s)

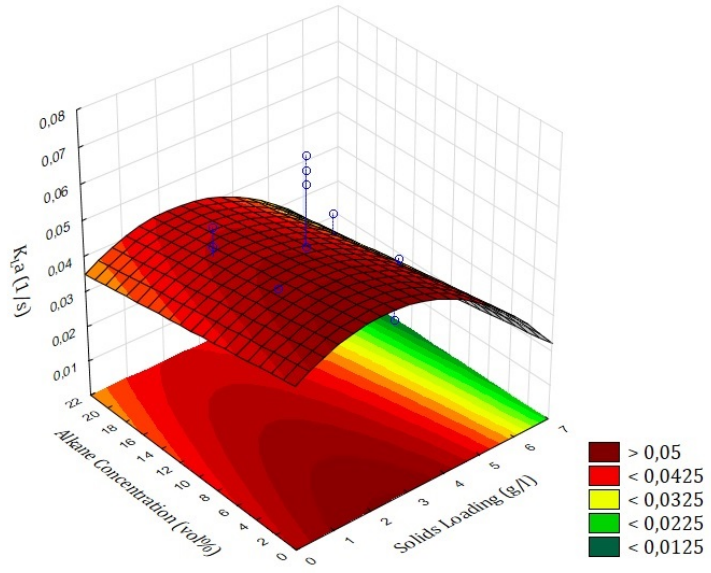

Figure A.37: Influence of the alkane concentration and solid loading on K_La in corn flour at constant superficial gas velocity (high value of 2.38 cm/s)

A.12.3 Dependence of K_La on Superficial Gas Velocity and Solids Loading at Constant Alkane Concentration

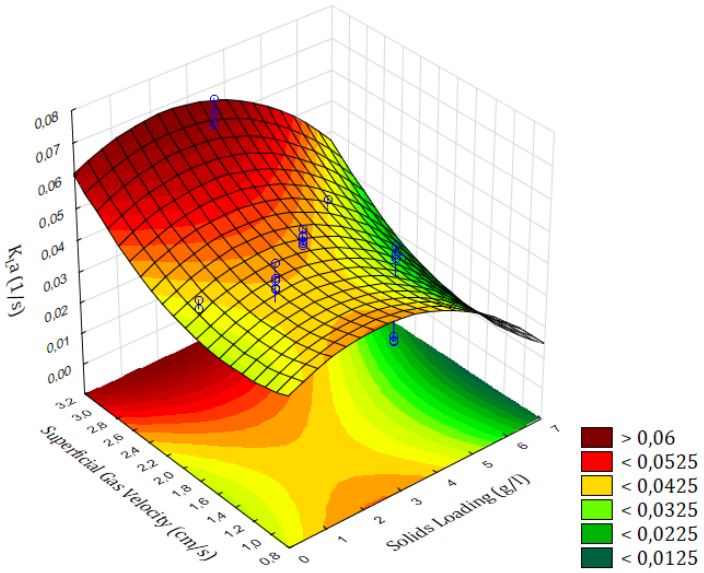

Figure A.38: Influence of the superficial gas velocity and solid loading on K_La in corn flour at constant alkane concentration (low value of 7.88 vol%)

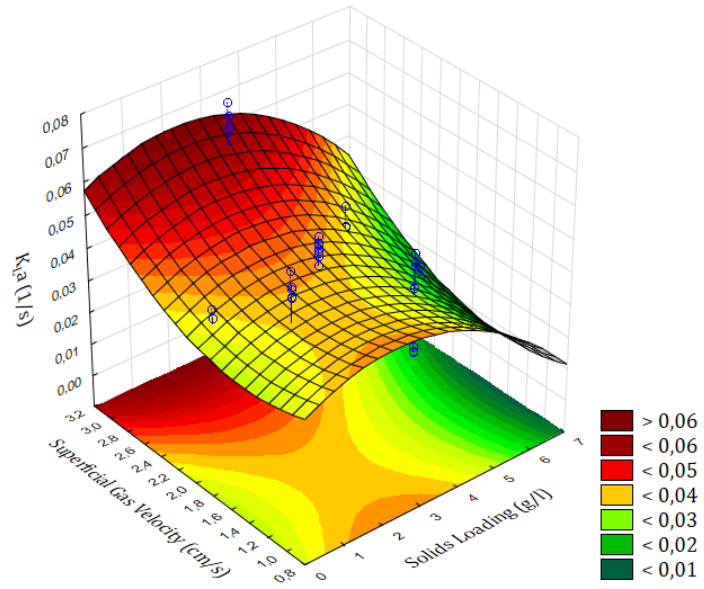

Figure A.39: Influence of the superficial gas velocity and solid loading on K_La in corn flour at constant alkane concentration (high value of 14.62 vol%)

A.13 Sauter Mean Diameter in Systems Containing Non-Viable Microbes

A.13.1 Dependence of Sauter Mean Diameter on Alkane Concentration and Superficial Gas Velocity at Constant Solids Loading

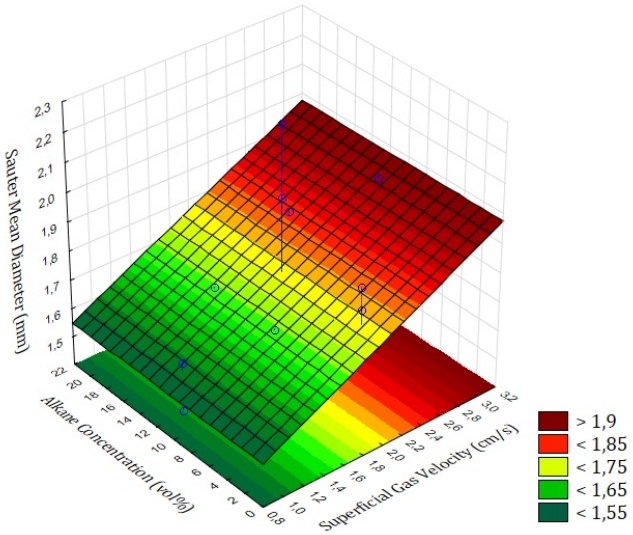

Figure A.40: Influence of the alkane concentration and superficial gas velocity on D_{32} in yeast at constant solids loading (low value of 1.62 g/l)

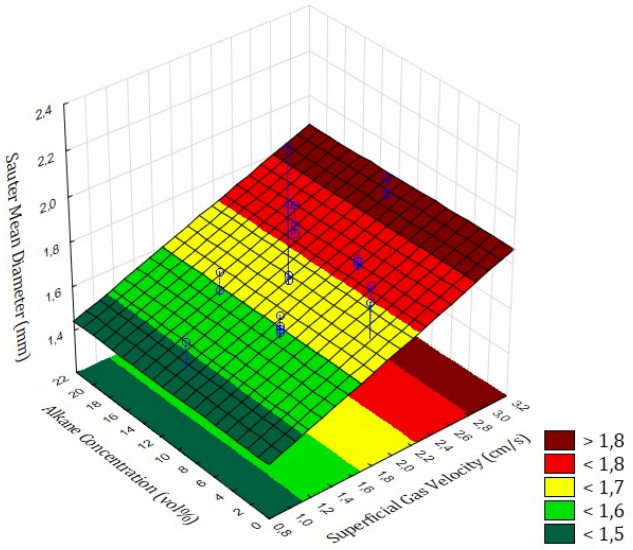

Figure A.41: Influence of the alkane concentration and superficial gas velocity on D_{32} in yeast at constant solids loading (high value of 4.88 g/l)

A.13.2 Dependence of Sauter Mean Diameter on Alkane Concentration and Solids Loading at Constant Superficial Gas Velocity

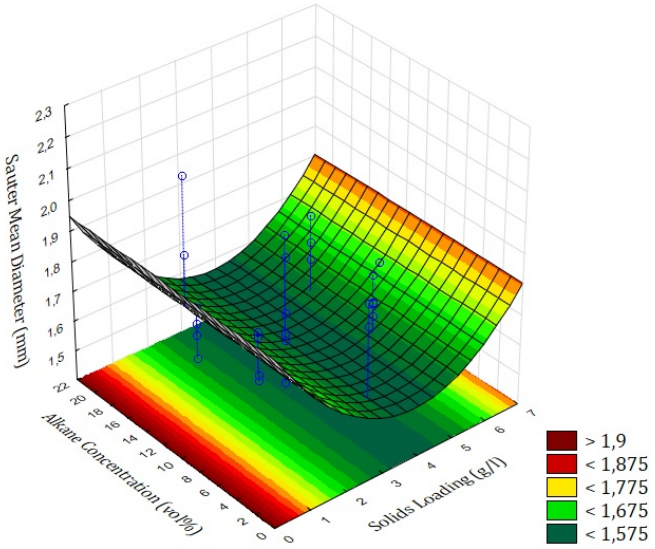

Figure A.42: Influence of the alkane concentration and solids loading on D_{32} in yeast at constant superficial gas velocity (low value of 1.62 cm/s)

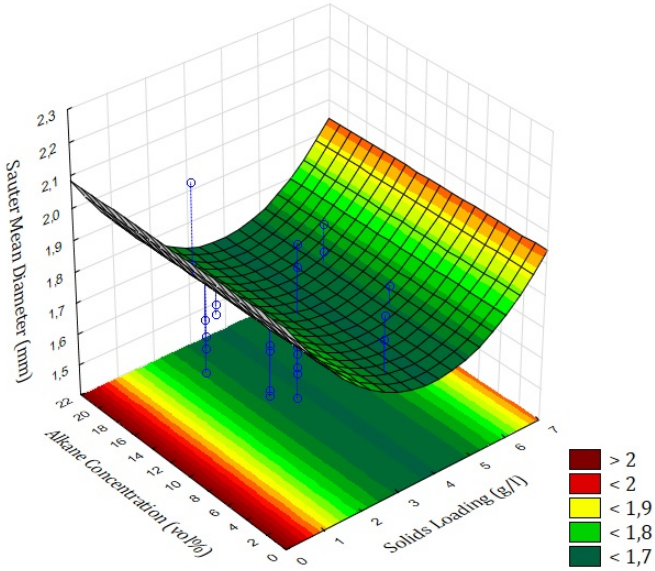

Figure A.43: Influence of the alkane concentration and solids loading on D_{32} in yeast at constant superficial gas velocity (high value of 2.38 cm/s)

A.13.3 Dependence of Sauter Mean Diameter on Superficial Gas Velocity and Solids Loading at Constant Alkane Concentration

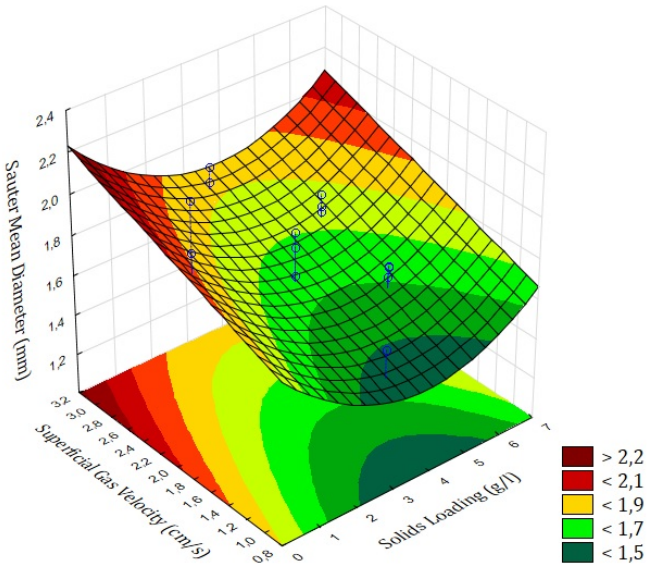

Figure A.44: Influence of the superficial gas velocity and solids loading on D_{32} in yeast at constant alkane concentration (low value of 7.88 vol%)

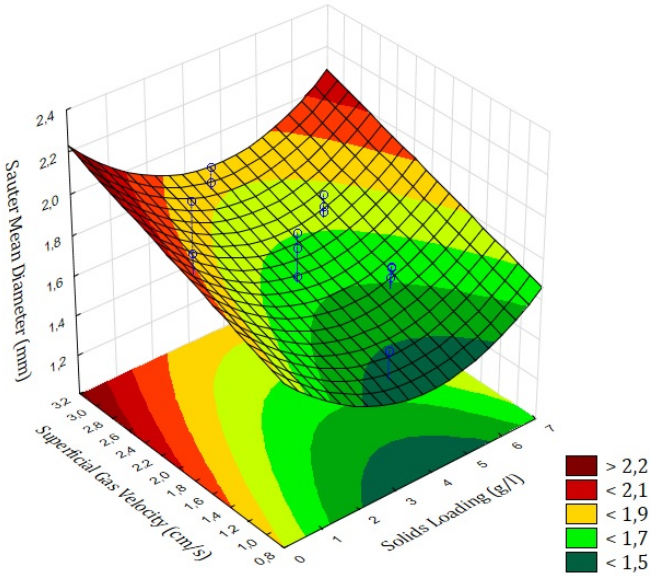

Figure A.45: Influence of the superficial gas velocity and solids loading on D_{32} in yeast at constant alkane concentration (high value of 14.62 vol%)

A.14 Gas Holdup in Systems Containing Non-Viable Microbes

A.14.1 Dependence of Gas Holdup on Alkane Concentration and Superficial Gas Velocity at Constant Solids Loading

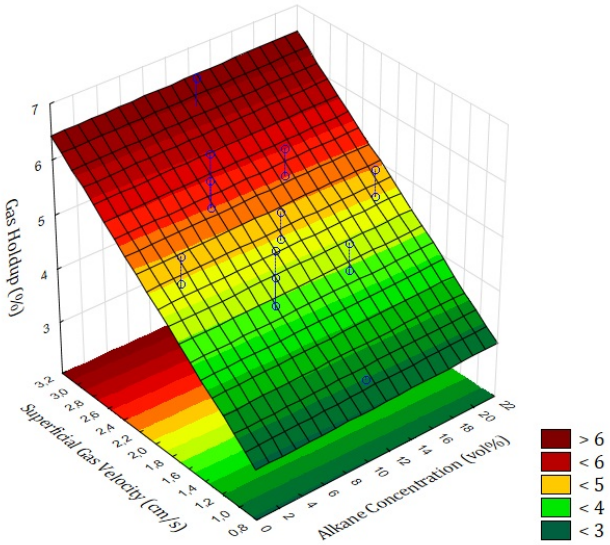

Figure A.46: Influence of the alkane concentration and superficial gas velocity on ϵ_G in yeast at constant solids loading (low value of 1.62 g/l)

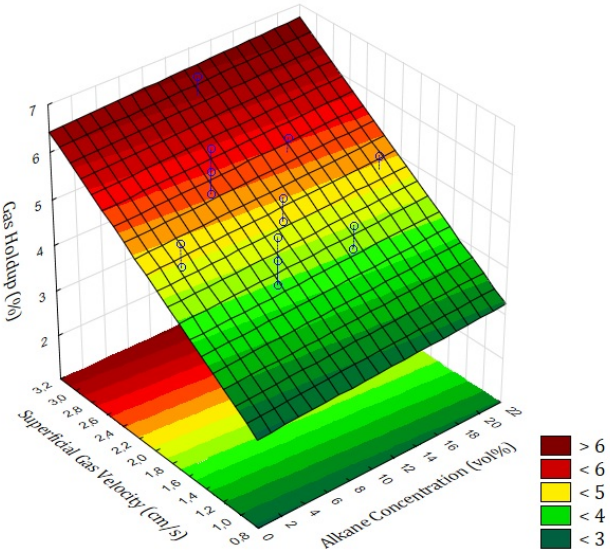

Figure A.47: Influence of the alkane concentration and superficial gas velocity on ϵ_G in yeast at constant solids loading (high value of 4.88 g/l)

A.14.2 Dependence of Gas Holdup on Superficial Gas Velocity and Solids Loading at Constant Alkane Concentration

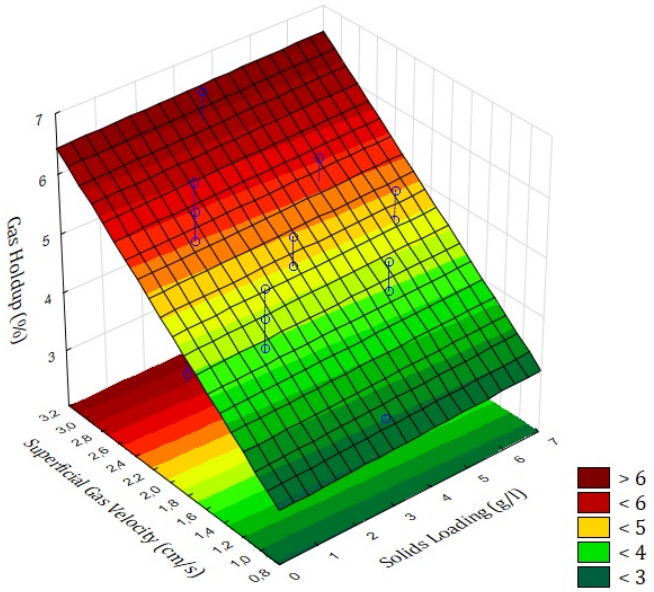

Figure A.48: Influence of the superficial gas velocity and solids loading on ϵ_G in yeast at constant alkane concentration (low value of 7.88 vol%)

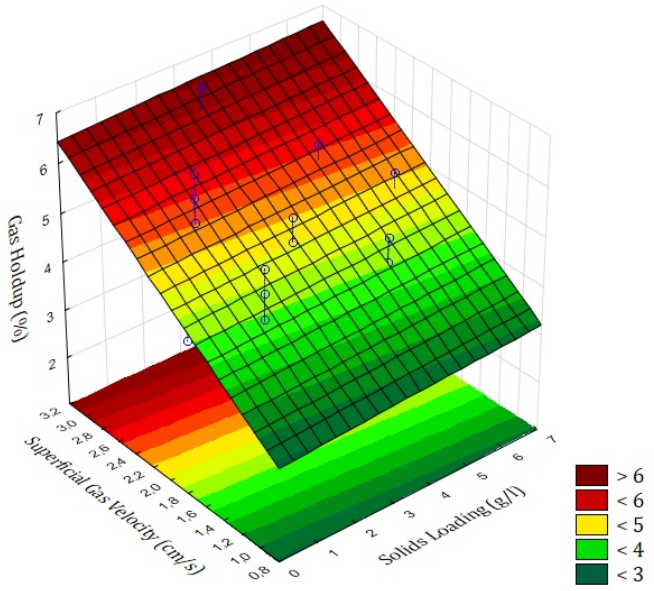

Figure A.49: Influence of the superficial gas velocity and solids loading on ϵ_G in yeast at constant alkane concentration (high value of 14.62 vol%)

A.14.3 Dependence of Gas Holdup on Alkane Concentration and Solids Loading at Constant Superficial Gas Velocity

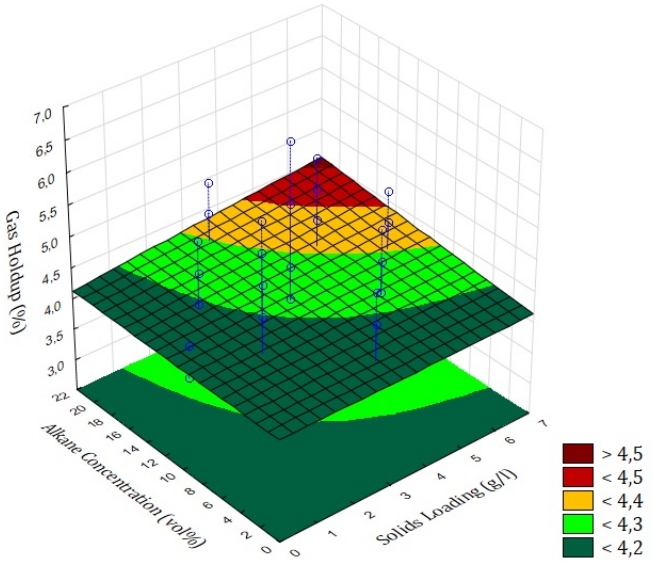

Figure A.50: Influence of the alkane concentration and solids loading on ϵ_G in yeast at constant superficial gas velocity (low value of 1.62 cm/s)

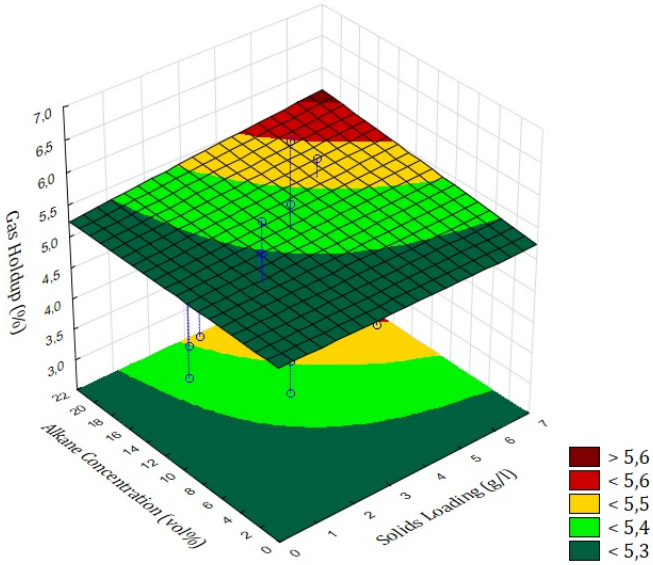

Figure A.51: Influence of the alkane concentration and solids loading on ϵ_G in yeast at constant superficial gas velocity (high value of 2.38 cm/s)

A.15 Interfacial Area in Systems Containing Non-Viable Microbes

A.15.1 Dependence of Interfacial Area on Alkane Concentration and Superficial Gas Velocity at Constant Solids Loading

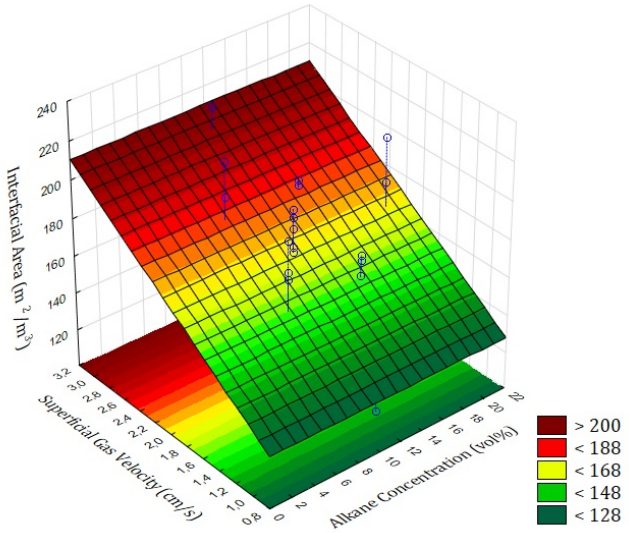

Figure A.52: Influence of the alkane concentration and superficial gas velocity on interfacial area in yeast at constant solids loading (low value of 1.62 g/l)

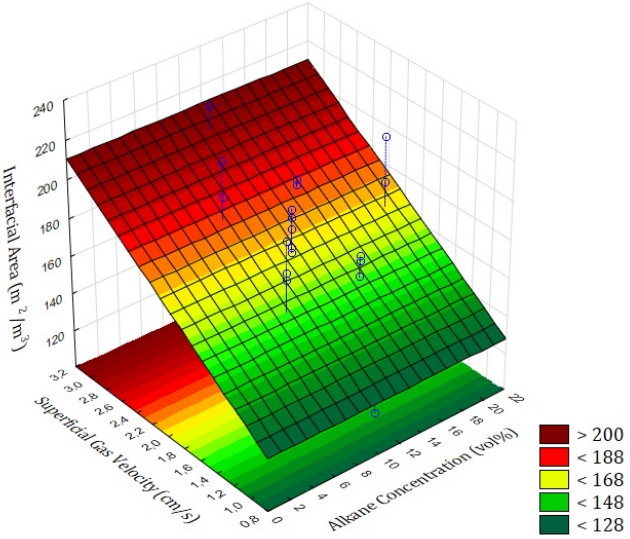

Figure A.53: Influence of the alkane concentration and superficial gas velocity on interfacial area in yeast at constant solids loading (high value of 4.88 g/l)

A.15.2 Dependence of Interfacial Area on Superficial Gas Velocity and Solids Loading at Constant Alkane Concentration

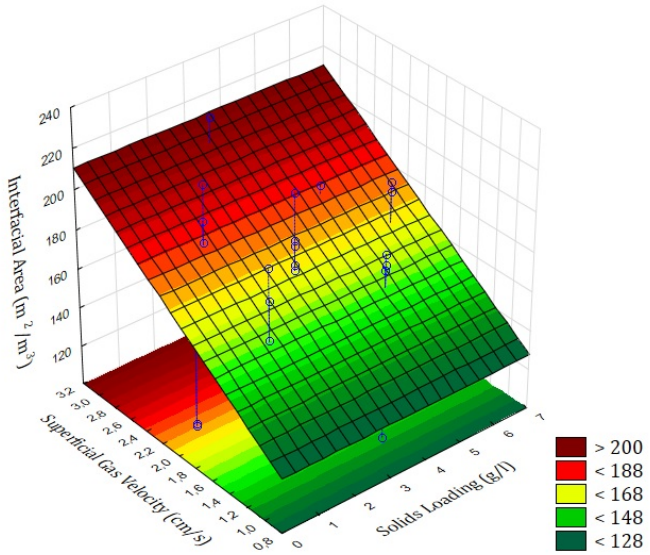

Figure A.54: Influence of the superficial gas velocity and solids loading on interfacial area in yeast at constant alkane concentration (low value of 7.88 vol%)

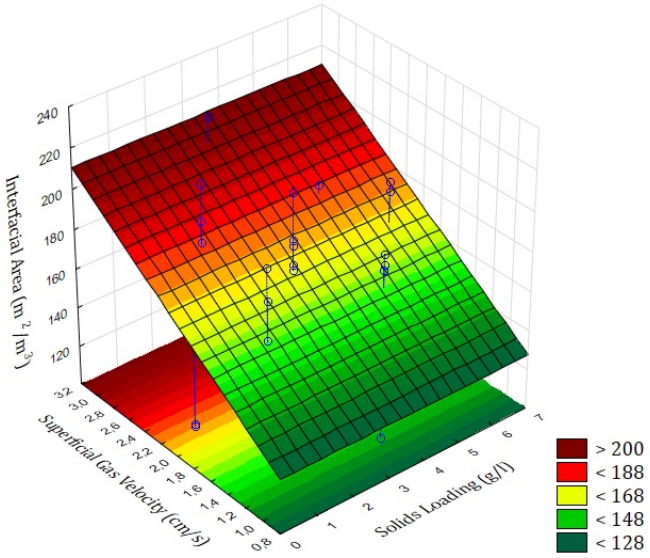

Figure A.55: Influence of the superficial gas velocity and solids loading on interfacial area in yeast at constant alkane concentration (high value of 14.62 vol%)

A.15.3 Dependence of Interfacial Area on Alkane Concentration and Solids Loading at Constant Superficial Gas Velocity

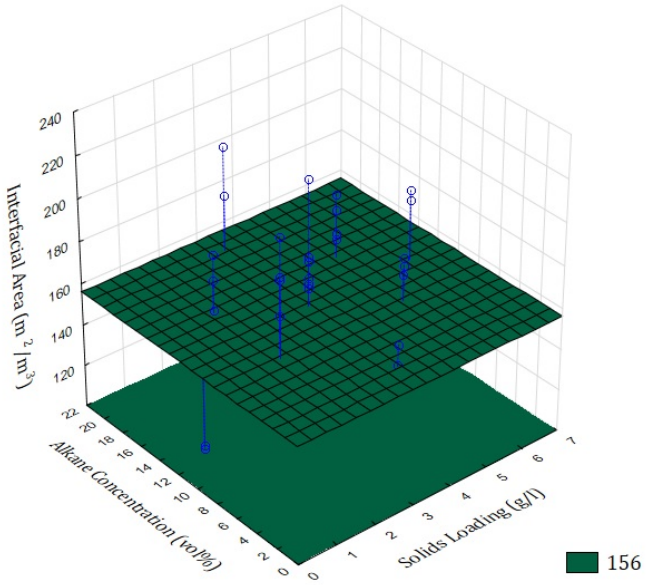

Figure A.56: Influence of the alkane concentration and solids loading on interfacial area in yeast at constant superficial gas velocity (low value of 1.62 cm/s)

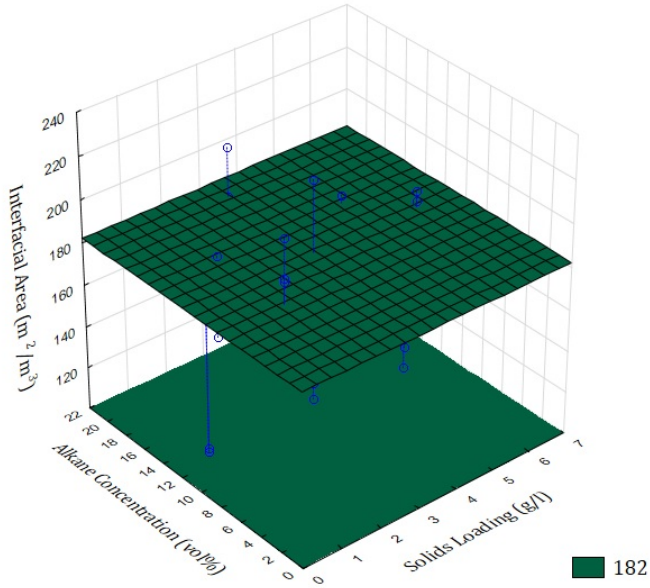

Figure A.57: Influence of the alkane concentration and solids loading on interfacial area in yeast at constant superficial gas velocity (high value of 2.38 cm/s)